Electronic and structural properties of deposited silver nanoparticles: a STM and GISAXS study

Dissertation
zur Erlangung des akademischen Grades

doctor rerum naturalium

der mathematisch-naturwissenschaftlichen Fakultät
der Universität Rostock

vorgelegt von

Kristian Sell

Rostock

urn:nbn:de:gbv:28-diss2011-0009-4

Betreuer:	Dr. Ingo Barke (Universität Rostock) Prof. Karl-Heinz Meiwes-Broer (Universität Rostock)
Gutachter:	Prof. Karl-Heinz Meiwes-Broer (Universität Rostock) Prof. Mathias Getzlaff (Universität Düsseldorf)
Eingereicht am:	29.10.2010
Verteidigt am:	15.12.2010

“Auch das lauteste Getöse großer Ideale darf
uns nicht verwirren und nicht hindern,
den einen leisen Ton zu hören,
auf den alles ankommt.”

Werner Heisenberg

Contents

List of abbreviations

5×2 ..... Si(111)5×2-Au
7×7 ..... Si(111)7×7
ACIS ..... arc cluster ion source
AFM ..... atomic-force microscopy
ALD ..... atomic layer deposition
APS ..... Advanced Photon Source
ARPES ..... angle-resolved photo electron spectroscopy
CBM ..... conduction band minimum
DAS ..... dimer adatom stacking fault
DWBA ..... distorted wave Born approximation
DOS ..... density of states
EELS ..... electron energy loss spectroscopy
FER ..... field emission resonance
GID ..... grazing incidence diffraction
GISAXS ..... grazing incidence small-angle X-ray scattering
HC ..... honeycomb chain
HOPG ..... highly oriented pyrolytic graphite
HV ..... high voltage
LDOS ..... local density of states
LEED ..... low-energy electron diffraction
LT-STM ..... low-temperature scanning tunneling microscope
LWF ..... local work function
MDP ..... mean diffusion path
ML ..... monolayer
SAXS ..... small-angle X-ray scattering
SEM ..... scanning electron microscopy
SPV ..... surface photovoltage
SCCM ..... standard cubic centimeter per minute
SCR ..... space charge region
STM ..... scanning tunneling microscopy / scanning tunneling microscope
STS ..... scanning tunneling spectroscopy
TEM ..... transmission electron microscopy
TPR ..... temperature programmed reaction
UHV ..... ultra-high vacuum
VBM ..... valence band minimum

1. Introduction

In today's science and technology, miniaturization of structures and devices plays a decisive role. The aim is to create and construct smaller mechanical and electronic devices with equivalent or even more features and processing power. Thus in nearly every new generation of devices, the scales are moved towards smaller sizes. Some electronic devices, e.g. transistors, are already on the nanoscale level. But also in chemistry small nanosized aggregates are used as nanocatalysts in reaction environments. The understanding of such nano-sized aggregates needs fundamental research, dealing with the basic properties and effects. Somtimes, the physics of nano-sized objects and devices can be quite surprising, as some of the known physical properties change due to quantum size effects. One approach for studying such systems where these effects play a dominant role, is the investigation of nanosized clusters [1]. These small aggregates, consisting of several to hundred thousands of atoms that are arranged normally in a more or less spherical shape, serve as a perfect lab by filling the gap in the size regime between a single atom and the bulk material. Nanoparticles feature a variety of interesting properties in their electronic, chemical and structural properties that are extremely dependent on the number of the containing atoms [2]. These properties can be accessed by investigating the clusters as free particles, e.g. during their flight through a spectroscopy setup, or as particles that are supported on a solid surface [3, 4]. The support on a surface is also needed for useful applications beyond basic research.

In this work some properties of supported metal nanoparticles will be investigated, with the focus on specific structural and electronic qualities of deposited silver clusters. Ag particles are well suited for the experiments because they have metallic properties (cf. section 2.3) and are known to show catalytic activity during appropriate reactions [5]. The experiments that are presented in the next chapters can be roughly divided in three parts: 1) the behavior of clusters on the surface after deposition, 2) the electronic properties of a model nanoscale metal-semiconductor contact consisting of a Ag cluster deposited on a semiconductor substrate, and 3) the size and shape effects of deposited Ag clusters during a catalytic reaction. These three topics will be briefly introduced in the following.

Deposition of clusters

For investigating the electronic properties in conductive measurement experiments or for catalytic applications, the nanoparticles have to be supported on a sample substrate. In this work the Si(111)7$\times$7 surface serves as a substrate for cluster deposition, as this surface is well known from experiments in the past. In general there are two ways to produce

nanosized clusters on a surface: the clusters can be directly grown on the substrate by evaporation of the cluster material or they can be produced in the gas-phase with a cluster source and deposited from the beam onto the substrate surface. When clusters are deposited on a surface, it depends on their kinetic energy if the particles are soft-landed or fragmented or even implanted upon landing. For most experiments the soft-landing regime is the important process as the clusters are safely landed on the surface and no fragmentation occurs [6, 7].

One interesting aspect, that is investigated in this work, is the behavior of the particles after their landing on the substrate surface. The question is if the particles remain at their impact position or if they move over the surface due to a diffusion mechanism. For smaller particles (several to hundreds of atoms) there have been already several studies in literature, showing that a movement of clusters over the surface is possible in general. Goldby *et al.* [8] investigated small size-selected Ag clusters deposited on HOPG and showed that even the three-dimensional clusters containing thousands of atoms seem to be mobile on the surface up to some degree at room temperature. Carroll *et al.* [9] showed that Ag clusters of several hundred atoms are able to diffuse and become trapped at the surface step edges. A direct and interesting application of this effect was presented by Kebaili *et al.* [10]. They used the diffusion of Ag clusters to decorate step edges and grain boundaries on HOPG for visualizing these structures with scanning electron microscopy (SEM). Masson *et al.* [11] showed that the diffusion of clusters may retain if they reach epitaxial orientation with the substrate. In that case only a mobility limited by the individual atomic movements is possible, resulting in a very small diffusion constant which is in the order of 10^{-17} cm^2s^{-1} at room temperature [12]. Unfortunately for larger particles, like they are used here in this work, there is less information about surface diffusion.

In chapter 4.1 Ag particles are deposited on the Si(111)7×7 surface and analyzed with the help of scanning tunneling microscopy (STM) regarding their behavior after landing and a possible diffusion towards the boundaries and step edges of the surface. Simulated cluster depositions that include a simple diffusion model are compared to the experimental data giving a first hint for the diffusion behavior. The deposited clusters on the Si(111)7×7 surface also serve as a model system for a nanoscale metal-semiconductor contact, that is introduced in the following section.

Nanoscale metal-semiconductor contact

When a metal is brought into electrical contact with a semiconductor, the equilibrium condition of the chemical potential, also known as the Fermi level, forces charge carriers to rearrange and thus a band bending in the semiconductor is induced near the interface. The resulting Schottky barrier gives rise to highly nonlinear transport properties through the metal-semiconductor interface. Compared to p-n junctions in doped semiconductors, the Schottky contact is characterized by an extremely low depletion width in the metal. Schottky devices, such as the Schottky diode or the metal-semiconductor field effect transistor (MESFET) take advantage of the low junction capacitance and the high carrier mobility. These devices are

essential elements in high-frequency applications.
Metal nanoparticles deposited on a semiconductor substrate provide the possibility to create model systems for Schottky contacts in the nanometer regime (Fig. 1.1). They can also be easily modified by choosing the cluster size and supporting material.

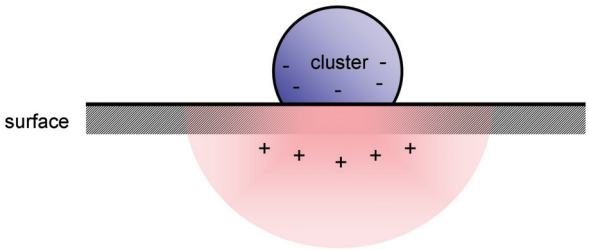

Figure 1.1.: Schematic view of a nanoscale model Schottky contact: metal nanoparticle on a semiconductor surface

Significant deviations from bulk physics are expected because of the particle dimensions being much smaller than the Debye length in the semiconductor, the limited charge reservoir in the metal and the influence of the detailed electron states at the particles-substrate interfaces. Large-scale local-density calculations of a nanometer Schottky contact have been presented by Landman *et al.* [13] for the interface of silicon nanowires and the contacting metal. Compared to the corresponding macroscopic system the Schottky barrier height increases by 40%...90% in this nanosize regime. For Cu particles on TiO_2 a sigificant reduction of the measured contact potential relative to that of an infinite plane has been reported by Carroll *et al.* [14]. Based on voltage-dependent scanning tunneling microscopy (STM) measurements this was explained by contributions of a current flow through the edges of the nanostructures. Furthermore, a number of studies on nanoscale Schottky-contacts using point-contact spectroscopy [15, 16, 17] and other techniques [18, 19] have been presented in the past.
In chapter 4.2 the laser-induced surface photovoltage (SPV) [20] is used for characterizing the band topology of two different nanoscale systems. High spatial resolution is achieved by STM-based determination of the SPV, a technique that has been used by several groups in the past [21, 22, 23]. In this work the band topology of a metal-semiconductor interfaces formed by Ag clusters deposited on Si(111)7×7 is investigated. In addition, nanoscale patches of the quasi-1D chain structure Si(111)5×2-Au serve as a model system helping to understand the results obtained from the clusters. A simple model for the band topology of 7×7 and 5×2 is developed, which is consistent with supporting local work function (LWF) variations. The results are discussed in terms of the SPV theory and the current transport mechanisms of a Schottky contact.

Structural properties of Ag cluster during a catalytic reaction
The catalytic performance of nanoparticles has been subject of extensive theoretical and experimental studies within the catalysis and surface science communities over the last

years [24, 25, 26, 27, 28]. However, in order to elucidate the structure-reactivity relationship in the catalysis, well defined particles as well as the use of industrially relevant supports are required [29]. In addition to the fabrication of the catalysts, the catalyst activity needs to be investigated under realistic reaction conditions, regarding possible industrial applications.
The silver particles serve as catalysts in a catalytic reaction, e.g. the epoxidation of propylene resulting in the formation of propylene oxide and acrolein which are important precursors for a variety of commodity chemicals and polymers [30]. Traditional processes to produce propylene oxide are energy-intensive, inefficient and environmentally unfriendly since the processes involve multiple steps and create large quantities of unwanted by-products and waste. Therefore, the heterogeneously catalyzed direct oxidation of propylene by molecular oxygen has received increased attention lately [31, 32, 5]. Silver-based catalysts have been successfully used in the other epoxidations, e.g. the epoxidation of ethylene, on both the laboratory and industrial scale.
It is a challenging task to elucidate the relationship between structure and reactivity with traditional catalyst preparation methods, which introduce variations in the mean particle size and particle size distribution. Therefore, size selected deposition methods contribute to the understanding of the effect of particle size on the catalytic properties by providing highly uniform model catalyst systems for such studies. In general, the activity of the catalytic metals can be optimized when using them in a form of small sub-nanometer clusters or small nanoparticles [33]. In the epoxidation of propylene to propylene oxide on silver or gold nanoparticles, these catalysts exhibit a strongly size dependent catalytic activity and selectivity. In order to make a correlation between the shape/morphology of the catalyst and its function, it is necessary to track changes in the shape of the nanoparticles induced by temperature and exposure to the reactive gases *in situ* under realistic reaction condition.
In chapter 4.3 grazing-incidence small angle X-ray scattering (GISAXS) is used to monitor changes in size and shape of the supported Ag nanoparticles, while the catalytic performance is followed by simultaneous temperature programmed reaction (TPR) under atmospheric pressure. The main focus of the investigation are the effects on the size and shape of the particles. The result are qualitatively discussed in terms of the change of the cluster morphology.

2. Methods and concepts

In this first chapter the methods and concepts that are used throughout the work are introduced. The aim is to give an overview to the theories behind the experimental methods and the sample systems. Furthermore the physical effects and calculations that are needed for the analysis and the subsequent discussions are explained.

2.1. The metal-semiconductor contact

A part of this work focuses on the electronic properties of a metal-semiconductor contact, also known as a Schottky contact [34]: the surfaces of a semiconductor and a metal are brought into physical contact and form a conductive connection. Figure 2.1 shows the schematic energy-band diagram of a metal-semiconductor contact.

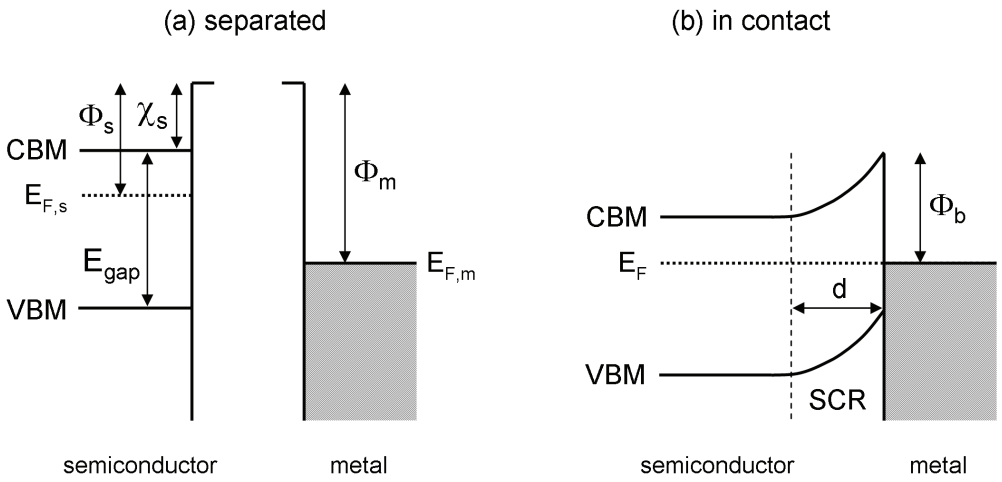

Figure 2.1.: The metal-semiconductor contact: (a) metal and semiconductor are separated, with different Fermi levels E_F, (b) both are in contact, resulting in a band bending in the semiconductor near the interface and a matching of the Fermi levels (according to [35])

In the left image (a) the metal and semiconductor are considered separated. The metal is characterized by a Fermi energy $E_{F,m}$ that describes the highest occupied state. The work function of the metal ϕ_m is the difference between the vacuum level and the Fermi energy. The semiconductor has a different work function ϕ_s and a different Fermi level $E_{F,s}$. The latter is located within the electronic gap, that is given by the difference of the energy of the

valence-band maximum (VBM) and the conduction-band minimum (CBM): E_{gap} = CBM - VBM. The exact position depends on the type of doping, the doping concentration and on the temperature T. The Fermi level is located near the center of the gap for undoped material or near the conduction (valence) band for n-type (p-type) material. With the Fermi-Dirac statistics the exact position of the Fermi level within a n-type semiconductor can be calculated as [35]

$$E_{F,s} = E_{CBM} - kT \ln\left(\frac{N_C}{N_D}\right) \tag{2.1}$$

where E_{CBM} describes the energy at the conduction band minimum, N_C is the effective density of states within the conduction band, N_D the concentration of the dopants. For the n-type Si(111) sample that is used later in this work, the density of states in the conduction band is given as a function of the temperature: $N_C = 6.2{\times}10^{15}$ cm^{-3} $\cdot$ T$^{3/2}$ [36]. According to the manufacturer, the doping concentrations equals $N_D = 3{\times}10^{16}$ cm^{-3}. This leads to a Fermi level position below the CBM of $E_{CBM} - E_F = 0.181$ eV at room temperature (300 K) and $E_{CBM} - E_F = 0.033$ eV for liquid nitrogen temperature (78 K). The difference between the work functions of the two materials $\phi_m - \phi_s$ is called the contact potential. χ_s is the electron affinity of the semiconductor and it is measured from the CBM to the vacuum energy. When both materials get in physical contact, which is sketched in the right image (b), charge carriers from the semiconductor will flow into the states below $E_{F,m}$ of the metal. Thermal equilibrium is established as metal and semiconductor can now be seen as a single system. The Fermi level of the semiconductor E_F is lowered by the amount of the contact potential and equalizes between both materials. The barrier height ϕ_b is given by difference between the metal work function ϕ_m and the electron affinity χ_s of the semiconductor: $\phi_b = \phi_m - \chi_s$. A depletion layer of the width d establishes at the semiconductor side. This layer is also called the space charge region (SCR).

2.1.1. The semiconductor surface

The clean surface of a semiconductor can be described quite similar to a Schottky contact. Here the position of the Fermi level is also different than in the bulk. The surface atoms differ from the bulk atoms regarding the reduced number of binding partners. The abrupt termination of the bulk crystal lattice at the surface and the different symmetry in the atomic bindings result in electronic states, the so-called surface states, that only exist at the semiconductor surface. The surface states are often located within a forbidden energetic region, e.g. within the electronic gap of a semiconductor. They can have donor or acceptor character and can also contain a charge Q_{ss}. Figure 2.2a shows the energetic diagram of an n-type semiconductor surface with distinct surface states. When an atomic orbital misses binding partners, the wavefunction extends from the bulk into the vacuum resulting in so-called dangling bonds.

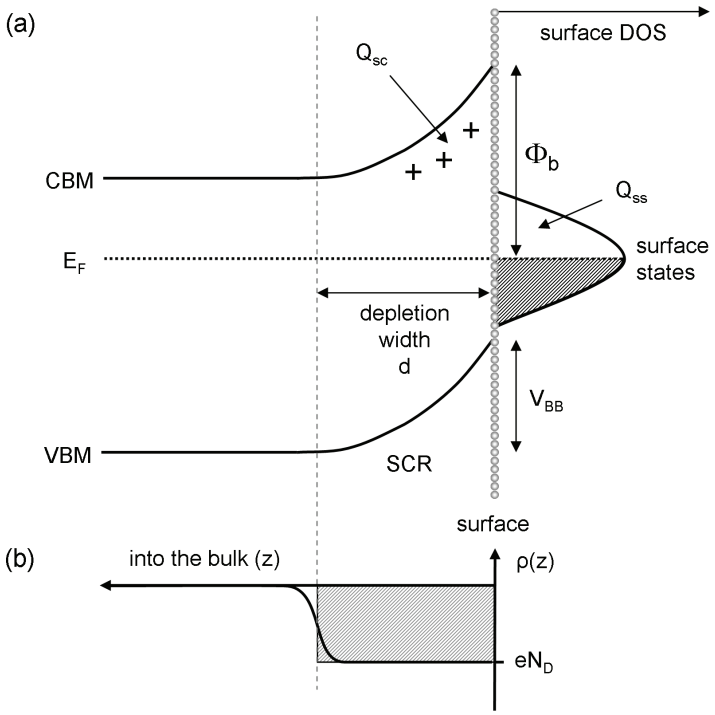

Figure 2.2.: Energetic diagram of (a) the n-type semiconductor surface that exhibits surface states within the energetic gap, (b) the charge density within the depletion region: realistic development (black line) and approximated rectangle (grey box).

The position of Fermi level at the surface has normally a different energetic position than in the bulk, because at the surface the Fermi level is pinned by the surface states at a certain position [37, 38]. This pinning effects the Fermi level in the bulk direction (z direction) as this is bend downwards or upwards near the surface resulting in a space charge region (SCR) near the surface containing the charge Q_{sc}. In equilibrium the band bending V_{bb} is tuned in a way that the SCR equals the negative charge of the surface state: $Q_{sc} = -Q_{ss}$. The SCR induces the depletion region that is positively charged due to the missing of free charge carriers, electrons in this case. The distribution of the charge density $\rho(z)$ is directly connected with the band bending $\phi(z)$ by the Poisson equation [39]:

$$\frac{\partial^2 \phi(z)}{\partial z^2} = -\frac{\rho(z)}{\epsilon \epsilon_0} \tag{2.2}$$

where ϵ is the relative dielectric permittivity of the material and ϵ_0 is the vacuum permittivity. The charge density has contributions from several properties: the concentration of holes $p(z)$, of electrons $n(z)$, of ionized donors N_D^+ and of ionized acceptors N_A^-:

$$\rho(z) = e\Big(p(z) + N_D^+(z) - n(z) - N_A^-(z)\Big) \tag{2.3}$$

In the bulk the charge density $\rho(z)$ equals zero. Due to the band bending near the surface the Fermi level moves closer to the center of the gap. As a consequence, the donators get

ionized and thus positively charged in the SCR. The maximum charge density is given by the donor concentration N_D. In Fig. 2.2b the charge density is plotted against the z direction. Within the SCR the charge density changes from $\rho(z > d) = 0$ to $\rho(0 \leq z < d)$ within a narrow range. Therefore $\rho(z)$ is constant and equals eN_D for $0 \leq z \leq d$. The solution of the Poisson equation is then obtained by integration which results into

$$\phi(z) = \phi(\infty) + \frac{eN_D}{\epsilon\epsilon_0}(z - d) \ , \quad (0 \leq z \leq d) \tag{2.4}$$

The height of the band bending V_{bb} is thus given by:

$$V_{bb} = \phi(\infty) - \phi(0) = \frac{eN_D d^2}{2\epsilon\epsilon_0} \tag{2.5}$$

From this equation one obtains the relation for the depletion layer width:

$$d = \sqrt{\frac{2\epsilon\epsilon_0 V_{bb}}{e^2 N_D}} \tag{2.6}$$

The depletion width is later used in section 2.2.1 for the calculation of the surface photovoltage.

2.2. The surface photovoltage

The photovoltaic effect, discovered by Becquerel in 1839, describes a change in the electronic potential distribution in a sample induced by illumination. The effect of the surface photovoltage (SPV) is a specific variant of the photovoltaic effect where only the surface potential of a sample is changed due to the illumination. This effect has been first noticed on Si and Ge surfaces by Brattain in 1947 [40], followed by a detailed work of him in 1953 [41].

The basic mechanism leading to the phenomenon of SPV is sketched in Fig. 2.3 for a clean n-type semiconductor surface. In equilibrium (Fig 2.3a), the Fermi level pinning induced by surface states results in an upward bending of the bulk bands in n-type semiconductors (downward bending for a p-type semiconductor). Upon illumination (Fig. 2.3b) the absorpted photons of the energy $E_{photon} = h\nu$ produce free charge carriers by creating electron-hole pairs via band-to-band (interband) transitions. If the photon energy is larger than the electronic gap ($E_{photon} > E_{gap}$), the mechanism is called super-bandgap SPV: the possibility for band-to-band absorptions is larger than for trap-to-band absorptions appearing in the sub-bandgap SPV. The electric field within the SCR separates the electron-hole pairs, resulting in a photocurrent of minority carriers (holes for n-type and electrons for p-type semiconductor) moving towards the surface and the majority carriers moving into the bulk. The charge carriers induce an additional potential at the surface, the SPV, causing a partial

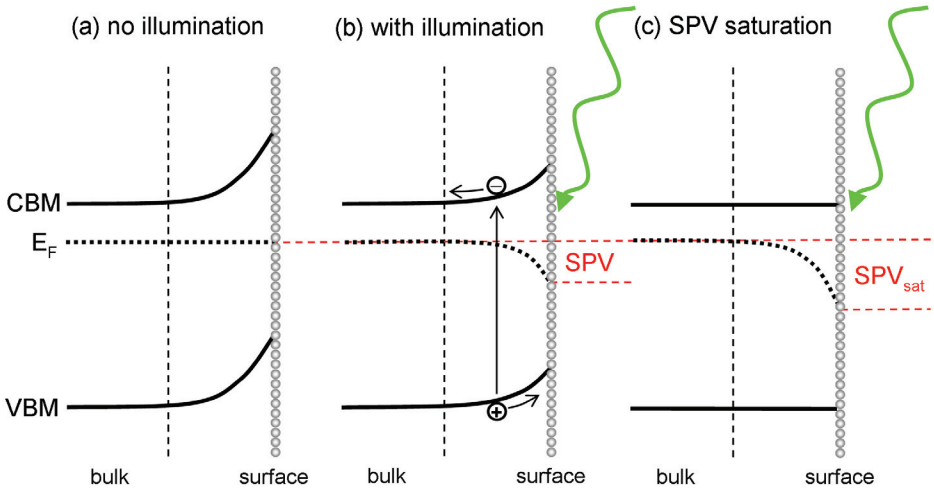

Figure 2.3.: The mechanism of surface photovoltage: **(a)**: surface states pin the Fermi level at a different energy position compared to the bulk. This causes bending of the bulk bands, including the valence band maximum (VBM) and conduction band minimum (CBM), **(b)**: absorpted photons produce free charge carriers resulting in a partial band flattening, **(c)**: largest possible SPV (saturation SPV) occurs for completely flattened bands.

band flattening[1]. At a high photon flux the SPV saturates, resulting in completely flattened bands (Fig. 2.3c). Here the SPV corresponds to the Fermi-level difference between bulk and surface: $SPV = E_{F,bulk} - E_{F,surface}$. In the case of n-type semiconductors the maximum SPV is approximately given by the Fermi-level position relative to the conduction band minimum at the surface.

In this work the surface photovoltage (SPV) is used for characterizing the band topology of nano-sized systems. High spatial resolution is achieved by STM-based determination of the SPV, a technique that has been used by several groups in the past [21, 22, 23].

2.2.1. Calculation of the surface photovoltage

The magnitude of the photon-induced SPV can be calculated using the Schottky model of the thermionic emission [35, 42]. Instead of having a full metal-semiconductor interface, on a plain semiconductor surface the surface states play the role of the metal. Figure 2.4 shows the different current transport mechanisms that may occur in this system.

The photon-generated electron-hole pairs are separated by the potential difference in the depletion region d which gives rise to a photon-induced current j_{ph}. The equalizing currents results from several effects. First there is the thermionic emission of electrons due to the Fermi-Dirac statistics, where at finite temperatures the carrier density at finite energies is

[1] This behavior is in analogy to a photodiode, apart from the fact that there the p-n-transition forms the driving force for the charge carrier separation.

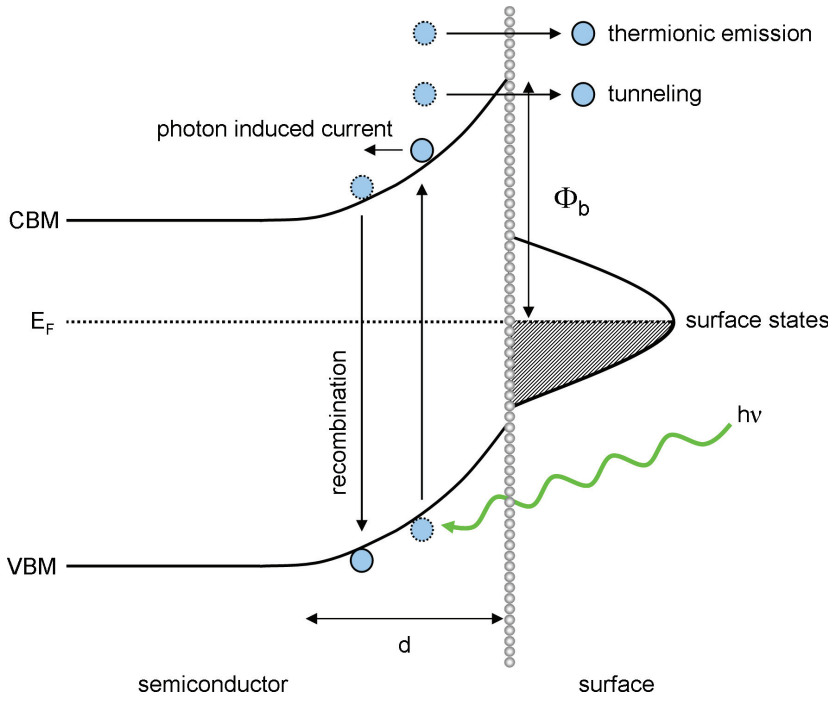

Figure 2.4.: Schematic view of the balance between the photo-induced current and the thermionic emission, the electron tunneling and recombination in the depletion region at a semiconductor surface. (According to [43])

not zero. Electrons with an energy above the potential barrier may diffuse over the barrier resulting in the current from thermionic emission j_{th}. Here the barrier height is the important parameter when considering electrons and not the barrier width or shape. Other occurring mechanisms are the tunneling of electrons through the barrier, resulting in a tunneling current j_{tun} that can be described in analogy to the tunneling in scanning tunneling microscopy (cf. section 2.6). Another current is due to recombination of electron-hole pairs within the depletion zone of the space charge region, resulting in the recombination current j_{rec}. The different recombination mechanisms are sketched in Fig. 2.5.

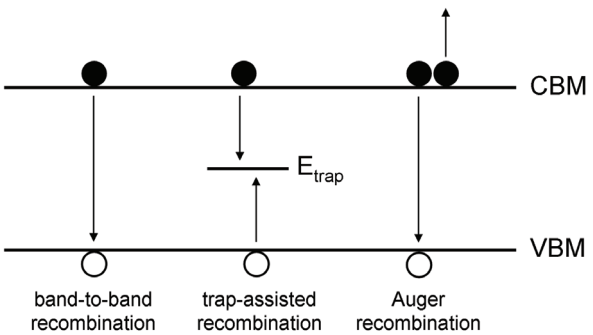

Figure 2.5.: Possible recombination mechanisms: band-to-band recombination, trap-assisted recombination and Auger recombination. (According to Zeghbroeck [44])

In the case of band-to-band recombination an electron moves from the conduction band state into an empty valence band state occupied by a hole. Trap-assisted recombination occurs when an electron falls into a trap state, which is an energy level within the bandgap caused by the presence of foreign atoms or structural defects. In a second step the electron occupying the trap moves into an empty valence band state, completing the recombination process. One can think of this process as a two-step transition of an electron moving from the conduction band to the valence band or as the annihilation of the electron and hole meeting each other in the trap. This process is also known as Shockley-Read-Hall (SRH) recombination [44]. In an Auger recombination an electron and hole recombine in a band-to-band transition, but now the excessed energy is transferred to another electron. The involvement of a third particle has influence on the recombination rate so that the Auger recombination has to be treated differently from the band-to-band recombination. In indirect-bandgap semiconductors such as Si, the dominant mechanism is the indirect SRH recombination via trap states [35].
For a steady-state SPV the photon-induced current is given by the relation [43]

$$j_{pc} = j_{th} + j_{tun} + j_{rec} \tag{2.7}$$

In the Schottky model, the total current over the barrier is only caused by the majority carriers whose energy is larger than the barrier. At semiconductor surfaces with a high density of surface states within the bulk gap, the surface is the dominant recombination site. The effects of tunneling and recombination are neglected in this model. The thermionic emission is derived from the assumptions that the barrier height is much larger than kT and that the thermal equilibrium is not affected by the emission process [35]. Thus one can superimpose two current fluxes: one current flowing from the semiconductor into the surface states and another current of the opposite direction. The first current $j_{sc\to ss}$ is the current density of electrons flowing from the semiconductor into the surface states. It can be expressed as

$$j_{sc\to ss} = A^* T^2 \exp\left(-\frac{e\phi_b}{kT}\right) \exp\left(\frac{eU_{SPV}}{kT}\right) \tag{2.8}$$

where $e\phi_b - eU_{SPV}$ is the barrier height that the electrons have to overcome to get into the surface states. The first exponential term describes the barrier height, the second term is due to an external voltage, which is the SPV in this case. A^* is the effective Richardson constant that depends of the effective electron mass and considers the velocity distribution of the electrons, as only those with a sufficient velocity perpendicular to the surface can overcome the barrier. A^* can be expressed as

$$A^* = \frac{4\pi e m^* k^2}{h^3} \tag{2.9}$$

Under external bias, the barrier height remains the same for electrons moving from the surface states into the semiconductor. Therefore the current density directing into the semiconductor is unaffected by the SPV, and $j_{ss\to sc}$ must be equal to $j_{sc\to ss}$ when thermal equilibrium

prevails, i.e. when $U_{SPV} = 0$:

$$j_{ss\to sc} = -A^* T^2 \exp\left(-\frac{e\phi_b}{kT}\right) \tag{2.10}$$

The total thermionic emission current is then given by the sum of equations 2.8 and 2.10

$$j_{th} = j_{ss\to sc} + j_{sc\to ss} = A^* T^2 \exp\left(-\frac{e\phi_b}{kT}\right)\left[\exp\left(\frac{eU_{SPV}}{kT}\right) - 1\right] \tag{2.11}$$

In equilibrium the induced photocurrent j_{pc} equals the current of the thermionic emission j_{th}:

$$j_{pc} = j_{th} \tag{2.12}$$

According to Singh [45], the photocurrent is a function of the wavelength of the light and the width d of the SCR which is on the other hand a function of U_{SPV}

$$j_{pc} = \frac{eP}{h\nu}\left(1 - e^{-\alpha d(U_{SPV})}\right) \tag{2.13}$$

where P is the intensity of the incoming light and α is the absorption coefficient of the sample material. Using equations 2.11, 2.12, 2.13 and the relation $d(U_{SPV}) \propto \sqrt{V_{bb} - U_{SPV}}$, the light intensity P can be written as a function of the induced SPV

$$P = \frac{C\left(e^{eU_{SPV}/kT} - 1\right)}{1 - \exp(-\alpha c\sqrt{V_{bb} - U_{SPV}})} \tag{2.14}$$

with $C = A^* T^2 \frac{h\nu}{e} e^{-e\phi_b/kT}$ and $c = \sqrt{2\epsilon\epsilon_0/eN_D}$ summarizing all constants. For Si the absorption coefficient is $\alpha_{Si} = 10^4$ [35] for a wavelength of $\lambda = 532$ nm and the depletion width is about $d \approx 500$ nm. Therefore the exponential term in equation 2.13 can be approximatively neglected. This leads to a simpler expression for the photocurrent

$$j_{pc} = \frac{eP}{h\nu} \tag{2.15}$$

Now the surface photovoltage can be written as a function of the incoming light intensity:

$$U_{SPV} = \frac{kT}{e} \ln\left(1 + \frac{\exp(\phi_b/kT)}{A^* T^2 h\nu} P\right) \tag{2.16}$$

Putting all constants into A and B leads to a simplified expression

$$U_{SPV} = A \cdot \ln(1 + B \cdot P) \tag{2.17}$$

So for moderate light intensities the photocurrent is directly proportional to the light intensity and thus the SPV shows a logarithmic dependence on the light intensity [21]. At higher photon fluxes the SPV saturates due to the completely flattened bands. In this saturation regime equation 2.17 is no longer valid and the SPV is given by a constant

saturation value. In a normal experiment the SPV is influenced by recombination rates, diffusion lengths and other effects, so that the study of the SPV provides access to those physical quantities.
Another aspect that influences the magnitude of the SPV is a potential effect that may appear across the region of the sample that is electrically neutral in equilibrium. This potential has its origin in the non-equal generation and recombination of charge carriers in the sample. Since the diffusion of electrons is faster than the one for holes, a small photo-induced positive surface potential appears for both n- and p-type samples, which is called the Dember potential [46, 35]. It results from the larger loss of photo-electrons into the bulk. The appearing potential equalizes the electron and hole fluxes at the surface in the steady state. The resulting Dember addition to the SPV, which is not due to the band bending in the dark, is in the order of only a few mV. Therefore it can be neglected in the discussion of the SPV in this work.

2.3. Deposited Ag cluster

Silver (Ag) is an element of the transition metals with the atomic number 47. Considering bulk silver, it crystallizes in the fcc structure with a lattice constant of 0.409 nm. The bulk phase of Ag has a very high electrical and a high thermal conductivity.
A solid metal can be electronically described in a first approximation by the model of a free electron gas. Here the valence electrons are delocalized and can move freely throughout the crystal lattice. A cluster can be analogically described in context of the spherical jellium model [47, 48]. Here the valence electrons are also delocalized, mutually interacting and confined by the attractive potential of the positive ions. As this attractive potential is known to be weak and slowly changing over the distance, it can be described by the approximation of a homogeneous background potential substituting the average ionic density. In the case of clusters, the detailed spatial distribution of the ions can be replaced by a constant positive charge distribution (jellium) that is confined within a chosen spherical volume. Although this model is a simple approximation it provides a good insight into the electronic structures of metal particles. The detailed electronic properties of clusters are not part of this work. Instead, the particles are deposited onto a Si surface and considered to be the “metallic part” of a metal-semiconductor contact.
In general, the properties of clusters differ from those of a single atom and bulk material. So it cannot taken for granted that the particles in the here used size-regime have a metallic character. Looking at one single Ag atom, it does not show metallic properties. On the other hand, bulk silver is known to be a metal with high electrical conductivity. Due to the finite size, clusters exhibit a discrete electron density of states (DOS), resulting in a finite energy spacing δ between the energy levels around E_F [49]. Here a finite temperature T is needed to excite electrons into the empty states. An estimation of this temperature was given by

Kubo [50]:

$$kT = \delta = \frac{4E_F}{3N} \tag{2.18}$$

with N being the number of valence electrons in the finite system. With this equation, the temperature T can be estimated for a Ag particle with a radius of 4.5 nm that is used in this work: with the Fermi energy $E_F = 5.5$ eV for silver and the estimated number of atoms in the cluster $N = 23068$, one obtains a Kubo gap of $\delta = 3.2\times10^{-4}$ eV. So at temperatures above 3.7 K, these Ag particles show a metallic character. The larger the particles, the smaller the Kubo gap and the lower is the temperature for the insulator-metal transition. It is also possible to estimate, at what cluster size the metal-insulator transition takes place e.g. for $T = 78$ K: below an atom count of $N = 1094$, which corresponds to a particle radius of about 1.6 nm, the particles should show insulating character. So according to this result and by only going down to liquid nitrogen temperature in the experiments, all the Ag clusters used in this work have metallic properties.

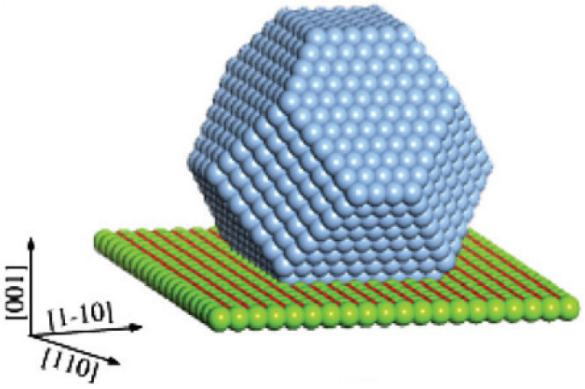

Figure 2.6.: Calculated lowest energy structure of a Ag cluster supported on the MgO(001) surface. The cluster has the shape of a truncated octahedron containing (001) and (111) facets. [51]

Another very important aspect of the nanoparticles are the structural properties and the shape. A cluster consists of several up to thousands of atoms, that are arranged in a three-dimensional structure [1]. The exact shape strongly depends on the number of cluster-atoms. Especially in the regime of low atom counts the shape may change when adding or removing single atoms [52, 53]. For larger clusters, consisting of hundreds to several thousands of atoms, the shape, which is normally a polyhedron, can be determined by the Wulff construction and the minimizing of the surface energy, respectively. For large Ag clusters ($N >> 100$) that are used in this work, the equilibrium shape is given by a truncated octahedron (for fcc structure) or by a rhombic-dodecahedron (for bcc structure)

[1] Normally a small aggregate containing only several to hundred atoms is called “cluster”, whether the larger ones containing thousands of atoms are normally called “nanoparticles”. As there is no official definition, both terms will be used in this work equally, although only larger particles appear here.

[54]. This is confirmed by calculations of Long *et al.* [51] showing also the shape of a truncated octahedron for Ag clusters supported on the MgO(001) surface (cf. Fig. 2.6). The octahedral shape is covered by (001) and (111) facets. It can be seen that the cluster is truncated at the bottom at the interface between the cluster and the substrate. The magnitude of this truncation is proportional to the adhesion energy, which is equal to the work that is necessary to separate the cluster from the sample surface by an infinite distance [54].
In this work the clusters are produced from gas phase (cf. section 3.2) and deposited from the free beam onto the Si(111)7×7 surface, which is described in the next section. Although the kinetic energy of the clusters is rather low upon landing, the shape of the particles may be modified or reduced by a certain amount depending on the impact energy, and the material of the cluster and the substrate.

2.4. The Si(111)7×7 surface

The Si(111)7×7 (in the following referred to as "7×7") surface reconstruction has been known since several decades. It is perfectly suited as a substrate for a number of experiments as it is well known, easy to prepare and quite well understood. It was observed for one of the first times with low energy electron diffraction (LEED) by Lander *et al.* [55] and Ridgway *et al.* [56]. The first real-space imaging was done by Binnig and Rohrer [57, 58] some years after they introduced the principle of scanning tunneling microscopy in 1982. The reconstruction of the surface can be described by the dimer-adatom stacking fault (DAS) model which has been developed by Takayanagi *et al.* in 1985 [59] (Fig. 2.7). Today this model is commonly accepted in the literature.

The unreconstructed Si(111) surface has one dangling bond on each surface atom. So each Si surface atom has a non-bonding orbital that can accommodate two electrons. However, it is only occupied by a single electron, resulting in surface states with a metallic character. The 7×7 reconstruction reduces the numbers of dangling bonds by about a factor two, without changing the electronic properties of the surface.
A 7×7 unit cell consists of a faulted and unfaulted half unit with 6 adatoms and 3 rest atoms per half unit, respectively (Fig. 2.7a). A unit cell contains 19 dangling bonds that are aligned perpendicular to the surface: 12 for the adatoms, 6 for the rest atoms and 1 for the atom below the corner hole (Fig. 2.7b). In STM the 7×7 reconstruction has a different appearance depending on the polarity of the gap voltage. At positive sample voltages the electrons tunnel into the unoccupied states where the topography shows a ring-like structure (Fig. 2.8a), while at negative voltages the electrons tunnel into the occupied states, where the faulted and unfaulted half of the unit cell can clearly be distinguished as dark and bright triangles (Fig. 2.8b+c). In normal STM experiments, using conventional tungsten tips, only the adatoms are visible due to their electronic states being closer to the Fermi level than those of the rest atoms [60]. Nevertheless it is possible to image the rest atoms with

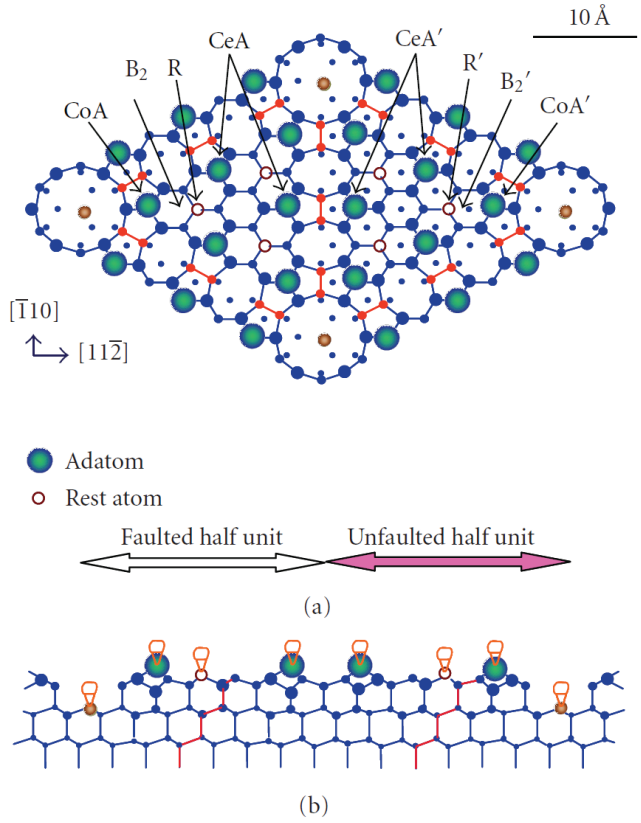

Figure 2.7.: Structural model of the Si(111)7x7 unit cell. (a) top view of the faulted and unfaulted half unit with 6 adatoms (green circles) and 3 rest atoms (small red-white circles) per unit. The sites of corner adatom (CoA), center adatom (CeA), and rest atom (R) are identified by arrows. (b) side view showing the dangling bonds that are located at the topmost of all adatoms, rest atoms, and holes. [60]

STM by using a tip that is contaminated with semiconducting atoms of the surface or with a completely semiconducting tip like InAs [61]. In this work only the adatoms are visible as normal tungsten tips are used throughout the experiments.
During preparation of the 7×7 surface (cf. section 3.1), the on-going reconstructing process of the 1×1 bulk structure of the Si will start at different locations [62]. This results in many 7×7 patches forming on the surface independently. When two of these patches hit each other they can be misfitted by a whole-numbered multiple of one unit cell of the 1×1 bulk [63]. A result of this misfit is the creation of grain boundaries and special defect structures appearing between the patches. Within these boundaries and defects the 7×7 reconstruction is distorted to compensate the misfit between neighbored patches. In Fig. 2.9 four types of defects can be identified. The line-like boundaries (1) appear due to the misfit between two neighbored 7×7 patches. On this sample, a boundary may also end at a step edge (2) where the mismatch is compensated. The step edges are due to internal stress during the UHV preparation or to the manufacturing process of the wafer. The cutting and polishing

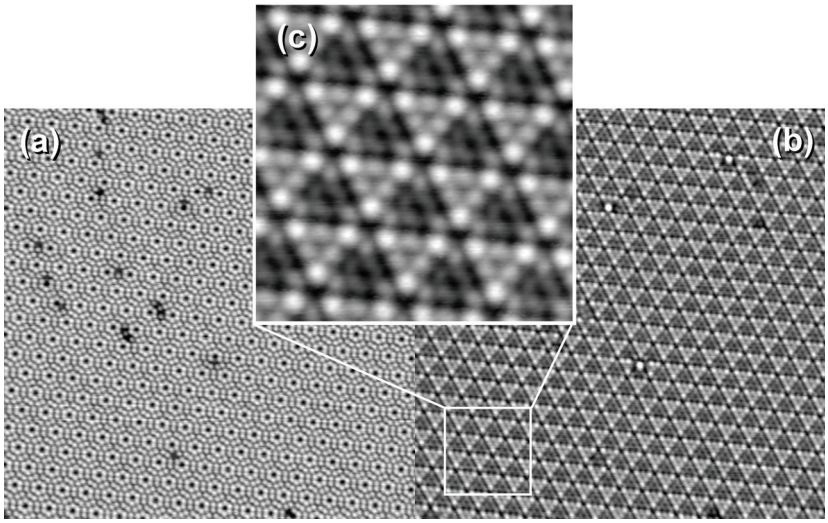

Figure 2.8.: Topographic images of the Si(111)7x7 reconstruction at **(a)** a positive gap voltage of +0.8 V and **(b)** a negative gap voltage of −1.3 V (50 nm × 50 nm, $I_T = 50$ pA). **(c)** zoomed view of the 7x7 reconstruction at negative gap voltages (10nm×10nm)

may result in a small miscut in the angle, so that the surface of the wafer is not perfectly parallel with the lattice planes of the bulk material. This leads to the formation of step edges appearing regularly on the surface. The formation of the triangular defects (3) has been suggested to be due to the mismatch of three 7×7 domains [62, 64]. These triangles also appear when two boundaries hit a step edge (dark line) within a certain distance as it can be seen at location (4). Zhou *et al.* [63] proposed that within a triangular defect it would be too difficult for a surface reconstruction to accommodate to the surrounding three reconstruction domains. Therefore the absence of adatoms would release the mismatch stress in this region. The electronic properties of the 7×7 surface have been analyzed in the past using different techniques, including photoelectron spectroscopy (PES) [65, 66, 67], electron energy-loss spectroscopy (EELS) [68] and scanning tunneling microscopy (STM) [69, 70]. Angle-resolved photoelectron spectroscopy (ARPES) studies have consistently reported the existence of three surface-state bands. The two bands closest to the Fermi level are interpreted as belonging to the dangling-bonds and the third is associated with back-folding bonds. The two bands resulting from dangling bonds show only a weak dispersion [65], which has been verified by STM studies [69]. Photoelectron spectroscopy shows a significant emission at the Fermi energy implying that the 7×7 surface has a metallic character. A detailed theoretical analysis of the surface electronic structure is presented by Ortega *et al.* [71]. The occupancies of different dangling-bonds associated with rest atoms, the corner-hole atom and the adatoms are analyzed. The results show that the adatom-dangling bonds control the electron density of states (DOS) at the Fermi level and therefore add the main contribution to the tunneling current in STM. The calculations also confirm the metallic character of the 7×7 reconstruction. Recent results from Modesti *et al.* [72] show the presence of an energy gap in the ground state of the 7×7 surface at temperatures < 20

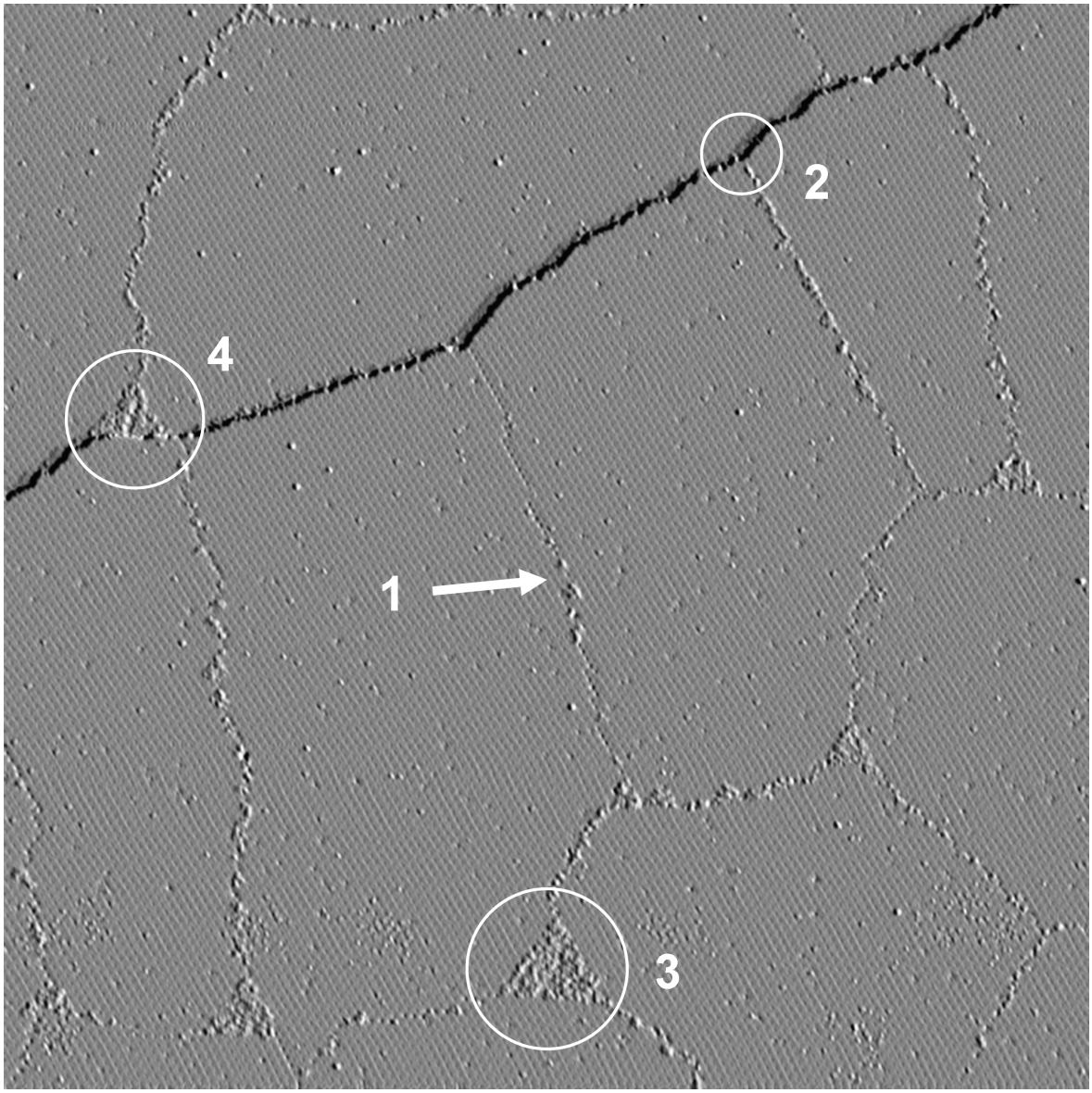

Figure 2.9.: STM image showing the different types of domain boundaries: (1) normal boundary between two 7×7 patches, (2) a boundary hitting a step edge, a triangular pattern where (3) three boundaries converge and (4) two boundaries hit a step edge within a certain distance. The image is processed with a numerical differentiation in horizontal direction to emphasize the topographic details. (350 nm × 350 nm, $U_{gap} = -1.5$ V, $I_T = 15$ pA)

K. As a result the 7×7 would be insulating at these low temperatures. They attribute this not to a Mott-Hubbard transition, but to electron-phonon interactions connected with lattice distortions.
The plain 7×7 surface can be used as a basic surface for a number of experiments. The evaporation of gold onto this surface, e.g., leads to a quasi 1D chain structure that can be used for investigating low-dimensional electronic effects. This structure will be introduced in the next section.

2.5. The Si(111)5×2-Au reconstruction

When gold is evaporated on Si(111)7×7 the quasi one-dimensional reconstruction Si(111)5×2-Au is formed. Although this system has been known since more than forty years [73] the finding of the structural model was not successful for many years. Proposed models (cf. references [74, 75, 76, 77, 78]) gave first hints for the structure but they were all found to be inconsistent with STM measurements or angle-resolved photoemission spectroscopy (ARPES). Recently a structural model that is consistent with the experiments was proposed by Erwin *et al.* [79]. Studies conducted within this work have contributed to the development of this model [80]. It is also consistent with STM measurements as it nicely reproduces the details of topographic images. Figure 2.10 shows the new proposed model: the yellow circles are Au and the small circles are Si atoms. The surface layer consists of a single row Au (S), a Au double row (D) and the silicon honeycomb chain (HC). The dark blue atoms are Si adatoms that decorate the surface with a local 5×4 periodicity to minimize the surface energy. Due to the presence of the adatoms the 5×1 periodicity of the substrate doubles to the 5×2 (grey unit cell) caused by a dimerization within the Au gold double row [79].
This new model is similar to a model proposed by Erwin *et al.* [75] before, except the important modification that it is based on a new value for the ideal Au coverage. In a collaboration with the groups of Erwin and Himpsel, this revised value for the Au coverage was found by a careful analysis of large-scale STM images [80]. This value for a complete Si(111)5×2 (in the following referred to as "5×2") surface amounts to 0.6 ML, where 1 ML corresponds to the number of Si atoms in the unreconstructed Si surface layer. It replaces the old value of 0.4 ML which could be found in the literature for years. In this new model Au atoms substitute for Si atoms in the topmost surface layer where they form two AuSi chains oriented along the $[1\bar{1}0]$ direction of the surface.
For the determination of the accurate Au coverage, two samples, in this case Si(557) and Si(111), are mounted on a sample holder next to each other (Fig. 2.11). The simultaneous Au evaporation ensures the same coverage on both samples. The coverage is optimized until an ideal Si(557)-Au structure is observed. On the Si(111) sample, 5×2 patches coexist with plain 7×7 reconstruction. Using an semiautomated image processing that recognizes the

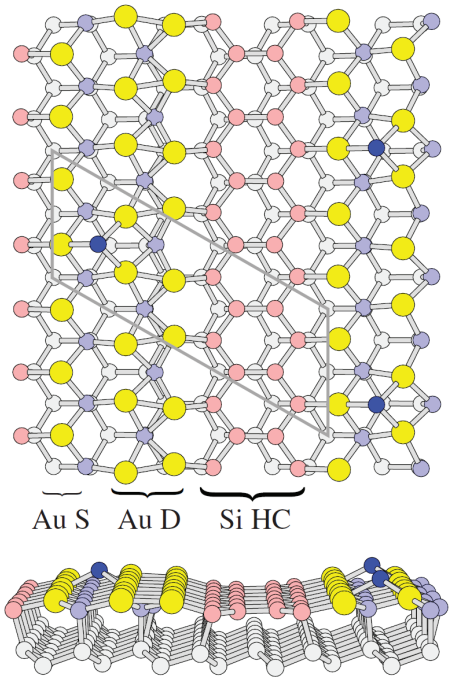

Figure 2.10.: Structural model of the Si(111)5×2-Au reconstruction. The yellow circles represent the Au atoms, the smaller circles the Si atoms. The surface layer consists of a gold single row (S), a gold double row (D) and a silicon honeycomb chain (HC). The surface energy is minimized when this surface is decorated by silicon adatoms (dark blue) with 5×4 periodicity. In the presence of adatoms the 5×1 periodicity of the underlying substrate spontaneously doubles to 5×2 (grey outline) due to dimerization within the gold double row. [79]

different surface reconstructions, the fraction of the 5×2 patches could be determined. By comparing the value with the Si(557) sample, the coverage of $0.615 \pm 0.040 ML$ was found [80].

A pseudo 3D image of the 5×2 surface is shown in Fig.2.12. The one-dimensional character of the reconstruction can be clearly seen from the chains pointing to the back of this view. An ideally covered 5×2 surface is shown in Fig. 2.13. Here the chains are pointing from the bottom left to the top right. Due to the size of the scan area only the adatoms are visible in this measurement as light spots.

At coverages lower than 0.6 ML, the system separates into patches of 5×2 and regions of bare 7×7. Figure 2.14 shows a topographic image of a such a partly covered surface. At negative gap voltages the Si adatoms (bright protrusions in the dark region) are the most prominent features of the 5×2 patch. The coexistence of both surface reconstructions on the sample allows the simultaneous investigation of both structures.

The electronic properties of the 5×2 have been investigated in several works. Compared to the plain 7×7 surface, the 5×2 reconstruction is known to show a metallic behavior. Yoon *et al.* [81] proposed, based on STM and STS investigations, that the 5×2 reconstruction con-

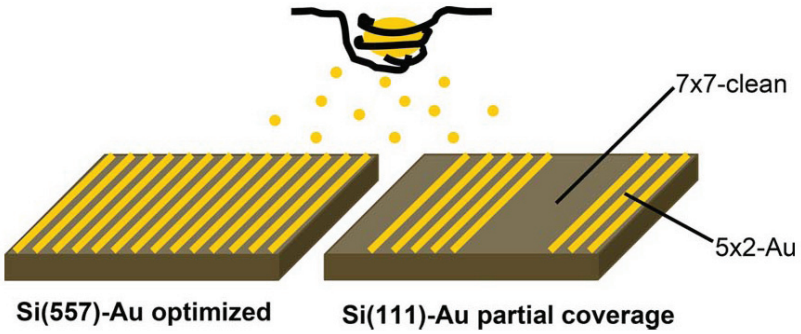

Figure 2.11.: Method for the coverage determination of Au chain structures on vicinal and flat Si samples. The Si(557)-Au structure with one Au chain per unit cell is used as reference. The same amount of Au is deposited on the Si(111). The relative areas of clean and Au-covered silicon uniquely determine the Au coverage. [80]

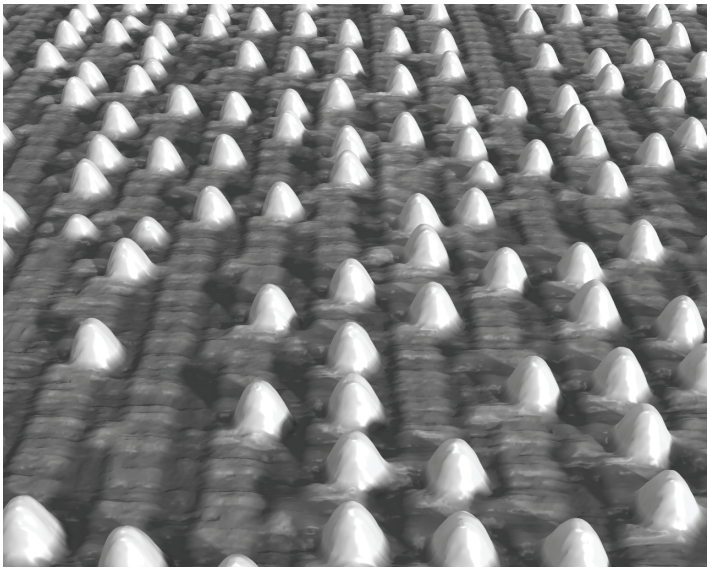

Figure 2.12.: After evaporation of Au onto the 7x7 reconstruction the Si(111)5x2-Au develops. The quasi one-dimensional chain structure can be seen as vertical lines, the Si adatoms appear as bright bumps.

sists of serially alternating metallic (without adatoms) and semiconducting (with additional Si adatoms) segments. This result was discussed by McChesney *et al.* [82], showing that the adatoms are not distributed in a 5×3 lattice, but they phase separate into 5×4 sections filled with adatoms.

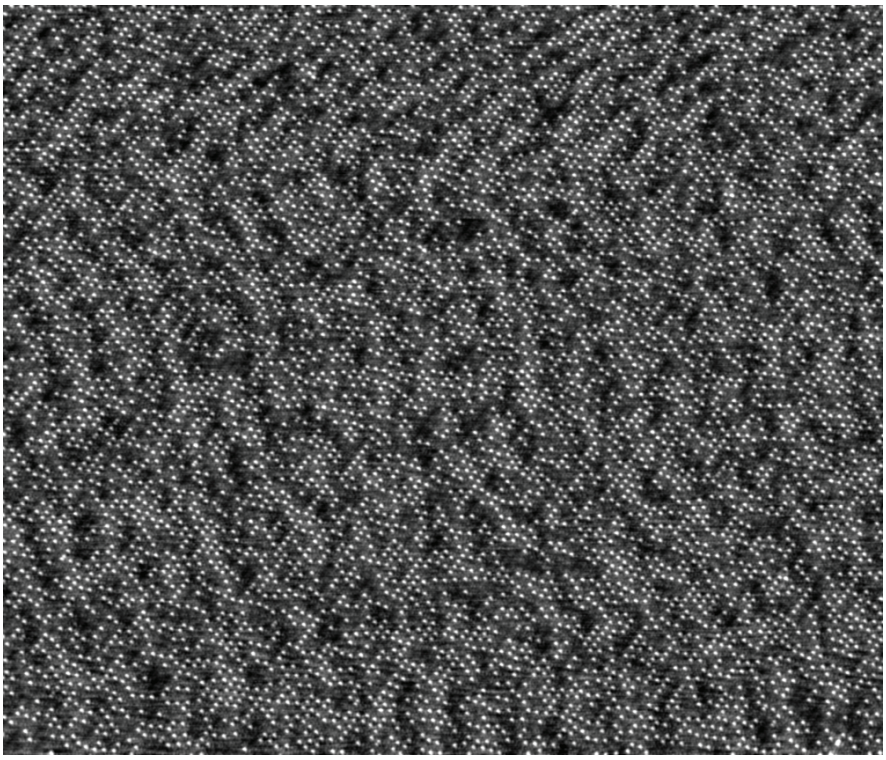

Figure 2.13.: Topographic image of an ideally covered 5×2-Au surface. The adatoms (bright spots) that are oriented in a direction from bottom left to top right indicate the one-dimensional character of the surface reconstruction (200 nm × 170 nm, $U_{gap} = -0.8$ V, $I_T = 5$ pA).

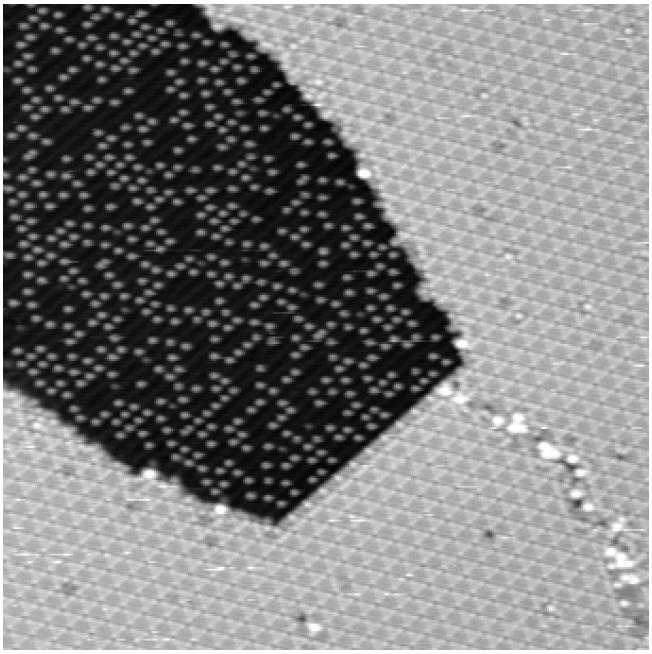

Figure 2.14.: Topographic image of a Si(111)5×2-Au patch (dark area) coexisting next to the patches of Si(111)7×7 (bright area) (80 nm × 80 nm, $U_{gap} = -2.0$ V, $I_T = 20$ pA).

2.6. Scanning tunneling microscopy

The scanning tunneling microscope (STM) became one of the most popular methods in surface science soon after it was developed in 1982 by Binnig and Rohrer [83]. It provides access to real-space imaging at the sub-nanometer scale of surfaces and nano-sized structures and even to spectroscopic applications with a high spatial resolution. Just four years after the invention, in 1986, the STM was awarded with the Nobel prize of physics showing the importance for the science community of this method. However, the technique and method of the STM were not completely new. About 10 years earlier, in 1972, Young *et al.* [84] proposed a machine called "Topografiner", quite similar to the STM but with the difference that it was based on field emission. Unfortunately this project ran out of money and was abandoned soon.

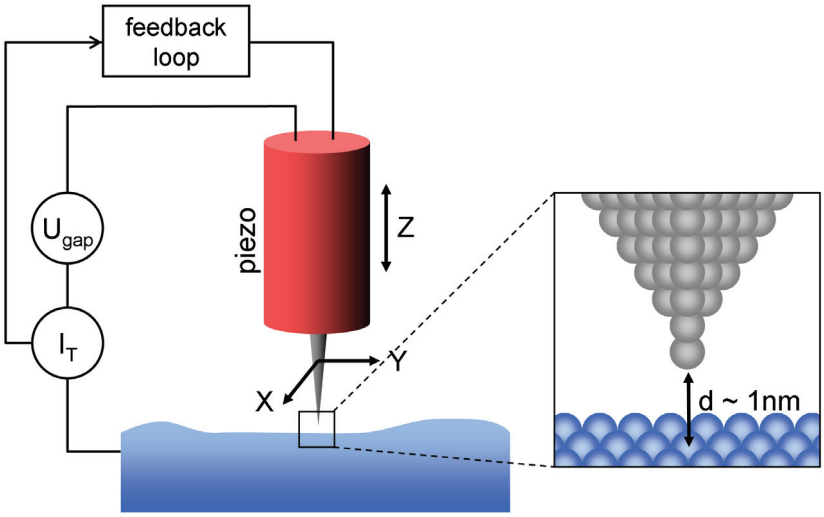

Figure 2.15.: Schematic view of the STM operation. See text for details.

A schematic view of the STM principle can be seen in Fig. 2.15. A conducting tip is brought near (less than 1 nm) to a conducting or semi-conducting surface. When the distance is small enough the tip and sample are in a tunneling contact. This is due to a quantum-mechanical effect called "quantum tunneling" or "tunnel effect", that will be described in the next section. Now if a bias voltage U_{gap} is applied between tip and sample, a tunneling current I_T can be measured, although both are not in physical contact. This tunneling current is the main quantity to be measured, providing access to imaging and spectroscopic applications. The three-dimensional motion of the STM tip is realized by using piezo elements allowing a precise movement on the sub-nanometer scale. The motion in the Z direction is controlled by a feedback loop that regulates the distance between tip and sample by evaluating the measured tunneling current. Normally the STM is operated in the "constant current mode". At a given gap voltage, the tunneling current is set to a fixed value, which is called the setpoint. Now the Z piezo is adjusted so that the actual tunneling current matches the setpoint

conditions. The changing of the Z piezo voltage is then used to get a height information of the sample. Another mode of operation is the "constant height mode" where the Z piezo is at a fixed position and the changing tunneling current is imaged as a function of the position. This mode can be used on very flat surfaces and provides the possibility of higher scan speeds.
When using the STM for topographic imaging, the imaged objects are always a convolution of their own shape and the shape of the tip [85, 86, 87]. Therefore only information about the object height can be reliably extracted from the measurements. However, even the measured height depends on the actual setpoint conditions, e.g. the gap voltage. Hövel and Barke [88] showed that in the normal range of the gap voltage during topographic imaging ($U_{gap} < 2$ V), the measured height leads to underestimated values of less than 10%. As this error is in the range of the STM scanner calibration error, it can be normally neglected.
In Fig. 2.16 the energetic scheme of the tip-sample system is plotted for three possible situations:

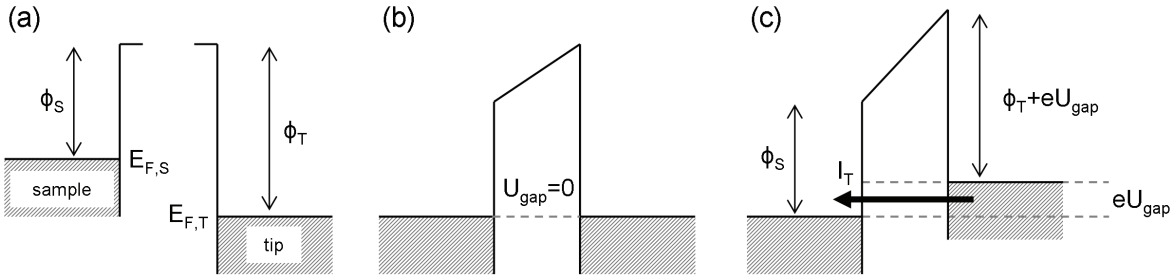

Figure 2.16.: Energetic view of the tip-sample system in a trapezoidal barrier model: (a) non-contact, (b) in tunnel contact with equilibrium conditions and (c) tunneling contact with applied gap voltage U_{gap}

(a) Tip and sample are far from each other and without any contact. The Fermi level of the tip $E_{F,T}$ is different than the Fermi level of the sample $E_{F,S}$.

(b) Tip and sample are in the tunneling contact with a distance of some Å. As a result the two Fermi levels equalize.

(c) A gap voltage (or bias voltage) U_{gap} is applied between tip and sample so that the Fermi level of the tip (in this case) is shifted upwards. Electrons from the occupied states of the tip can now tunnel through the vacuum barrier into the unoccupied states of the sample (or vice versa at a reverse polarity of the gap voltage). As a result, a tunneling current I_T can be measured.

The derivation of the expression for the tunneling current will be shown in section 2.6.2. Apart from topographic imaging the STM also provides access to spectroscopic applications by performing scanning tunneling spectroscopy (STS), which will be described in section 2.6.3.

2.6.1. Quantum tunneling

The STM is based on the principle of quantum tunneling. There are several approaches to describe the tunneling through an energetic barrier. The very basic one-dimensional model of the tunnel effect is sketched in Fig. 2.17. Here a single particle is assumed to tunnel elastically through a rectangular barrier. In the view of quantum-mechanics an electron of the energy E has a finite probability to tunnel through a potential barrier of the energy E_0 and the width d.

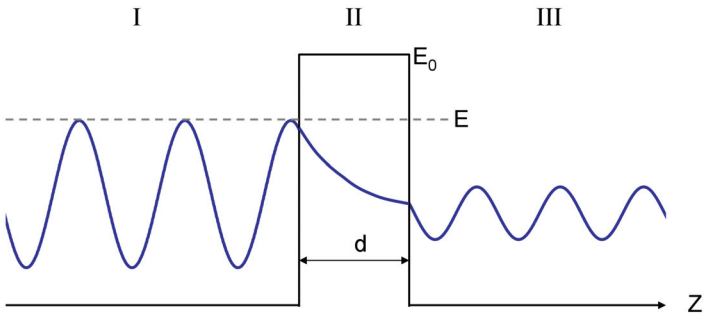

Figure 2.17.: A quantummechanical particle, like an electron, with the energy E has a probability to tunnel through a potential barrier of the E_0.

The process can be described by the time-independent Schrödinger equation for the three regions I, II and III.

$$-\frac{\hbar^2}{2m}\frac{d^2\Psi_I}{dz^2} = E\Psi_I \tag{2.19}$$

$$-\frac{\hbar^2}{2m}\frac{d^2\Psi_{II}}{dz^2} + E_0\Psi_{II} = E\Psi_{II} \tag{2.20}$$

$$-\frac{\hbar^2}{2m}\frac{d^2\Psi_{III}}{dz^2} = E\Psi_{III} \tag{2.21}$$

The interesting property of the tunneling barrier is the transmission coefficient T that describes the ratio of the transmitted current density j_{out} and the incident current density j_{in}:

$$T = \frac{|j_{out}|}{|j_{in}|} \tag{2.22}$$

T is often used for the description of the probability of the electron penetrating of the barrier. From the exact expression of T, that is shown e.g. in reference [89], and the assumption of a strongly attenuating barrier the transmission coefficient can be written as

$$T \propto \exp\left(-\frac{2}{\hbar}\sqrt{2m(E_0 - E)}\cdot d\right) \tag{2.23}$$

with m being the electron mass, E_0 being the energetic barrier height and E being the energy of the electron. From equation 2.23 one can see that the transmission through the barrier

depends exponentially on the squareroot of the effective potential barrier $\sqrt{2m(E_0 - E)}$ and from the width d of the potential barrier which is in our case the vacuum between tip and sample. This dependence on the barrier width is typical for tunneling, independent from the exact shape of the barrier. The one-dimensional barrier is, of course, only an approximation for understanding the basics of tunneling. In STM the tunneling junction is three-dimensional and of a more complex shape that the rectangular barrier.

2.6.2. The tunneling current

When tip and sample are in tunneling contact and a bias voltage is applied between them, a tunneling current in the range of pA to nA can be detected as a result of the tunnel effect. In topographic images the contrast is based on variations in the tunneling current.
In the approach of Tersoff and Hamann [90], the tunneling current is calculated with a perturbation theory. The geometry of the tunneling contact is simplified with a spherical tip with the radius R, positioned in the distance d above the sample (Fig. 2.18).

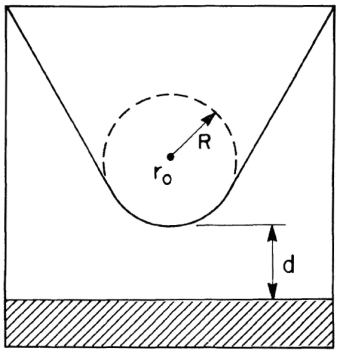

Figure 2.18.: Assumed tunneling geometry after Tersoff and Hamann [90]. The tip is assumed locally spherical with the radius of curvature R and the center r_0. The distance between tip and sample is denoted with d.

In his work, Bardeen [91] describes the transfer-rate η of electrons between two electrodes with the states Ψ_μ and Ψ_ν

$$\eta = \frac{2\pi}{\hbar}|M_{\mu,\nu}|^2\rho_\nu \tag{2.24}$$

with $M_{\mu,\nu}$ being the tunneling matrix element, that describes the states that are involved in the tunneling process, and ρ_ν the energy density of final states. According to Bardeen, the matrix element is given by

$$M_{\mu,\nu} = \frac{-\hbar^2}{2m}\int_S dS \cdot (\Psi_\mu^*\nabla\Psi_\nu - \Psi_\nu\nabla\Psi_\mu^*) \tag{2.25}$$

Under a forward bias voltage U_{gap}, the current can be evaluated with the 1D transfer-hamilton formalism by Bardeen [91] using a 1st order time-dependent perturbation theory:

$$I_T = \frac{2\pi e}{\hbar} \sum_{\mu,\nu} \{f(E_\mu)[1 - f(E_\nu + eU_{gap})] - f(E_\nu + eU_{gap})[1 - f(E_\mu)]\} \cdot \\ \cdot |M_{\mu,\nu}|^2 \delta(E_\nu - E_\mu) \quad (2.26)$$

where $f(E)$ is the Fermi function, U_{gap} is the bias voltage applied between tip and sample, $M_{\mu,\nu}$ is the element of the tunneling matrix between the unperturbated states ψ_μ of the tip and ψ_ν of the sample and E_μ (E_ν) is the energy of the states ψ_μ (ψ_ν) in the non-contact regime. Under the consideration of low temperatures and a small applied bias voltage the tunneling current reduces to

$$I_T = \frac{2\pi e^2}{\hbar} U \sum_{\mu,\nu} |M_{\mu,\nu}|^2 \delta(E_\nu - E_F) \cdot \delta(E_\mu - E_F) \quad (2.27)$$

Within the s-type wavefunction of the spherical tip, the tunneling current can be written as [89]

$$I_T \propto U_{gap} \cdot n_t(E_F) \cdot exp(2\chi R) \cdot \sum_{\nu} |\Psi_\nu(\vec{r_0})|^2 \delta(E_\nu - E_F) \quad (2.28)$$

where χ is the decay rate, $n_t(E_F)$ is the density of states at the Fermi level of the tip, R is the effective tip radius and $\vec{r_0}$ is the vector pointing to the middle of the spherical tip. However, the wave function of real tips is more complex, so this approach is only a very simple approximation. From equation 2.28 the quantity

$$n_s(E_F, \vec{r_0}) = \sum_{\nu} |\Psi_\nu(\vec{r_0})|^2 \delta(E_\nu - E_F) \quad (2.29)$$

can be identified as the local density of states (LDOS) of the sample surface at the Fermi level E_F at the center $\vec{r_0}$ of the tip. With the information that wave functions decay exponentially at the surface in the z-direction to the vacuum barrier, one finds that

$$I_T \propto exp\left(-\frac{2}{\hbar}\sqrt{2m(E_0 - E)} \cdot d\right) \quad (2.30)$$

which describes the exponential dependence of the tunneling current I on the barrier width d, which is the distance between the tip and the sample. This exponential behavior allows the detection of irregularities of the sample surface on a sub-nanometer scale. From the similar proportionality of equation 2.30 and 2.23 it is obvious that the tunneling current I_T is also proportional to the transmission coefficient T.
However, the interpretation of Tersoff and Hamann is only valid for low bias voltages and a s-type tip wave function. A generalized expression for finite voltages can be approximated using the derivations from [89]:

$$I_T \propto \int_0^{eU_{gap}} n_t(\pm eU_{gap} \mp \mathscr{E}) \cdot n_s(\mathscr{E}) \cdot T(\mathscr{E}, eU_{gap}) d\mathscr{E} \quad (2.31)$$

where n_t is the DOS of the tip, U_{gap} being the gap voltage, n_s the DOS of the sample and $T(\mathscr{E}, eU_{gap})$ the transmission coefficient that depends on the energy $\mathscr{E}$ and the applied gap voltage U_{gap}. From equation 2.31 it is obvious that the tunneling current contains both information of the density of states of the tip and the sample. This is especially important when using the STM for spectroscopic measurements.

2.6.3. Scanning tunneling spectroscopy

Next to the application of obtaining nanoscale topographic images of the sample surface, the STM also provides access to different spectroscopic applications. In scanning tunneling spectroscopy (STS) [92] the STM is used for spectroscopic investigations of the electronic surface properties. For STS, the tip is moved to a certain location that is manually selected or given by a fixed grid of distances within the scan area. At this position the tip movement is halted while the spectroscopy is performed, resulting in spatially resolved spectroscopic data. The spatial resolution depends on the selected distance between the single measurements. There are several types of spectroscopy that can be performed with the STM. In the following, only two of them will be described as they are the most important for this work.

I(V) - conductance spectroscopy: At a certain location on the sample the tunneling current I_T is measured as a function of the bias voltage U_{gap}. The resulting $I(V)$ curve gives information about the conductance of the sample at this location. For example, on a semiconducting sample the width of the energy gap can be determined in a first approach from an $I(V)$ curve. In this work, the $I(V)$ spectroscopy is used for obtaining the laser-induced SPV of the samples.

dI(V)/dV - differential conductance spectroscopy: When considering a constant transmission coefficient, equation 2.31 reduces to

$$I_T \propto \int_0^{eU_{gap}} n_t(\pm eU_{gap} \mp \mathscr{E}) \cdot n_s(\mathscr{E}) d\mathscr{E} \tag{2.32}$$

showing that the tunneling current is a convolution of the DOS of the tip and the sample. Now assuming that the tip DOS n_t is constant during the measurement, the following relation can be made

$$\frac{dI}{dV} \propto n_s(\mathscr{E}, U_{gap}) \tag{2.33}$$

So for ideal measurement conditions, the differential conductance dI/dV is directly proportional to the sample DOS and thus provides information about the sample local density of states (LDOS) at a given voltage. This is, of course, only valid if the electronic structure of the tip does not change during the measurement.

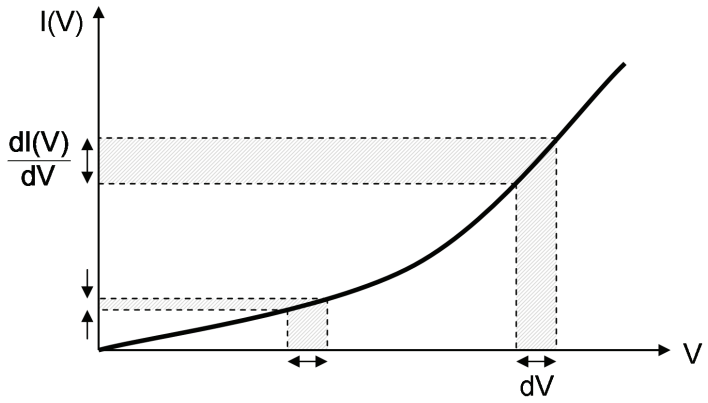

Figure 2.19.: Measuring the differential conductance with a lock-in amplifier: modulating the gap voltage with dV, results in a dI/dV signal that depends on the slope of the curve.

One way to obtain the differential conductance is by numerical differentiation of the recorded $I(V)$ spectra. Another quite simple method has been established as a standard technique: the differential conductance is directly obtained during the STS measurement by using an additional lock-in amplifier. The lock-in generates a small modulation voltage dV that is added to the bias voltage: $U' = U_{gap} + dV$. From the resulting tunneling current I_T the lock-in detects the modulation signal and gets the dI/dV signal as a result. This signal directly depends on the slope of the $I(V)$ curve as it is shown in Fig. 2.19. With this method the differential conductance can be directly measured during normal $I(V)$ spectroscopy.

2.6.4. Measuring the surface photovoltage with STM

With the help of the STM (section 2.6) one can also get access to the direct measurement of the surface photovoltage. One of the first STM assisted SPV investigation was done in 1990 by Hamers and Markert [21]. They used a double feedback technique, where at every pixel of the image the feedback loop of the constant-current mode is switched to a specific SPV mode. A second feedback loop is used to keep the Z position of the piezo constant while the gap voltage is adjusted by nulling the tunneling current. The found difference in the gap voltage directly corresponds to the induced photovoltage U_{SPV}.
One year later, in 1991, Cahill and Hamers [93] used a chopped laser beam that creates a modulating SPV ΔU_{SPV} inducing a modulation of the tunneling current $\Delta I = (dI/dV)\Delta U_{\text{SPV}}$. This modulation is then measured with a lock-in amplifier. A second lock-in measures the differential conductivity dI/dV. By dividing these two signals one directly obtains the value of the modulated SPV.
Another way for SPV determination was presented by Kochanski and Bell [94] in 1992. Their idea was to measure the tunneling current at every position in the image at a fixed Z position for two different gap voltages. The first gap voltage is the measured SPV from the previous position and the second at the value of a reference tunneling current. A linear

interpolation to $I_T = 0$ directly delivers the SPV for that position. This method is said to have an uncertainty of about 10 mV and a speed of about 10 ms per position (pixel).
In 1998, Hagen *et al.* [95] used a modified version of the technique introduced by Hamers and Markert. Here the SPV feedback and the Z regulation work simultaneously. The gap voltage is adjusted by the SPV feedback to null the tunneling current. This method directly outputs the SPV value. Instead of using the tunneling current, the Z regulation uses the differential conductivity dI/dV measured by a lock-in amplifier.
The previous methods have all their specific assets and drawbacks. The methods that use a feedback at the zero crossing of the $I(V)$ curve rely on the assumption that there is enough conductivity dI/dV at the region of zero crossing. But this is only working for semiconductors having a large density of surface states within the band gap. The methods using chopped laser light suffer from the side-effect of thermal expansion of the tip-sample system adding a current modulation, that is linearly depending on the laser power, to the tunneling current due to the linear thermal expansion of the tip and sample materials [95, 96]. Another problem of chopped methods is the decay time of the SPV. On certain samples this decay can become rather long which limits the chopping frequency of the laser [97].

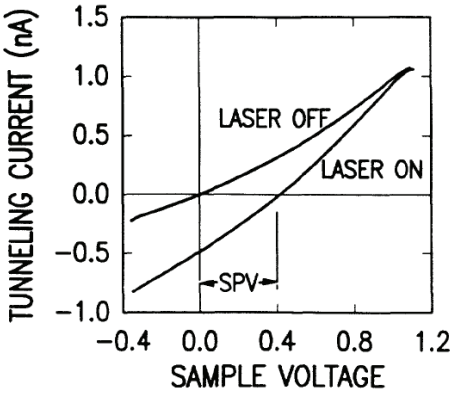

Figure 2.20.: I(V) curves ($U_{gap} = 1.2$ V) in equilibrium and under laser illumination. The shift of the zero-crossing corresponds to the induced surface photovoltage and directly reflects the exact value [21].

The measured SPV can be changed by external electrical fields, e.g. the field between the STM tip and sample. McEllistrem *et al.* [98] systematically investigated the dependence on the gap voltage and found that on semiconductors surfaces with a weak Fermi-level pinning, i.e. Si(001)2×1 or H-Si(111), the tip potential induces an additional band bending resulting in a modified SPV. On the other hand, on the Si(111)7×7, the SPV is almost unaffected by the electrical field as the field is completely screened by the surface states.
In this work normal $I(V)$ spectroscopy is used for the determination of the surface photovoltage. Under illumination, the whole $I(V)$ curve shifts along the voltage axis as if an additional external bias voltage is applied to the sample: $I'(V) = I(V + SPV)$. The shift directly reflects the value of the induced surface photovoltage, as it is shown in Fig. 2.20.

By analyzing the shift of the zero-crossing for situations without and with illumination, the value of the SPV can directly be obtained from the $I(V)$ curves. Although this method suffers from being extremely time-consuming, particularly for spatially-resolved SPV maps, it is less prone to the spurious artifacts discussed above. Additionally, no further devices like a second feedback loop or lock-in amplifiers are needed, making this method available by using a standard STM setup.

2.6.5. Field emission resonances

Another aspect of STM measurements is the usage of larger bias voltages, in the range of $U_{gap} = 3...10$ V. In this regime the STM operates in the mode of field emission, also called Fowler-Nordheim tunneling [99]. This mode is used in this work for observing field emission resonances (FER) that are sensitive to changes in the local work function (LWF) of the sample.
Considering a metal surface, the interaction of charge carriers with the nearby surface can be described by an image charge model. In this model an attractive image potential binds an electron that has been emitted from the surface. In a semi classical approach, distinct energy levels are formed in the potential well between the surface and the vacuum due to phase matching reflection conditions (Fig.2.21a). These discrete standing waves are known as image states [100].

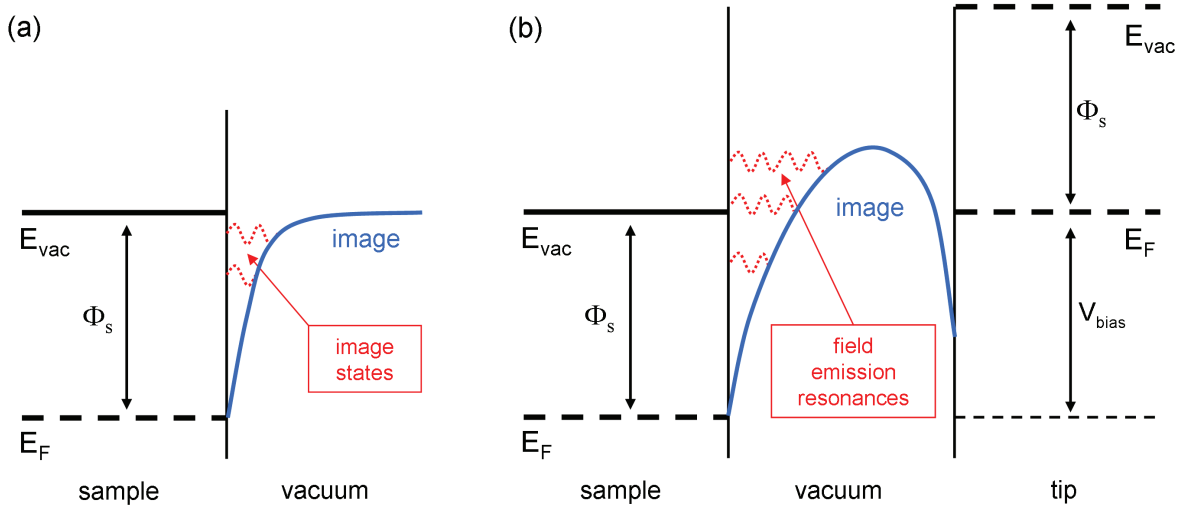

Figure 2.21.: Schematic view of the origin of the field emission resonances. (a) image states form in the potential well near the surface, (b) the STM tip modifies the image potential, so that field emission resonances appear for large bias voltages.

When in STM the tip is brought close to the surface and a bias voltage is applied between them, the shape of the image potential is modified as it is shown in Fig.2.21b. For large voltages ($U_{gap} > 3...4$ V) discrete electronic states are allowed to exist even above the

vacuum level. These states are leading to the FER that can be easily observed by STS. They appear as oscillations of the differential conductivity dI/dV versus bias voltage U_{gap} with enabled feedback loop. Jung *et al.* [101] showed that the energetic position of these oscillations is strongly determined by the local work function (LWF). Thus the FER can be used to investigate qualitatively differences in the LWF on the sample.

2.7. Grazing-incidence small-angle X-ray scattering

With STM it is only possible to investigate a finite area on the surface containing only individual or a small amount of objects, i.e. deposited nanoparticles in this work. In some experiments this is a huge advantage, but if you need information averaged over many particles it is quite difficult to achieve. A completely different method that can be used for characterizing deposited clusters is the grazing-incidence small-angle X-ray scattering (GISAXS) [102]. It was first introduced in 1989 by Levine *et al.* [103] for studying the growth of thin films by combining the surface sensitivity of grazing incidence diffraction (GID) with the access to small lengthscales of small-angle X-ray scattering (SAXS). But instead of using a transmission geometry like SAXS, GISAXS works in reflective geometry. For the investigation of the morphology of deposited nanoparticles, GISAXS offers the opportunity to probe an assembly of nanoparticles as a whole and to define an "averaged particle". Not only the sizes and the particle density can be obtained, also others quantities like the particle shape, the width of the size distribution or higher order correlation parameters are hidden in the scattering profile [104].
The schematic view of a GISAXS experiment is shown in Fig.2.22. A monochromatic X-ray beam of the wavevector $\mathbf{k_i}$, with the wave number $k_0 = 2\pi/\lambda$, is directed at the sample at a small angle α_i. The beam is scattered along $\mathbf{k_f}$ in the (θ_f, α_f) direction. The scattering originates from electron density fluctuations within the illuminated part of the sample. In our case these are not only the deposited cluster but also the sample surface itself.
By evaluating horizontal (blue line in Fig.2.22) and vertical (green line) cross-sections (or cuts) of the scattering image information about the particle height and width, respectively, can be obtained. GISAXS is an integral method that is "looking" at a huge area of the sample, namely an area corresponding to the projected beam diameter. Therefore the obtained information does not characterize one single particle but averages over a whole particle ensemble. Due to the high number of particles results from GISAXS, e.g. about the particle size, have a high statistical relevance.
In the shown scattering geometry the scattering wavevector $\mathbf{q}$ for the three spatial dimensions can be written as

$$\mathbf{q} = (q_x, q_y, q_z) = \frac{2\pi}{\lambda} \begin{bmatrix} \cos(\alpha_f)\cos(\theta_f) - \cos(\alpha_i) \\ \sin(\theta_f)\cos(\alpha_f) \\ \sin(\alpha_i) + \sin(\alpha_f) \end{bmatrix}. \tag{2.34}$$

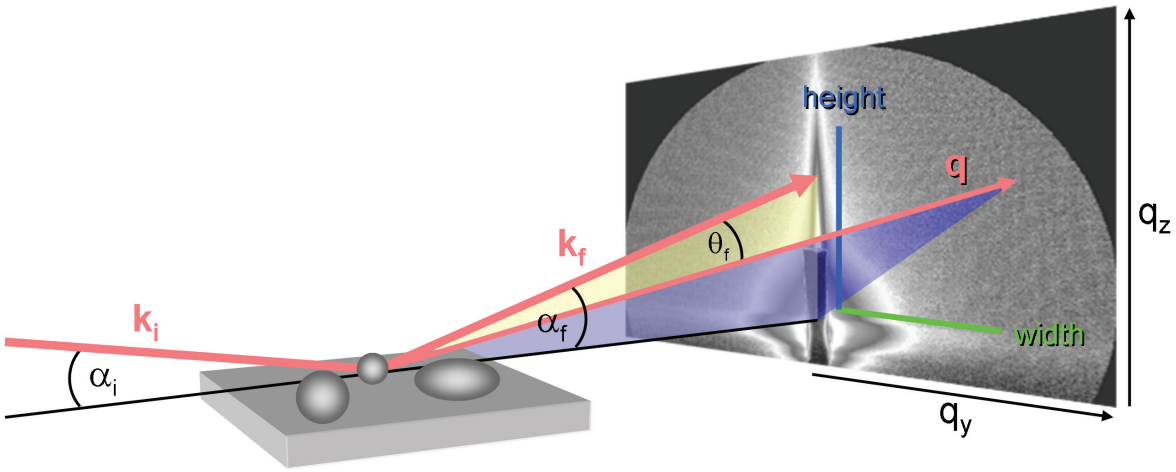

Figure 2.22.: Geometry of a GISAXS experiment on deposited particles. See the text for details.

where α_f is the angle between the forward scattered beam $\mathbf{k}_f$ and the sample horizon and θ_f is the angle between $\mathbf{k}_f$ and the scattering wavevector $\mathbf{q}$. In a GISAXS experiment the experimental data, which is a function of (θ_f, α_f), is recorded as a 2D pattern of the ($q_\parallel = q_y, q_\perp = q_z$) reciprocal plane. A typical pattern features two sharp peaks originating from the specularly reflected beam and a beam occurring due to transmission through the sample. These beams are normally suppressed by a beam blocker to avoid damage to the detector. The sample surface (z = 0) is called the "horizon".
The theoretical description of GISAXS experiments is more complex than normal X-ray experiments. Due to the shallow scattering angle, the reflection and refraction at the interfaces and roughness scattering can not be neglected in the scattering process. Therefore multiple scattering effects have to be considered. This leads to the currently most popular theory for GISAXS called "distorted wave born approximation" (DWBA) [105, 106, 107]. Here the roughness of the surface is viewed as a perturbation of a known reference, e.g. a flat interface. The scattering cross-section can be expressed as

$$\frac{d\sigma}{d\Omega} = \frac{k_0^4}{16\pi^2} \left|n_p^2 - 1\right|^2 \left|\mathscr{F}(\mathbf{q}_\parallel, k_{iz,0}, k_{fz,0})\right|^2 \tag{2.35}$$

where the DWBA form factor of the nanoparticle is given by

$$\begin{aligned}\mathscr{F}(\mathbf{q}_\parallel, k_{iz,0}, k_{fz,0}) = F(\mathbf{q}_\parallel, k_{fz,0} - k_{iz,0}) + r_{0,1}^f F(\mathbf{q}_\parallel, -k_{fz,0}, k_{iz,0}) \\ + r_{0,1}^i F(\mathbf{q}_\parallel, k_{fz,0} + k_{iz,0}) + r_{0,1}^i r_{0,1}^f F(\mathbf{q}_\parallel, -k_{fz,0} + k_{iz,0})\end{aligned} \tag{2.36}$$

with $\mathbf{q} = \mathbf{k}_f - \mathbf{k}_i$ being the wavevector transfer and $\mathscr{F}(\mathbf{q}_\parallel, k_{iz,0}, k_{fz,0})$ being the Fourier transform of the particle shape:

$$F(\mathbf{q}) = \int_{S(\mathbf{r})} e^{i\mathbf{q}\cdot\mathbf{r}} d\mathbf{r} \tag{2.37}$$

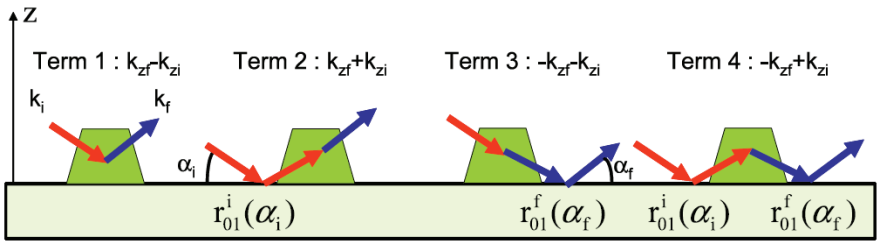

Figure 2.23.: Representation of equation 2.36, showing the different types of interactions with an object. It should not be interpreted as geometrical X-ray paths, but more as a schematic representation. [104]

Equation 2.36 contains the different possible scattering paths occurring on deposited nanoparticles. These paths are sketched in Fig. 2.23.
For particles with a polydisperse size distribution the scattering intensity can be expressed as the product of the structure factor $S(\mathbf{q})$ and the form factor $F(\mathbf{q})$ [28]

$$I(\mathbf{q}) = S(\mathbf{q})[F(\mathbf{q})]^2 \tag{2.38}$$

The structure factor S includes information on the crystal lattice parameters, orientation and dimension, whereas the form factor F provides the shape, size and orientation of the nanoparticles. The intensities and amplitudes of the form factor are known for different particle shapes from calculations [108, 109]. The structure factor of isotropic colloid-like objects is also available from literature [108, 109]. Due to the higher complexity of this multiple scattering, supporting results from other techniques, e.g. like AFM or TEM, are helpful to resolve the exact scattering cross section in the analysis afterwards.
Fig. 2.24 shows a recorded GISAXS pattern and the different regions resulting from different effects. The blue region marks features originating from the sample horizon and the substrate itself. Next to this scattering an enhancement of the intensity can be found at an exit angle close to the angle of total external reflection, which is the critical angle. This intensity peak is called "Yoneda peak" [110]. The green region originates from anomalous surface reflection of the sample horizon. Both regions are of less importance here as they contain no information about the particles. The region marked with the red circle is the region of main interest in this work. Here the features originating from the particle scattering can be found.
A helpful tool in understanding GISAXS images is the simulation of the scattering pattern. This can be done e.g. with the software IsGISAXS [109]. From these simulations, that are based on a known or approximated sample and particle geometry, the scattering images can be easily generated and compared to the experimental data.
A simulation done by Renaud *et al.* [104] is depicted in Fig. 2.25. It shows the scattering pattern of a square basis pyramidal particle for two orientations ξ of the incoming beam with respect to the base edge: (a) $\xi = 0°$, (b) and (c) $\xi = 45°$. Patterns "a" and "b" correspond to an isolated particle, while in pattern "c" a size distribution was assumed. The cluster is limited by (111) and (001) facets that make an angle of $54.7°$. A directional scattering

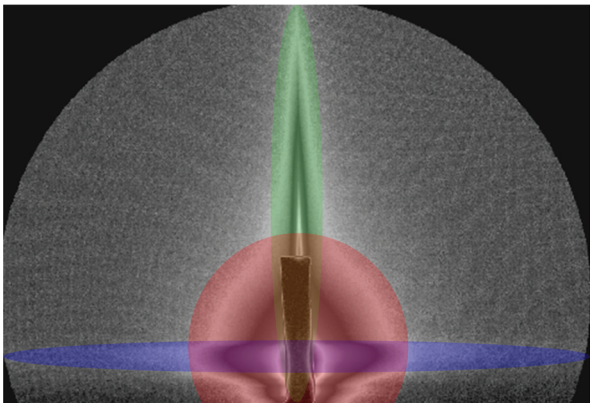

Figure 2.24.: The different regions of a GISAXS pattern: the blue region shows features originating from the sample horizon and the substrate itself. The green region comes from forward scattering and is less important in this work. The red region shows features from the deposited particles.

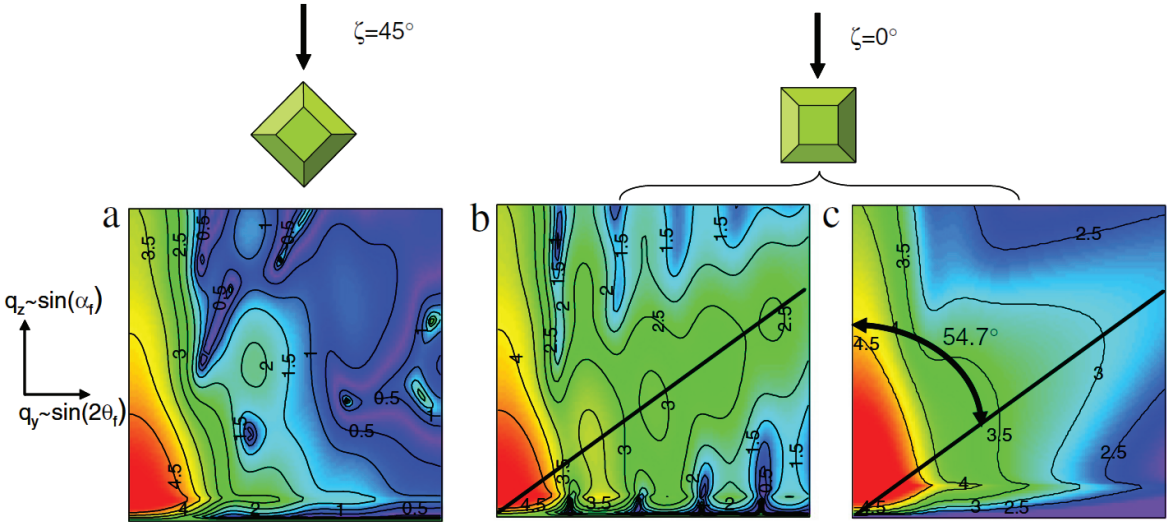

Figure 2.25.: Simulated GISAXS pattern of a square basis pyramidal island for two orientations ξ of the incoming beam with respect to the base edge: (a) $\xi = 0°$, (b) and (c) $\xi = 45°$. Patterns "a" and "b" corresponds to an isolated particle while for pattern "c" a size distribution was assumed. [104]

rod tilted by $54.7°$ from the surface normal shows up when the beam is aligned along the particle edge (Fig. 2.25b). This directional scattering feature decreases progressively upon rotation (Fig. 2.25a) and when the the size distribution of the particles gets broadened. This beautifully demonstrates that it is possible to investigate the facets of nanoparticles by using GISAXS.

In the last years, GISAXS became a popular instrument in surface science and physical chemistry. It has been used in several investigations on nanosized objects such as deposited nanoparticles [111, 112], grown clusters [113, 114] or islands [115]. Besides static samples

and real time measurements, the so called "micro-beam GISAXS" with a scanning sample position was developed by Roth *et al.* [116] providing spatial resolved measurements. In 2007, Vartanyants *et al.* [117, 118] showed coherent GISAXS measurements of nano-sized islands. With a direct inversion of the data by an intensive calculation, they were able to reproduce a reliable real-space image of the shape of the islands from the GISAXS data. So it is not only possible to measure structural properties of the sample, but even to reconstruct the shape and characteristics of the sample into a real-space image.

2.7.1. Analyzing GISAXS images

The resulting two-dimensional GISAXS images can be analyzed by taking cross sections in the q_y direction for horizontal information and in the q_z direction for vertical information. The scattering vector q is calculated from $(4\pi/\lambda)\sin\theta_f$, where θ_f is the scattering half angle and λ is the wavelength of the X-rays. When the size distribution of the particles is known, a scattering pattern can be fitted with calculated intensities based on different modeled shapes. The size distribution that can be used is e.g. the Schultz distribution representing a system of polydispersed spheres [119]. As the here used Ag cluster are nearly uniform and approximately of spherical shape, the data can be analyzed by the Guinier analysis [120]. This method was developed by Guinier and Fournet in 1955 [121] for SAXS and provides the horizontal and vertical particle radius of gyration [1] $R_{g,H}$ and $R_{g,V}$ from which the size of the particles can be calculated. The radius of gyration R_g is given by the root mean square of the mass-weighted distances of all small volume elements in a particle from the center of mass:

$$R_g = \sqrt{\frac{\int_V r^2 \rho(\mathbf{r}) d^3\mathbf{r}}{\int_V \rho(\mathbf{r}) d^3\mathbf{r}}} \tag{2.39}$$

where $\rho(\mathbf{r})$ is the density of a small volume element of the particle at the location $\mathbf{r}$ from the center of the particle mass. For a homogeneous sphere of the radius R the scattering form factor is known as [120]:

$$P_S(q,R) = \left(3\frac{\sin(qR) - (qR)\cos(qR)}{(qR)^3}\right)^2 = \left[F_S(q,R)\right]^2 \tag{2.40}$$

In the range where $qR < 1$, when q tends to 0, Guinier [121] has shown that the scattering form factor $P(q)$ only depends on the radius of gyration of the particle R_g:

$$P(q) \propto V_p \exp\left(-\frac{(qR_g)^2}{3}\right) \tag{2.41}$$

where V_p is the volume of one of the N_p homogeneous isotropic scatterers in the unit volume V. With the help of this approximation it is possible to obtain geometric information by only

[1] The name "radius of gyration" has nothing to do with rotating (gyrating) a particle about some axis. It is used here in a different content as normally in science.

analyzing the scattering at small angles.
By plotting the logarithm of the intensity $\ln(I)$ as a function of q^2 one gets a linear function where the radius of gyration R_g^2 is given by the slope of the function:

$$\ln I = \ln I_0 - \frac{1}{3} R_g^2 q^2 \tag{2.42}$$

With the help of this equation, a cross-section cut from the GISAXS scattering image can be fitted by a linear function where the slope directly returns the radius of gyration. For a spherical particle the diameter and the height can be calculated as $2.58 \times R_{g,H}$ and $2.58 \times R_{g,V}$, respectively. The aspect ratio of the particles is given as $R_{g,H}/R_{g,V}$.

3. The experimental setups

In this chapter the setup and details of the different experiments are introduced and explained. First the preparation of the sample surfaces and the deposition process of the clusters are shown. Afterwards the setup of the STM supported SPV measurement including the general STM setup and tip preparation is presented, while in the last part the setup for the GISAXS experiment is illustrated.

3.1. Preparing the sample surfaces

In this work, Si(111) samples are used for several experiments. This surface is well known from various experiments in the past (cf. section 2.4), so the preparation of the Si(111)7×7 reconstruction in ultra-high vacuum (UHV) is a standard method in surface science. The samples that are used in this work are cut from Si(111) wafers, n-doped (Wafer-World Inc.) and p-doped (Crystec) with both a resistance of 0.2 Ωcm which equals an impurity concentration of about 3×10^{16} cm^{-3} (n-type) and 1×10^{17} cm^{-3} (p-type), respectively. For the experiments, the sample is cut into small strips with a size of about 3 nm ×10 mm and mounted on an Omicron standard sampleplate. This plate has been modified to allow a direct heating of the sample by applying a DC voltage on both edges of the sample. Brought into UHV via a load-lock system, the samples are degassed at 600 °C for several hours or even overnight in the UHV chamber. This allows the desorption of water molecules and other unwanted adsorbates from the surface. Afterwards the samples are flashed three to four times up to 1250 °C for a few seconds [122, 123] followed by a moderate cooling-down ramp. While the sample is cooling down, the surface reconstructs from the 1×1 to the 7×7 structure [62]. During the preparation, the temperature of the sample is measured with an infrared pyrometer from outside the chamber through a glass-window flange. After the preparation, the quality of the surface can be verified with low electron energy diffraction (LEED). But as LEED is an integral method, it only indicates the surface quality of large areas. The sample quality on the atomic scale can only be resolved afterwards in the STM.
The clean sample is then used for cluster deposition (described in the next section) or the preparation of the Si(111)5×2-Au reconstruction. Evaporation of less than 0.6 ML gold using an electron-beam evaporator (EVM-3, Focus / Omicron Nanotechnology) and post annealing to 850 °C results in patches of 5×2 that coexist with regions of the clean 7×7. By adjusting the amount of evaporated gold as well as the post-annealing temperature and time the size of the 5×2 patches can be tailored in a wide range to the needs of the experiment

[80]. Patches of 5×2 prepared for this work have approximately rectangular shape with areas in the range of 100...10000 nm^2 (cf. Fig. 2.14 before). After the preparation the sample are transferred into the STM where it is cooled down to 78 K for the experiments.

3.2. Arc cluster ion source: cluster deposition on atomically clean surfaces

In this work small nano-sized silver clusters are used in the different experiments. The Ag clusters are produced in an arc cluster ion source (ACIS) that is connected to the UHV system [124] which allows *in situ* cluster deposition on the substrate under clean UHV conditions. The schematic setup of the cluster source is shown in Fig. 3.1.

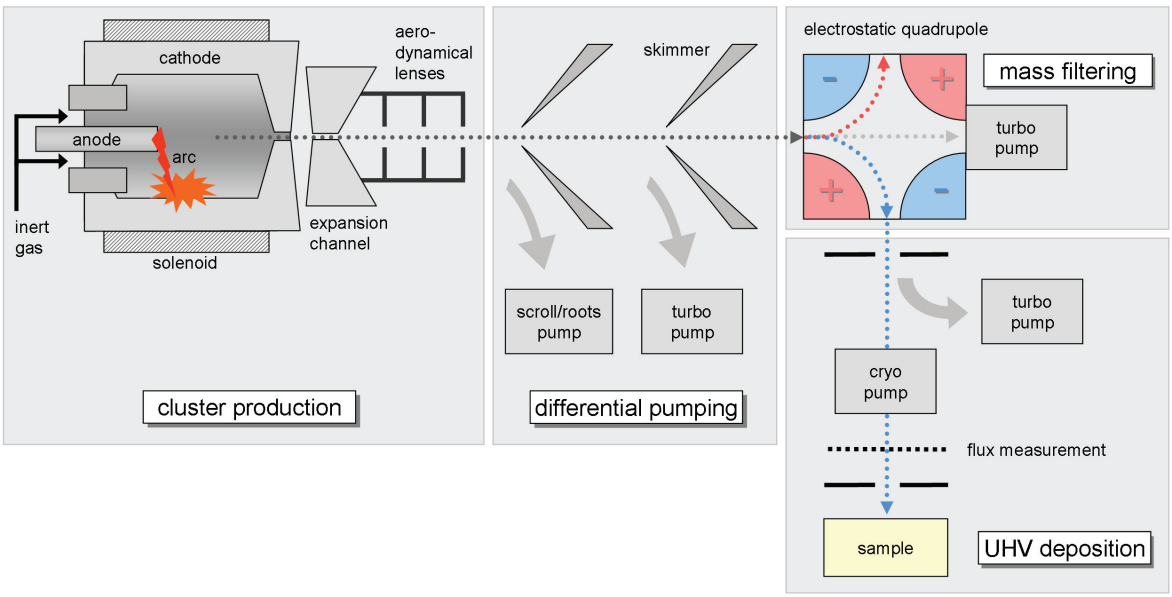

Figure 3.1.: Schematic view of the arc cluster ion source (ACIS) used for cluster production containing several pumping stages, the electrostatic quadrupole and the flux measurement.

In a cylindrical cathode, made out of pure silver in the case of Ag cluster, an arc is ignited by applying a high voltage between the cathode and the anode. As a result small aggregates of the cathode material are emitted and form a metal-vapor plasma in the high temperature environment. The cluster aggregation takes place in a rare gas atmosphere [125] of about 80% He and 20% Ar. Typical values of the gas flow through the cathode are 25 sccm [1] He and 8 sccm Ar, resulting in a total pressure of about 30 mbar within the cathode. Around the cathode, a solenoid is mounted generating a magnetic field, that causes the arc to rotate within the cathode so that the material is eroded uniformly. It showed up that when the

[1] 1 sccm = 1 standard cubic centimeter per minute gas flow

magnetic field is modulated, e.g. by a sinusoidal voltage, the arc can burn on one position for a short time before moving further, resulting in a short increased cluster production. The generated clusters, which include many sizes from small particles to even huge droplets, pass the expansion channel and a system of aerodynamical lenses. These lenses allow a collimation of the small clusters in the beam, leading to a size distribution moving to smaller cluster sizes [126]. In this region of the source the clusters are also cooled down. When passing the two skimmers, they are separated from the main part of the rare gas. In the following electrostatic quadrupole [127] the charged clusters are deflected by 90° and separated by their kinetic energy and charge:

$$E_{kin} = \frac{m}{2} \cdot v^2 = G \cdot n \cdot e \cdot |U_{Quad}| \tag{3.1}$$

where m is the mass and v the velocity and E_{kin} the kinetic energy of the clusters. G is a constant depending of the geometry of the quadrupole, $n \cdot e$ is a multiple of the elementary charge and $|U_{Quad}|$ is the voltage applied between ground (i.e. the whole cluster apparatus) and the respective quadrupole segments. Assuming the clusters have a spherical shape the relation 3.1 can be written as

$$\frac{v^2}{2} \cdot \rho \cdot \frac{\pi}{6} \cdot d^3 = G \cdot n \cdot e \cdot |U_{Quad}| \tag{3.2}$$

from which the following relation can be derived

$$d = A \cdot \sqrt[3]{|U_{Quad}|} \tag{3.3}$$

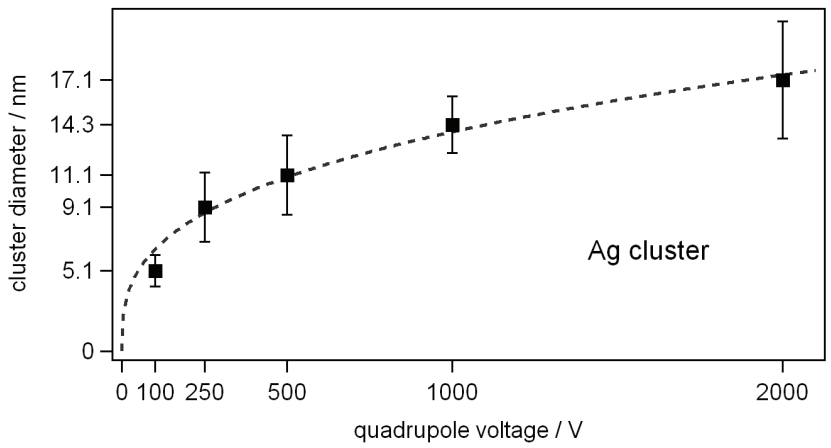

Figure 3.2.: The cluster diameter as a function of the applied quadrupole voltage. The dashed line shows a fit of the relation 3.3 with the fit parameter $A = 2.25$ nm/V$^{1/3}$.

with A being a proportional factor. The cluster diameter d is proportional to the third root of the quadrupole voltage U_{Quad}. This relation is fitted to the data points in Fig. 3.2, indicated by the dotted line: $d = 2.25$ nm/V$^{1/3}$ $\cdot \sqrt[3]{U_{Quad}}$. The data points in Fig. 3.2 represent results from TEM investigations where the diameter of the particles has been measured as a function

of the quadrupole voltage. A typical TEM image of Ag cluster produced with ±250 V is depicted in Fig. 3.3. The clusters appear as dark dots on the grey background, which is the amorphous carbon film of the TEM grid. From such TEM images size distributions are generated by statistical analysis. Figure 3.4 shows such distributions of the particle diameter for a ±250 V (left) and ±1000 V (right) deposition. The black curve represents a fitted Gaussian providing the mean diameter and its error by the width of the distribution. The resulting particle sizes are 9.1±2.2 nm for 250 V and 14.3±1.8 nm for 1000 V, which is also shown in Fig. 3.2.

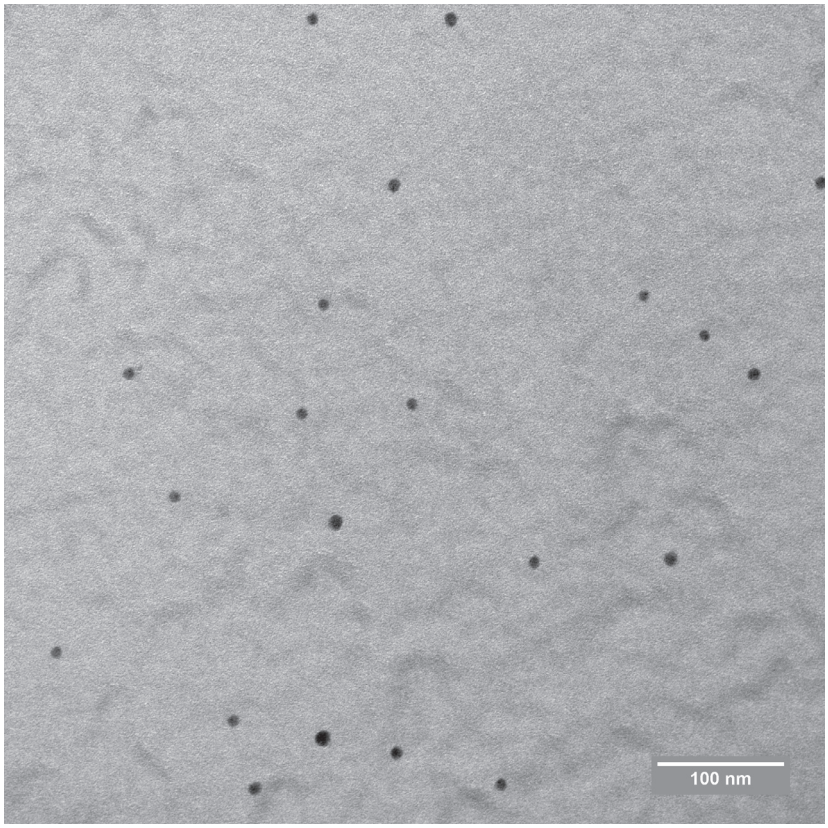

Figure 3.3.: TEM image of Ag clusters deposited with a quadrupole voltage of ±250 V on a carbon coated TEM grid. The particles appear as dark dots on the amorphous carbon film. The cluster density is about 2×10^9 clusters per cm^2.

One challenge during the deposition is to reduce the gas pressure from about 30 mbar in the cathode to UHV conditions at the sample. Several pumping stages consisting of turbo molecular pumps and a newly installed cryopump (see Fig. 3.1) are used to achieve ultra clean deposition conditions. Figure 3.5 shows the effectiveness of the cryopump: before the cryopump was installed the 7×7 reconstruction of the substrate was not directly visible in STM images after cluster deposition (Fig. 3.5a). Only with the help of a 2D autocorrelation [2] the three-fold symmetry of the 7×7 reconstruction can be revealed (inset in Fig. 3.5a).

[2]The 2D autocorrelation is a mathematical tool for finding repeating patterns or periodic signals that have

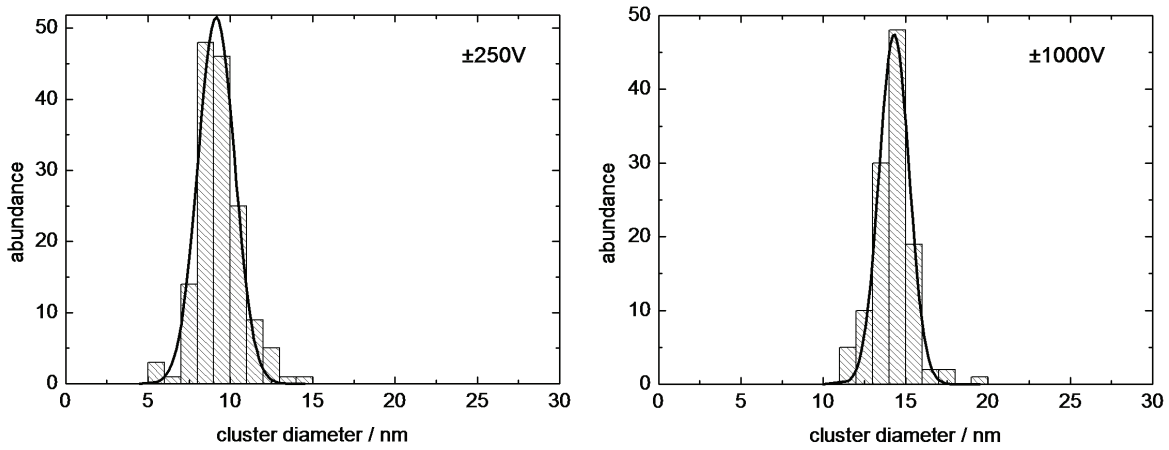

Figure 3.4.: Size distribution of the cluster diameter for a ±250 V (left) and ±1000 V (right) deposition. The black line shows a fitted Gauss distribution, from which the mean particle diameter can be estimated.

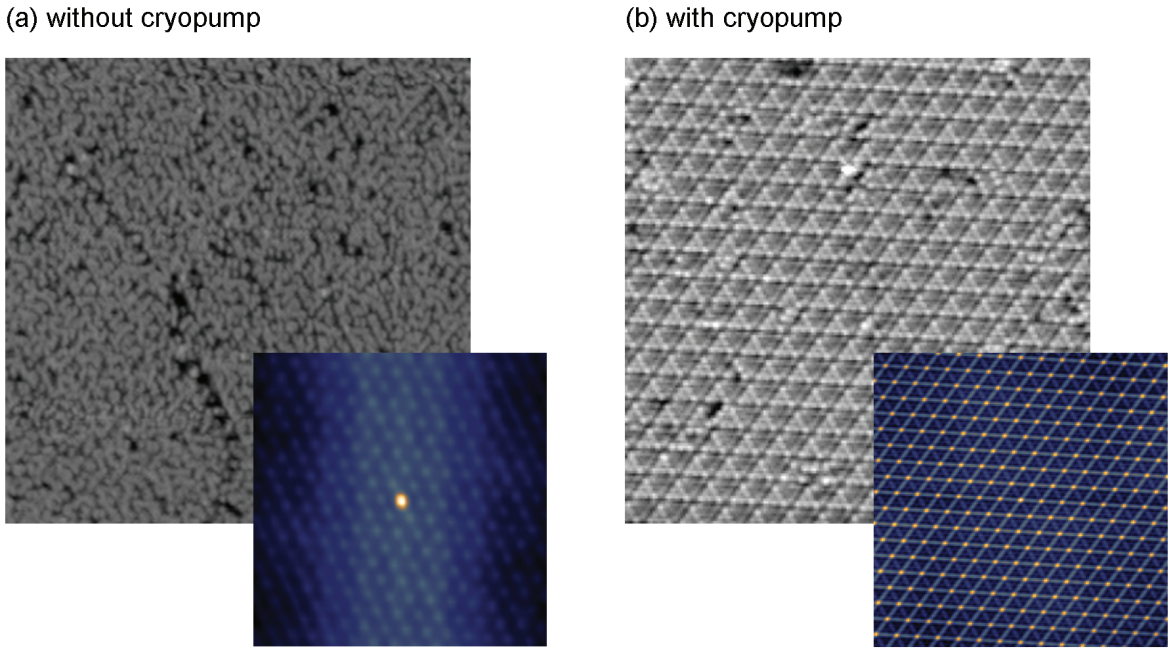

Figure 3.5.: The effect of the cryopump on the cleanness of the Si(111)7x7 surface after the deposition process: (a) before cryopump was installed (95 nm × 95 nm) and (b) with working cryopump (40 nm × 40 nm). Insets: the 2D autocorrelation of the respective topographies.

After installation of the cryopump, the 7×7 reconstruction is still clearly visible after the cluster deposition (Fig. 3.5b). Consequently, the 2D autocorrelation shows a perfect periodicity as well. So finally the setup allows the deposition of size-selected clusters while

been buried under noise. Applied to STM images it can help revealing the periodic structure of a surface reconstruction.

the atomic surface structure is preserved, even on reactive substrates like semiconductors. A highly transparent grid (flux measurement in Fig. 3.1) allows the measurement of cluster currents in the pico-ampere range providing information about the actual cluster beam flux. By integrating over the deposition time a total deposited charge, that is proportional to the amount of the deposited clusters, can be calculated. By comparing the deposited charge with the cluster density from TEM investigations, it is possible to calibrate the flux measurement to the amount of deposited clusters.

3.3. Surface analysis system

The surface analysis system is the main apparatus where most of the experiments are carried out. The main feature is the commercial Omicron LT-STM (low temperature scanning tunneling microscope) [128] which is operated in ultrahigh vacuum (UHV). During the measurement the sample is cooled down to liquid nitrogen temperature (78 K)[1]. A schematic overview of the setup can be seen in Fig. 3.6. Figure 3.7 shows a photographic view of the whole setup.

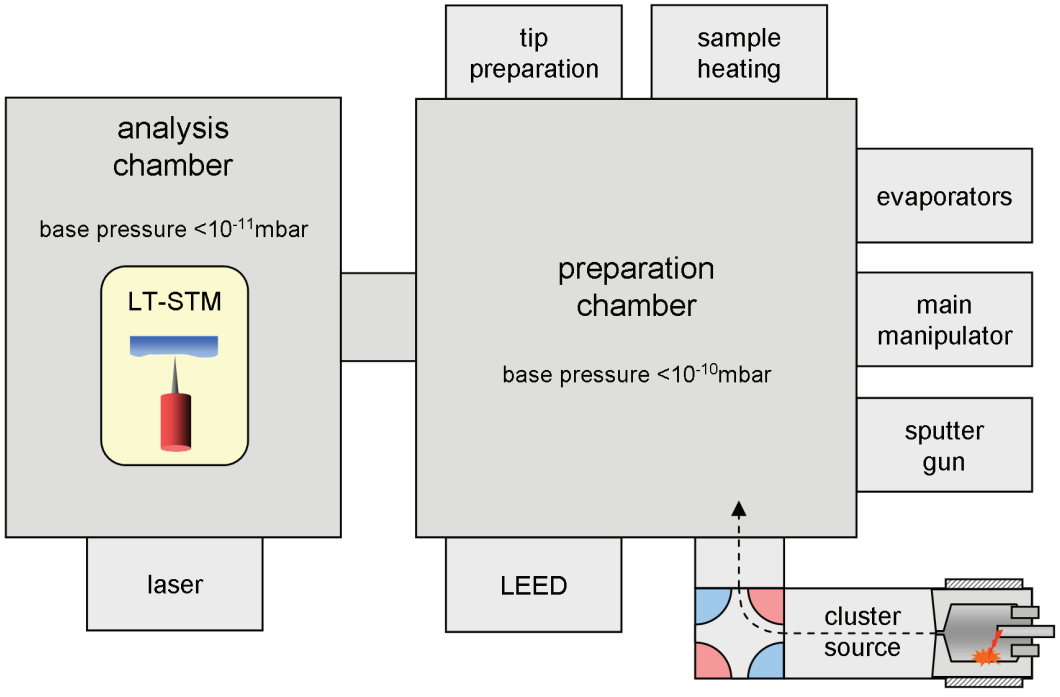

Figure 3.6.: Schematic overview of the experimental setup: the preparation chamber is equipped with standard surface science tools for sample- and tip preparation. For measurements the samples are transferred into the analysis chamber containing the LT-STM.

[1]The LT-STM can also be operated with liquid helium resulting in a sample temperature of about 5 K.

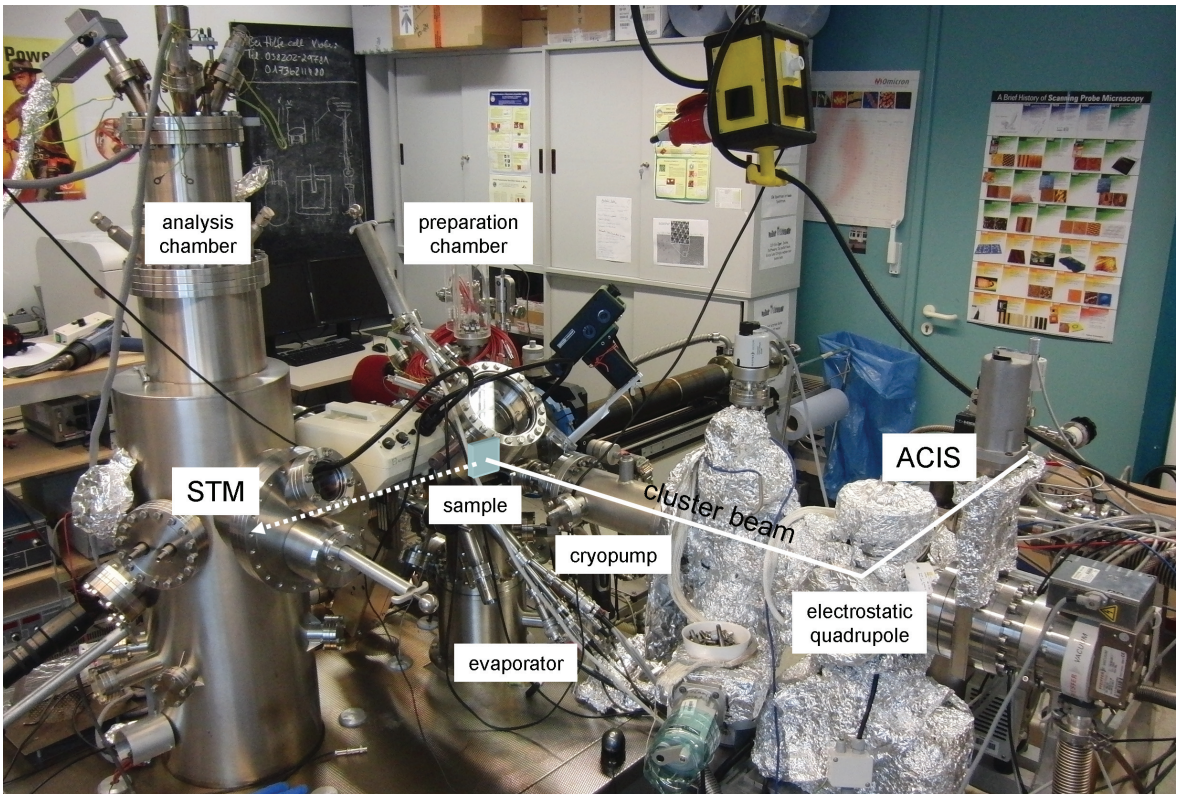

Figure 3.7.: Photo of the experimental setup including the cluster source, the cryopump, the preparation chamber and the analysis chamber. For measurements the sample is transferred into the STM.

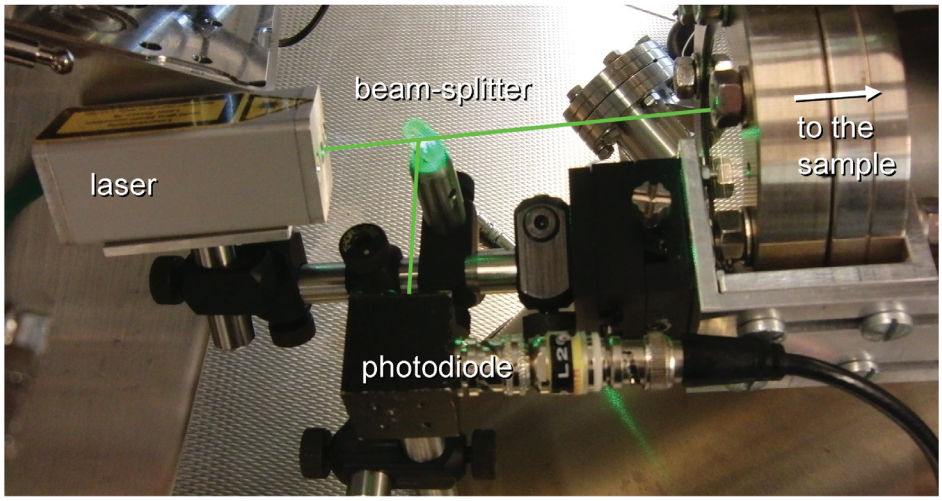

Figure 3.8.: Photo of the SPV setup externally mounted to the analysis chamber including the laser, a beam-splitter and the photodiode.

The preparation chamber (with is normally operated at a base pressure of < 10^{-10} mbar) is equipped with common surface science tools. It contains several possibilities for sample heating (electron-beam heating, direct-current heating and a resistive heater), a sputter gun, several evaporators (used e.g. for Au evaporation during the preparation of 5×2, cf. section 3.1), a LEED system, a direct connection to the cluster source that was described in section 3.2, and tools for UHV STM tip preparation. The sample can be inserted into the main manipulator to gain access to the different positions and directions within the chamber. It also allows transferring the sample into the analysis chamber where the LT-STM is located. During the measurements, the base pressure of the analysis chamber is < 10^{-11} mbar, which allows investigating clean surfaces over a long time. A small diode-laser with a wavelength of 523 nm is mounted outside the chamber (Fig. 3.8) to allow illumination of the sample through glass flanges. This is needed for the SPV measurements described in section 3.5.
The LT-STM has been optimized for electronic and acoustic low-noise operation, allowing low-noise topographic and spectroscopic measurements. Even at large scan areas and high spatial resolution, the STM operates thermally stable, although such large scans may take several hours per image to complete. As a result, the topographic images contain very low thermal drift. For spectroscopic modes the low electronic noise allows fast recording of $I(V)$ spectra. This is especially useful when performing spatially resolved spectroscopic maps that can easily consist e.g. of $50 \times 50 = 2500$ spectra. When using a lock-in amplifier for obtaining dI/dV spectra the modulation frequency can be set to several kHz. So even complete dI/dV maps with a high spatial resolution are possible in a reasonable time.

3.4. Tip preparation

The STM tips used in the experiments are made of 0.1 mm thick tungsten wire and are electrochemically etched in a 0.5 molar NaOH solution. The etching process is controlled by a special power supply that automatically cuts off power when a threshold slope in the current is reached. This ensures the tip to be relatively sharp upon etching. Afterwards, the tips are mounted to a standard OMICRON tip holder. In UHV the tips are prepared by heating cycles and self-sputtering with Ar^+ ions [129]. The heating is sketched in Fig. 3.9a. A ringlike filament is positioned near the tip, so that the front part of the tip is located within the ring. A high voltage HV is applied between them, yielding electrons emitted from the filament and accelerated to the tip front. The electron bombardment removes surface oxides and causes local melting by atomic diffusion, resulting in a rounder tip. In the following self-sputtering cycle (Fig. 3.9b) the tip is bombarded by the Ar^+ ions leading to a defined modification of the tip apex. This process is also known as “Schiller decapitation” as it was first described by Schiller *et al.* [130]. They found that the sharpening of tungsten tips shows a surprising effect when sputtering the tip with neon ions. The ions produce a neck in the foremost part of the tip which then becomes thinner until it breaks off due to induced stress.

Although this decapitation process limits the attainable sharpness of the tip to a radius of about 4 nm, the process is successfully used to create sharp tips in a reproducible manner.

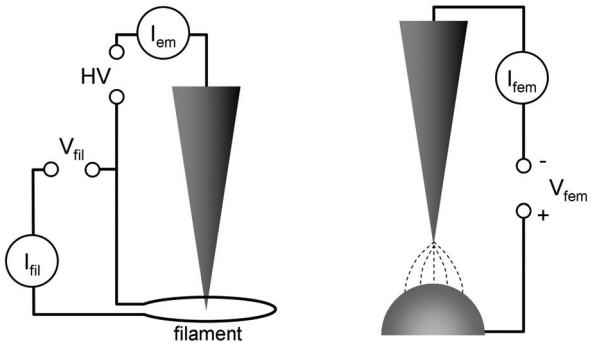

Figure 3.9.: Setup for the UHV tip preparation methods for (a) tip annealing with electron bombardment and (b) self-sputtering and field emission.

During self-sputtering the sharpness of the tip is monitored with the help of field emission [99]. The setup is the same as during the self-sputtering (Fig. 3.9b). When a voltage V_{fem} is applied between the tip and the electrode, an electron emission current I_{fem} can be measured that is given by the relation

$$I_{fem} \propto \left(\frac{V_{fem}}{r}\right)^2 \exp\left\{-6.8 \times 10^9 \phi^{3/2} \frac{\xi k r}{V_{fem}}\right\} \tag{3.4}$$

where ϕ is the work function of the tip, ξ is a correction factor [131] and r is the radius of the tip apex [132]. If the current I_{fem} is set to a fixed value, e.g. 50 nA in our case, the tip radius r is proportional to the voltage V_{fem}. So a lower voltage indicates a sharper tip apex. A typical field emission voltage that results from a good tip is in the range of $V_{fem} =$ 200...300 V. With this voltage one can generally estimate the size of the tip with the help of equation 3.4. Nevertheless this is quite difficult as the involved constants are generally not exactly known. Ernst *et al.* [132] showed a relation between the voltage and tip radius r that is the result from using an average work function for Tungsten of 4.5 eV and a comparison with SEM data:

$$r \approx \frac{2}{3}(\pm\frac{1}{6})V_{fem} \tag{3.5}$$

for r in $\mathring{A}$ and V_{fem} in V. From this equation the tip size can be estimated to $r =$ 13...20 nm. This is of course only a rough approximation. The large error in the equation of 25% results from the finite resolution of their used SEM.
When the preparation cycles are complete and the tip shows a sufficient sharpness, it is transferred into the STM.

3.5. STM supported SPV measurement

When the sample is illuminated with a laser, a surface photovoltage (SPV) occurs (cf. section 2.2). This SPV can be directly accessed by STM with several different approaches (cf. section 2.6.4). In this work simple $I(V)$ spectroscopy is used as the SPV directly corresponds to the shift of the zero-crossing of an $I(V)$ curve under illumination. The basic experimental setup for the STM supported SPV measurements is shown in Fig. 3.10.

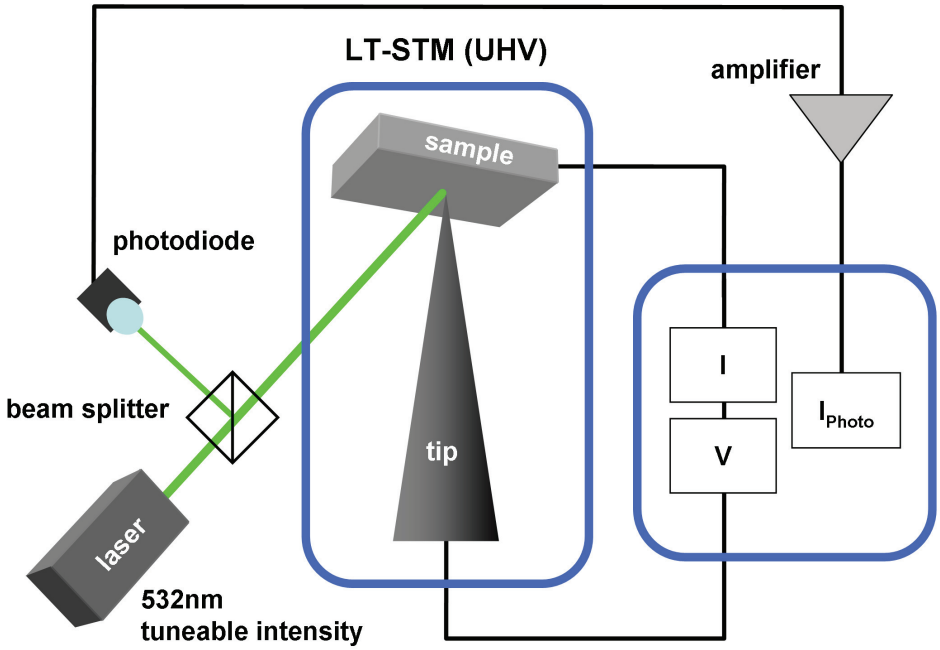

Figure 3.10.: Setup of the direct SPV measurements with the STM. The laser is pointed at the sample while $I(V)$ spectroscopy is performed with the STM, from which the surface photovoltage can be directly extracted.

A green laser ($\lambda = 532$ nm, $P = 0...20$ mW) is used to illuminate the sample from outside the chamber (cf. Fig. 3.8) with constant photon flux with a spot diameter of about 1...2 mm. A part of the beam is redirected to a photodiode, that is also located outside the chamber, for monitoring the laser intensity via the photocurrent I_{photo}. A highly-sensitive amplifier (FEMTO) is used for amplification of the photodiode signal. The wavelength ($\lambda = 532$ nm, $E = 2.33$ eV) has been chosen to achieve a compromise between available laser power and absorption efficiency [35]. During an experiment current-voltage curves $I(V)$ are recorded in constant-height mode with the STM and the laser intensity is logged using the photocurrent from the photodiode. The $I(V)$ spectroscopy is performed as grid spectroscopy. In that case several spectra are taken on different positions that are given by a grid of positions. When using small distances between two neighbored spectra, it is possible to achieve spatially resolved SPV maps. Afterwards single spectra are averaged over the region of interest for increasing the signal-to-noise ratio. Using grid spectroscopy

has two advantages in our case: first, it can be automatically performed without permanent interference by the experimentalist (as it is needed when using single point spectroscopy) and second, it is easier to evaluate during the following analysis.

3.5.1. Thermal effects

When a laser is used during a STM measurement to illuminate the tip-sample system, thermal effects have to be taken into account [42]. One main effect is the heating of the tip and sample due to the incoming light, resulting in a thermal expansion of both. This affects the width of the tunneling gap leading to a different tunneling condition and in a distorted tunneling current. These effects are important when the light is modulated, like e.g. in the chopped-light SPV methods. However, also ordinary power fluctuations of the laser have to be taken into account. In this work the tip and sample were constantly illuminated over a long time. This ensures a good thermal stability and a non-distorted measurement, as the STM feedback loop simply moves to a new equilibrium tip height where the setpoint for the tunneling current applies. Therefore the problem of thermal expansion is minimized. However, after adjusting the laser power the system has to adapt which can last up to one minute or more. In this time the thermal drift dominates the STM images resulting in a deformed topography. In the measurements it has always been taken care, that the system has enough time to thermally equilibrate after the laser intensity is changed.
If a temperature difference exists between the tip and the sample, a thermovoltage builds up across the tunneling junction [133, 134]. The temperature difference causes different electron distributions in the electronic states of the tip and the sample causing a current of thermally excited electrons. This leads to an accumulation of electrons in one electrode and thus to a potential difference reaching a value such that the total current vanishes under open-circuit conditions. This potential difference is called thermovoltage. Park *et al.* [135] have shown in a theoretical study that the induced thermovoltage due to surface generation of heat for a laser intensity of 1.2 MW/cm^2 is about 10 mV. As the laser used in this work has less intensity, the expected thermovoltage should be much less and thus can be neglected.

3.6. GISAXS on deposited clusters

The GISAXS experiments are carried out at the Advance Photo Source (APS) of the Argonne National Laboratory (ANL) (Chicago, Illinois, USA) in a collaboration with the group of S. Vajda (Materials Sciences Division and Center for Nanoscale Materials, ANL) [112]. The intention is to use the sensitivity of GISAXS during a catalytic reaction, i.e. the partial oxidation of propylene in this case, for monitoring the shape change of silver nanoparticles [24, 25, 136]. The here shown experiments are performed at the 12-ID

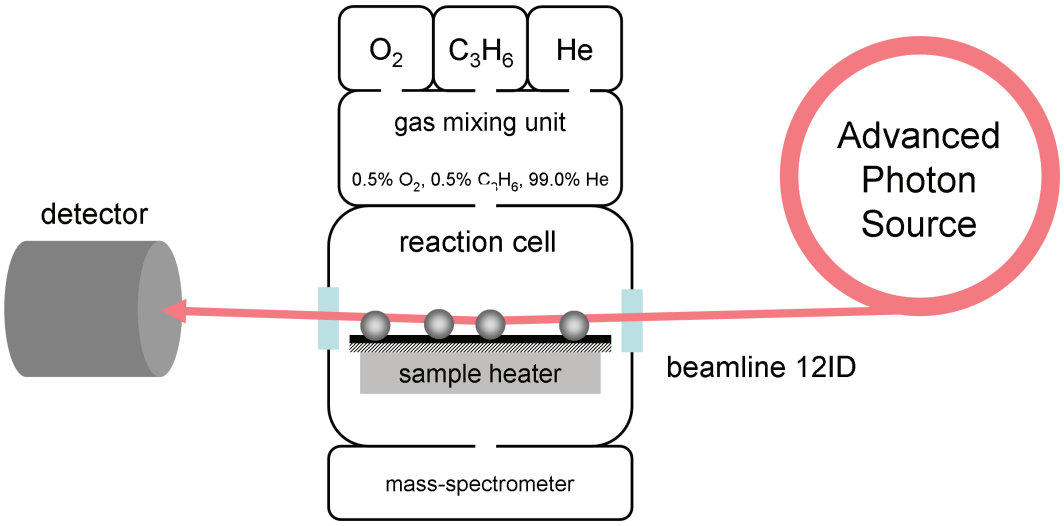

Figure 3.11.: Schematic view of the GISAXS experiment containing reaction cell, gas mixing unit, mass-spectrometer and detector. See text for more details.

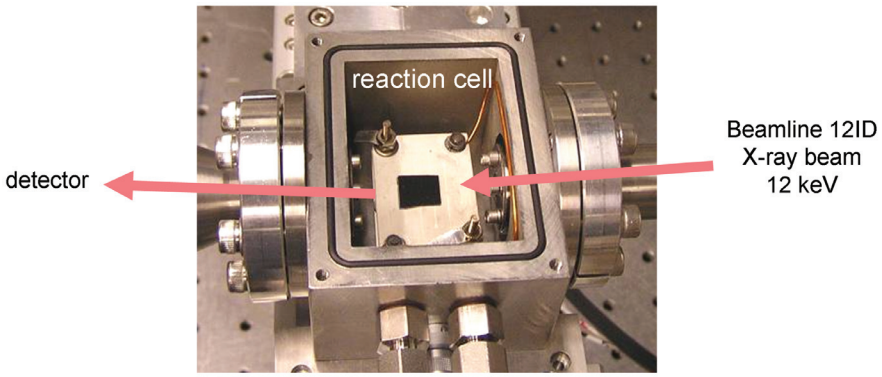

Figure 3.12.: View of the reaction cell containing a sample. The beam enters the cell through a windows on the right, interacts with the sample and exits the cell on the left in the direction of the detector.

Figure 3.13.: Experiment setup at the 12-ID beamline at the Advanced Photon Source (Argonne National Laboratory). The beam enters from the right into the reaction cell, where the interaction with sample takes place. The detector on the left is used to record the scattering image.

beamline of the APS sub-division Basic Energy Sciences Synchrotron Radiation Center (BESSRC). The beamline is operated at 12.0 keV photon energy.
The Ag nanoparticles used in this experiment are produced in our lab in Rostock with the ACIS and deposited on a 3 ML thick Al_2O_3 film that was produced before at the ANL by atomic layer deposition (ALD) [137] onto a naturally oxidized silicon wafer [111, 138]. ALD is a thin film growth technique that uses alternating cycles of saturating reactions between gaseous precursor molecules and the substrate surface for the deposition of films. For the here used samples six ALD cycles are used resulting in alumina films of approximately 3 ML thickness.
The schematic view of the GISAXS experiment is depicted in Fig. 3.11. The X-ray beam, provided by the APS synchrotron, enters the reaction cell which is a custom design developed by the Vajda and Winans groups (Fig. 3.12). In the reaction cell the sample is located on a ceramic resistive heater that allows heating of the sample up to temperatures of 600°C. The gases needed for the reaction are mixed in an external remotely controlled gas-mixing unit consisting of several mass flow controllers (Brooks), which is directly connected with the reaction cell. The cell was operated in a continuous flow mode at 133 kPa pressure and 30 sccm gas flow. The resulting reaction products are analyzed with a differentially pumped mass-spectrometer (Pfeiffer). To ensure thermal equilibrium between the heater and the sample during the process of a automated temperature ramp, a low heating rate < 1.5°C/min is used.
Figure 3.13 shows an overview of the experiment. The X-ray beam is entering from the right. In the reaction cell, the beam is scattered off the sample surface near the critical angle, which is the angle of total reflection, of the substrate ($\alpha = 0.18°$). A 2D CCD detector (Marresearch) with a resolution of 1024 pixel $\times$ 1024 pixel is used for the detection and imaging of the scattered X-rays. The GISAXS data is collected as a function of the sample temperature and time for the further analysis.

4. Results and analysis

After introducing the methods and concepts in the first chapter and explaining the experimental setups in the second chapter, the results from the experiments will be presented, analyzed, and discussed in the following. In the first two sections properties of deposited metal particles on semiconductor surfaces are investigated. Ag clusters are deposited on the Si(111)7×7 surface and their diffusion properties upon landing are investigated regarding a possible diffusion at the surface. Simulated results are compared to the experimental data to get insight into the problem. In the next part the laser-induced surface photovoltage is used to gain access to the band topology of the "metal cluster on semiconductor" system. Patches of the quasi 1D chain-structure Si(111)5×2 are used as a model system for a systematical study. A model of the band topology is developed for visualizing the experimental findings. In the last section deposited Ag particles are investigated as efficient catalysts using *in-situ* GISAXS. During the ongoing reaction, the observed changes of the cluster shape is investigated and discussed.

4.1. Diffusion properties of deposited clusters on Si(111)7×7

When nanoparticles are deposited from the free beam onto the sample surface under soft-landing conditions, there are two possibilities: the particles stay at their impact position or they move across the surface for a certain way due to some kind of diffusion mechanism. The behavior depends on several factors like the material of the clusters and of the substrate, the surface energy and temperature of both materials, and the kinetic energy of the clusters during the impact. Due to the quantity of the kinetic energy, on the one hand the cluster may land safely on the surface or on the other hand fragmentation of the particles may occur upon landing on the surface. The nanoparticles that are produced with the ACIS (cf. section 3.2) have a kinetic energy in the range of 10^{-3}...10^{-1} eV/atom [139]. Simulations and experiments in the literature show that the soft-landing regime applies for a kinetic energy lower than 0.1...1 eV/atom [140, 6, 141]. For the cluster deposition setup used in this work the kinetic energy can be written as a function of the applied quadrupole voltage

$$E_{kin} = (1.65 \pm 0.12) \cdot e \cdot U_{quad} \tag{4.1}$$

which is a result from simulations done by J. Passig [139]. Using the kinetic energy, which corresponds to the whole cluster, and the number of atoms per cluster, the kinetic energy per

atom can be calculated. Assuming a spherical shaped particle, the number of atoms N in the particle is given by

$$V = \frac{4\pi}{3}r^3 = N\frac{a^3}{n_{uc}} \quad \rightarrow \quad N = \frac{16\pi}{3a^3}r^3 \tag{4.2}$$

where V is the volumina of a sphere with the radius r, a is the lattice constant ($a = 0.409$ nm for bulk silver) and n_{uc} is the number of atoms per unit cell, which equals 4 in the case of a fcc structure. The cluster radius r that is used in the calculation, is taken from the experimental results in Fig. 3.2. With this it is possible to give a rough estimation on the kinetic energy per atom for clusters of different sizes which is shown in table 4.1. It can be seen that the particles have an energy of about $E_{kin} \approx 20$ meV/atom which indicates soft-landing conditions in the experiments.

U_{quad}	$E_{kin,total}$	r	N	$E_{kin,atom}$
2000 V	3300 eV	8.55 nm	153065	21 meV
1000 V	1650 eV	7.15 nm	89515	18 meV
500 V	825 eV	5.55 nm	41866	19 meV
250 V	412 eV	4.55 nm	23068	18 meV

Table 4.1.: Estimation of the kinetic energy per atom for different cluster sizes calculated with equation 4.1 and 4.2.

The 7×7 surface used for cluster deposition features domains that are separated by a network of boundaries, that will be shown later in section 4.1.2. It is known that these boundaries act as traps for the moving particles. In Fig. 4.1 a single boundary between two 7×7 domains is shown. The boundaries do not always follow a straight line. Instead, the direction can change within the threefold symmetry of the 7×7. This is seen in the middle of the picture, where the boundary shows a small kink. At this point the path of the boundary shows a difference of about two unit cells. The dislocation between the patches caused by the formation of the boundary can be visualized by using a vector, in analogy to the Burgers vector, introduced 1939 by Burgers [142], that is used to describe dislocations in crystal lattices. This vector shows the difference of one Burger circuit on the undisturbed patch (dashed green triangle) and one circuit of the same size located over the boundary (red triangle). For defining the vector the dashed green triangle is moved to fit two corners of the red triangle. This is shown by the solid green triangle. The difference of both circuits can then be expressed by a vector (blue arrow) (inset in Fig. 4.1). This vector is a characteristic feature of the boundary. The thickness of the boundary can be estimated from the image to at least the size of one unit cell which is about 2.5 nm.

For investigating the diffusion properties of the particles, a direct measurement during the deposition would be needed. With the current experiment setup this is not possible. So a different approach is used here: a statistical analysis of the distance between a cluster and the next boundary provides information whether the clusters are randomly distributed or

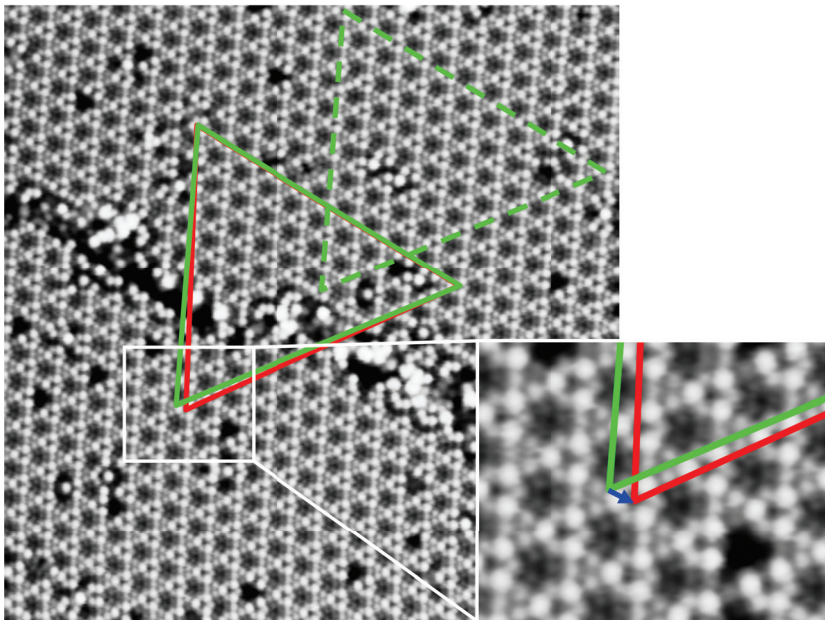

Figure 4.1.: A boundary in the 7×7 reconstruction. The offset in the reconstruction across the boundary is indicated by the colored triangles. **Inset:** Construction of the displacement vector (blue arrow) from the undisturbed triangle (green) and the dislocated triangle (red). (58 nm × 58 nm, $U_{gap} = -0.6$ V, $I_T = 50$ pA)

whether a diffusion mechanism is involved. To determine this behavior a simulation of the cluster deposition is performed in the following and then compared to experimental results. For the following analysis the raw STM images are prepared in the following way. In Fig. 4.2 a topographic image taken by STM is processed with a mean line correction and a plane leveling so that it perfectly shows the sample surface decorated with the deposited clusters, which appear as bright spots. The substrate shows different terraces appearing as different brightness levels of grey from left to the right. The terraces are separated by the step-edges. The size of the shown image is 1 μm × 1 μm. Some huge particles that do not fit the expected particle size also appear in this image. If they cannot be clearly identified as single or agglomerated clusters they are ignored in the following analysis. Since only a very few particles with an abnormal shape are ignored this does not influence the statistical analysis. Figure 4.3 shows the derivative image of Fig. 4.2. Here the objects and structures are better visible for the following processing. Here not only the particles can be clearly seen but also the boundaries are visible as small light-grey lines. Some step-edges appear as dark vertical lines. In Fig. 4.4 the boundaries (red lines) and step edges (blue lines) are extracted from Fig. 4.3. This is done manually by marking the boundaries and step edges with a standard graphics software. The red-blue color-coding is used later in the algorithm-based analysis and simulation. At some locations the exact shape of a boundary is not visible in the original data as it is covered by a cluster. Here the boundaries are manually interpolated by fitting a straight line through the particle. The particles are neglected in this image as only the

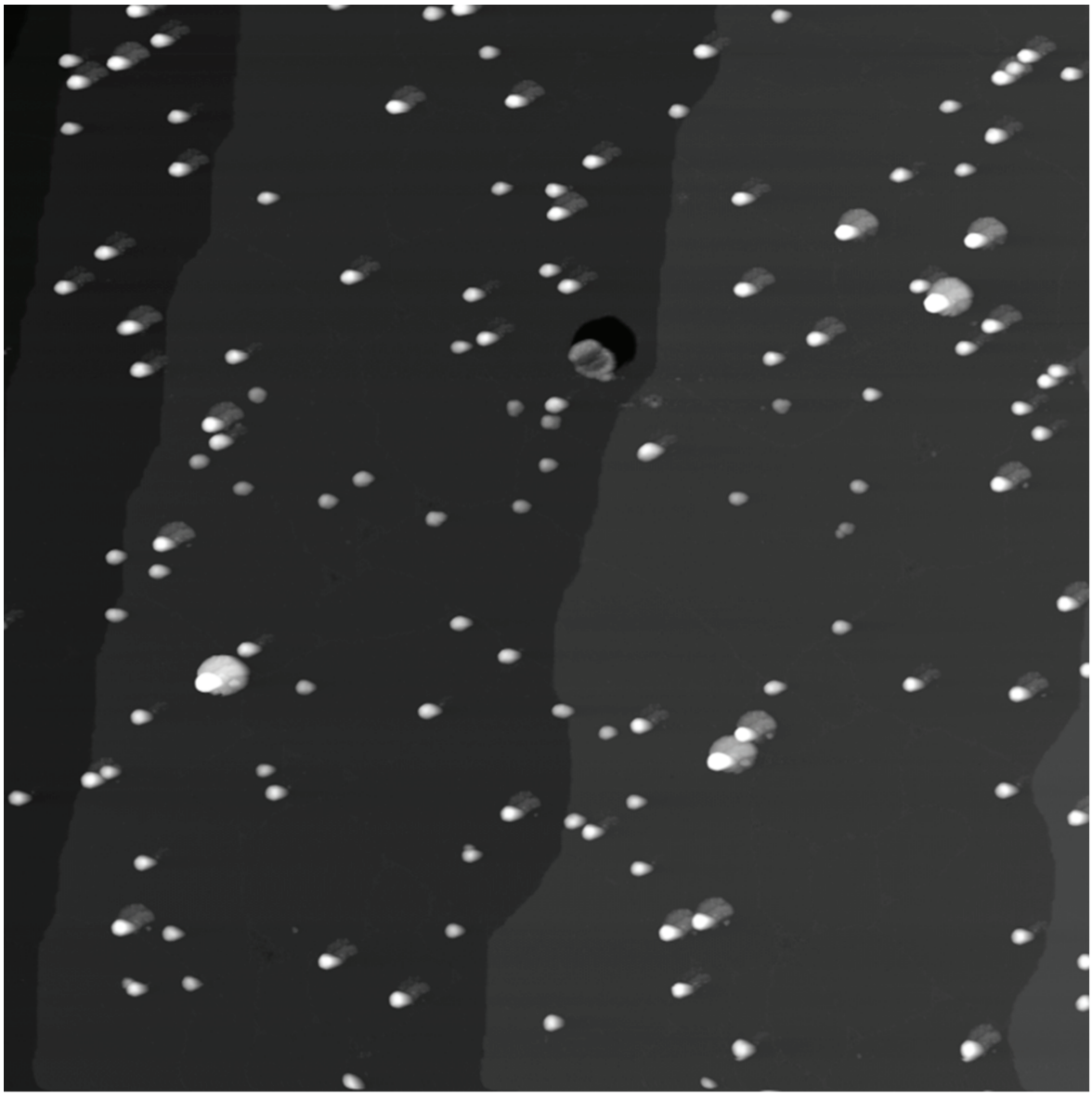

Figure 4.2.: Topographic image of deposited clusters on Si(111)7×7 (1 μm × 1 μm). The clusters appear as bright spots. The substrate exhibits several terraces that appear as steps in the background color.

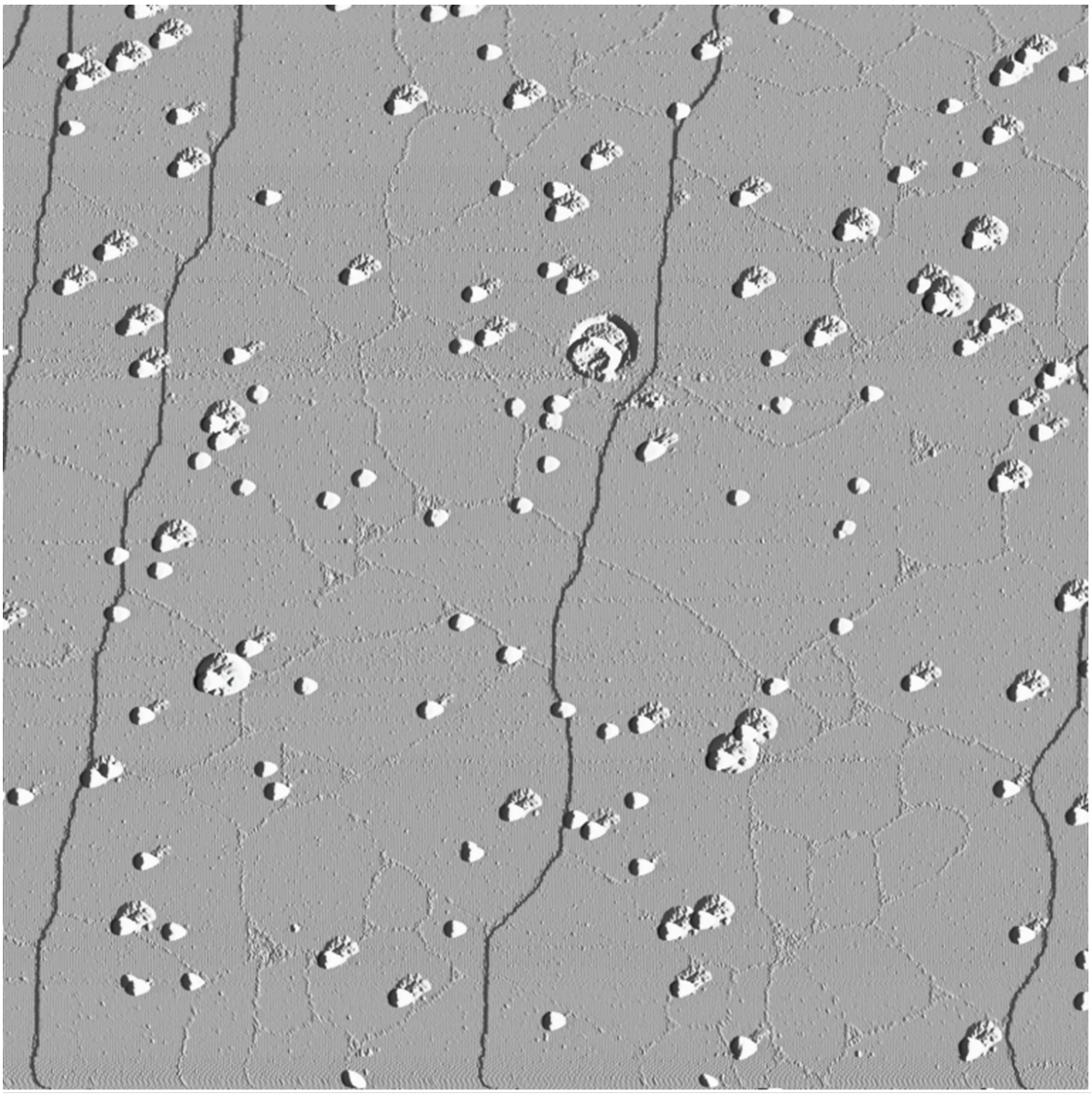

Figure 4.3.: Numerically differentiated image of Fig. 4.2. Clusters appear as black-white spots, boundaries as light-grey lines and step-edges as vertical dark lines.

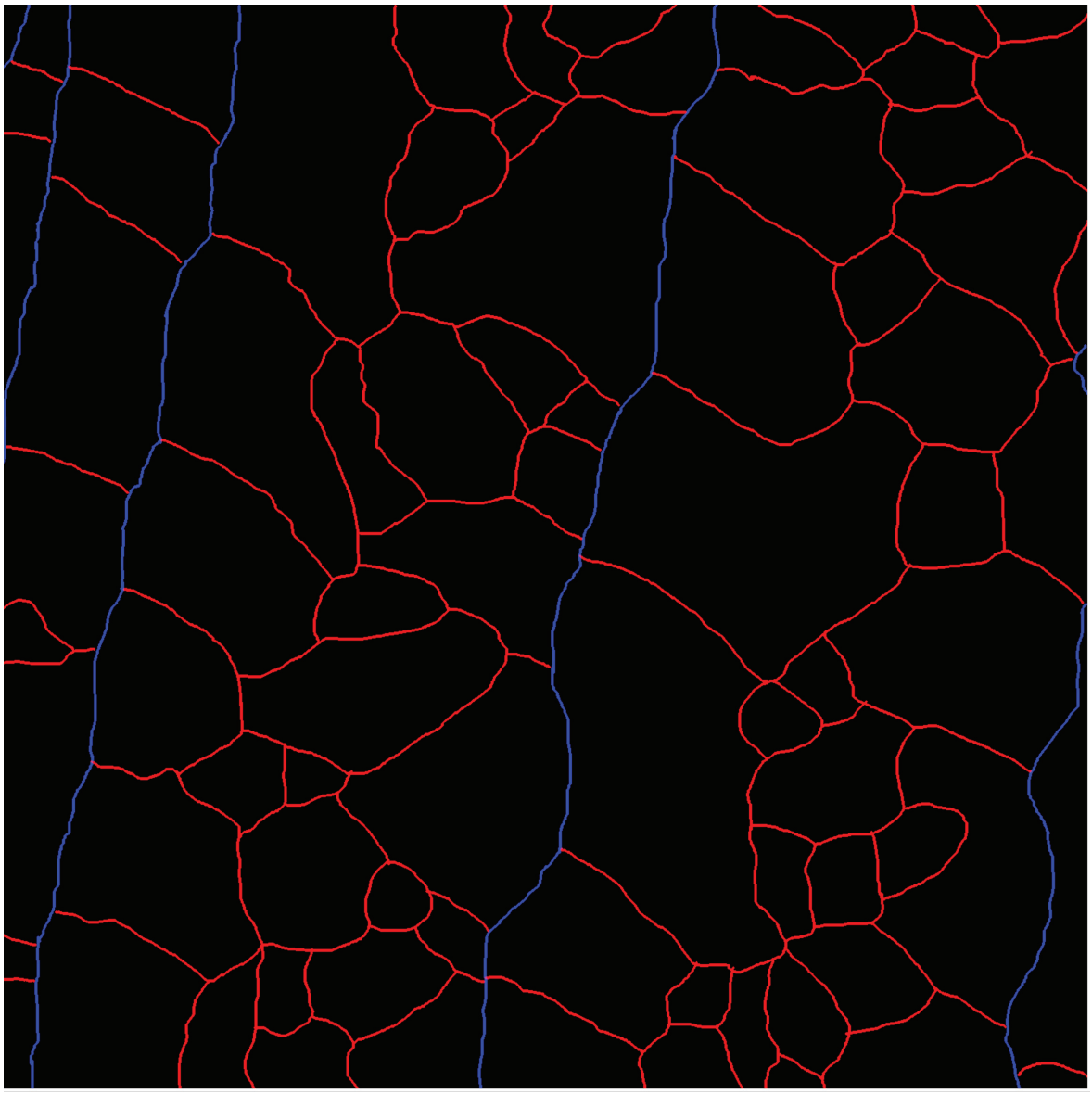

Figure 4.4.: Mask image of boundaries (red) and step edges (blue) generated from Fig. 4.3. The clusters are ignored here.

boundaries are needed for the simulation. The extracted boundary network is now used in different simulations that will help to investigate the behavior of the clusters upon landing on the sample surface.

4.1.1. Simulation

The impact position of the clusters is now simulated using the boundary mask from Fig. 4.4. The simulation is performed in two ways: (1) the cluster have a fixed random position after deposition (Fig. 4.5a) and (2) the cluster have a random position and a finite probability for diffusion after deposition (Fig. 4.5b). After the cluster are produced in the ACIS they have a certain kinetic energy during their flight through the cluster apparatus. As the particles are mass-selected by the electrostatic quadrupole, they all have the same kinetic energy within a certain energy distribution. So it can be assumed that the particles deposited on the sample have the same probability for a possible diffusion. Therefore all the particles can be handled within the same simulation model.

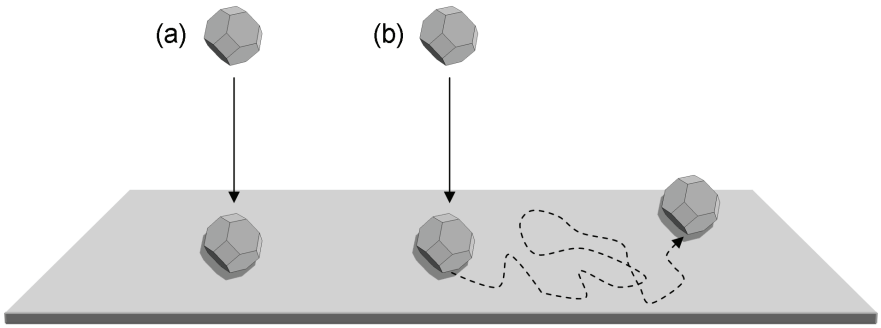

Figure 4.5.: The two simulated ways of the cluster behavior upon landing: (a) the clusters have a fixed random position and (b) the cluster move over the surface according to a simple diffusion model.

In the case of a cluster diffusion on the surface, the question is what mechanism is driving it. Unfortunately there is still little understanding of the diffusion of large deposited nanoparticles. Jensen *et al.* [12] assumed that they might keep their metastable configuration compared to grown clusters that would accommodate easily to the substrate geometry. At least one particle facet is in contact with the surface. One possible mechanism for diffusion is that all atoms on this contact facet perform a combined movement in one direction on the surface lattice resulting in a movement of the whole cluster. But here a large energy would be needed as every atom on the facet is involved in the movement at the same time. Another model was proposed by Kellogg *et al.* [143, 144] by assuming a mechanism in which the peripherical atoms, which are the surface atoms of the particle, diffuse across the cluster surface resulting in a net displacement of the whole particle. Here only small energies would be needed as only the energy barrier for one single atoms has to be overcome at one

time.
However it is not the aim of this work to investigate the exact diffusion mechanism. And because it is not easy to distinguish, the simplest diffusion model is assumed in this simulation, which is in principle a random walk model. With a Monte Carlo method the placement of the clusters is simulated by generating random numbers within the dimensions of the image for the x and y coordinates. The simulations are performed for different diffusion mean diffusion paths of the particles. The detailed procedure of the simulation is described in appendix A.2. When the cluster reaches a boundary or a step edge, the movement is halted as it is well known that defects and step edges pin the clusters due to the increased surface bonding [145, 10].

In Fig. 4.6 the results from different simulations for 500000 particles, that are placed on the boundary mask of Fig. 4.4, are shown [1]. It illustrates the abundances of the distances from a particle to the next boundary. The histograms represent the results for the random cluster placement without diffusion (black line) and the diffusion model (colored lines) for different mean diffusion paths (MDP) from 1 nm up to 300 nm. Some of the simulations show a distribution with a high peak around zero, which especially occurs at higher values of the MDP. In contrast the simulation without diffusion features a pronounced dip at 0nm which is quite surprising. This is also present at the 3 nm simulation. The dip is an artifact of the pixel-based position raster and characteristics of the boundary mask, which is not a problem in the further analysis, because the same procedure is used for the simulated and the experimental data. So the algorithm would produce the same artifact in both cases. Thus a direct comparison of the simulation and the experiment is possible.
For a better interpretation of the histograms, the differences of the simulations with diffusion and the random simulation are plotted in Fig. 4.7. From each simulation the random histogram (black line) is subtracted, resulting in difference graphs that feature a peak around 0 nm and a dip starting at 2 nm. At higher MDPs the dip gets even more pronounced. The negative regions of a dip can interpreted in such a way that during the simulated diffusion particles located at these distances move away into regions of smaller distance and positive values. The particles that move towards a boundary and get pinned there result in the high peak around zero.

To verify the significance of the simulated data another topographic image of a different location on the same sample is converted to a boundary mask (Fig. 4.8a). This image is not used for determining the cluster positions because the positions could not be clearly determined due to huge tip artifacts. So here only the extracted boundaries are used. Comparing to Fig. 4.4 it shows a different pattern of boundaries and step edges. The result from the 500000 particle simulation is shown in Fig. 4.8b for simple random deposition (black line) and with the additional diffusion model with 30 nm MDP (green line). In comparison with the results obtained from the simulation in Fig. 4.6 (red line) it shows

[1] For a better clarity only selected simulations shown in the figure. In the following analysis all performed simulations will be taken into account.

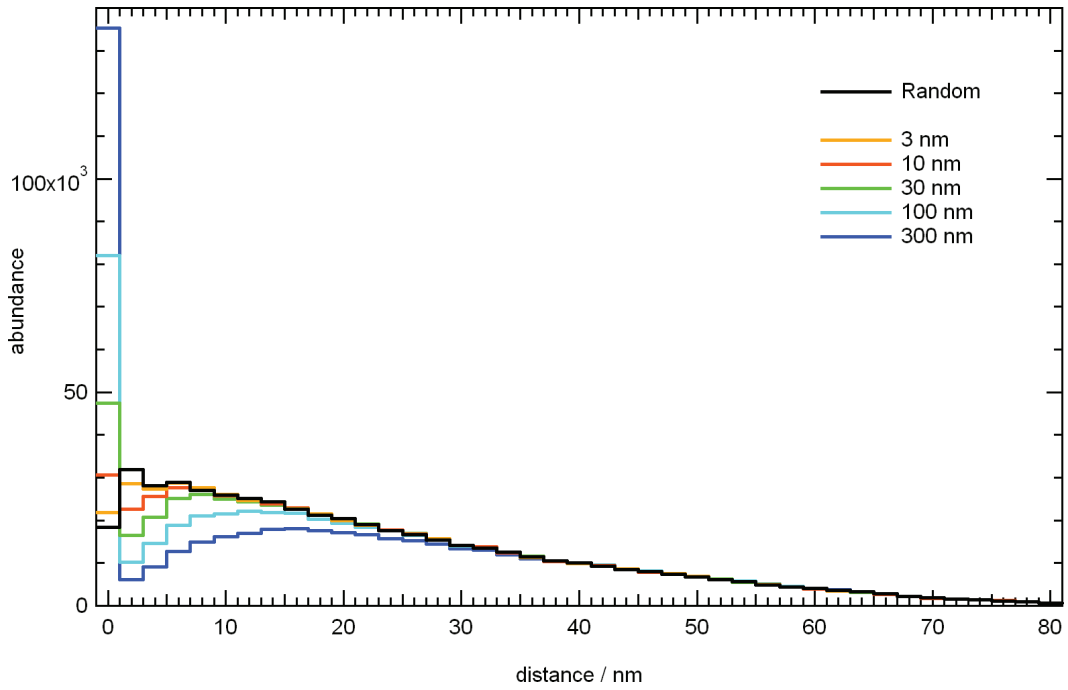

Figure 4.6.: Histograms of the distance to the next boundary for 500000 simulated particles that are placed on the boundary mask of Fig. 4.4: the random cluster placement (black line) and simple diffusion model (colored lines) for different diffusion step probabilities. Note that only selected simulations are shown for clarity.

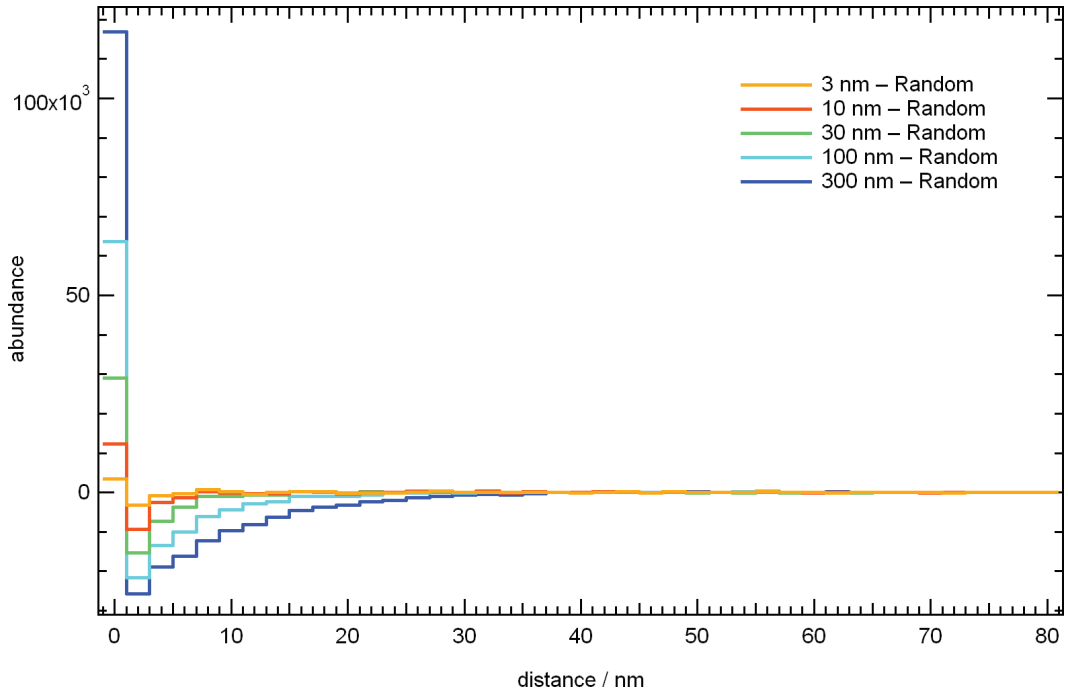

Figure 4.7.: From every diffusion simulation the random simulation (black curve in Fig. 4.6) is subtracted. During the diffusion particles have moved from regions of negative values to positive values.

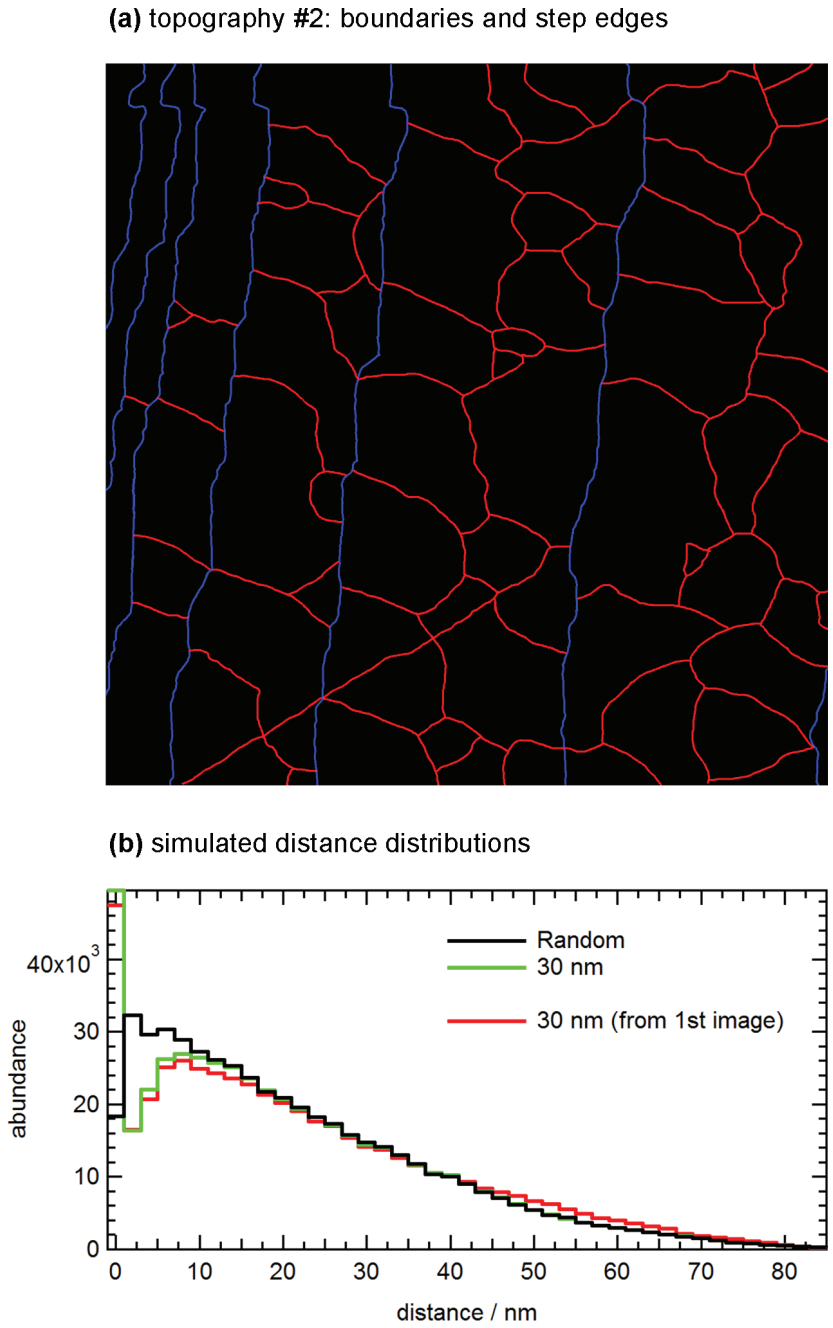

Figure 4.8.: Simulated deposition of 500000 particles with a random cluster placement (black line) and the 30nm diffusion model (green line) for a different location of the same sample. The result is comparable to the corresponding result from the first mask in Fig. 4.6 (red line).

similar characteristics for the diffusion model. The maximum cluster-boundary distance can be estimated to about 80 nm which is in accordance to the first simulation. These results show that the simulations give a relevant estimation as they are independent of the exact shape and arrangement of the boundary network and the location on the sample. This is of

course only valid if the considered section of the imaged sample is big enough and contains many different patches which is the case. Now having the results from the simulations, a comparison to the experimental data taken directly from STM images is possible.

4.1.2. Experiment

The results from the simulations are now compared to the data obtained from the STM experiment. In a first step the plain, clean surface is imaged before the deposition of the nanoparticles. This ensures that the observed amount and characteristics of the boundary network is not induced by the deposition process. Figure 4.9 shows an area of 280 nm × 280 nm of such a 7×7 surface where the characteristic structure of a boundary network can be seen.

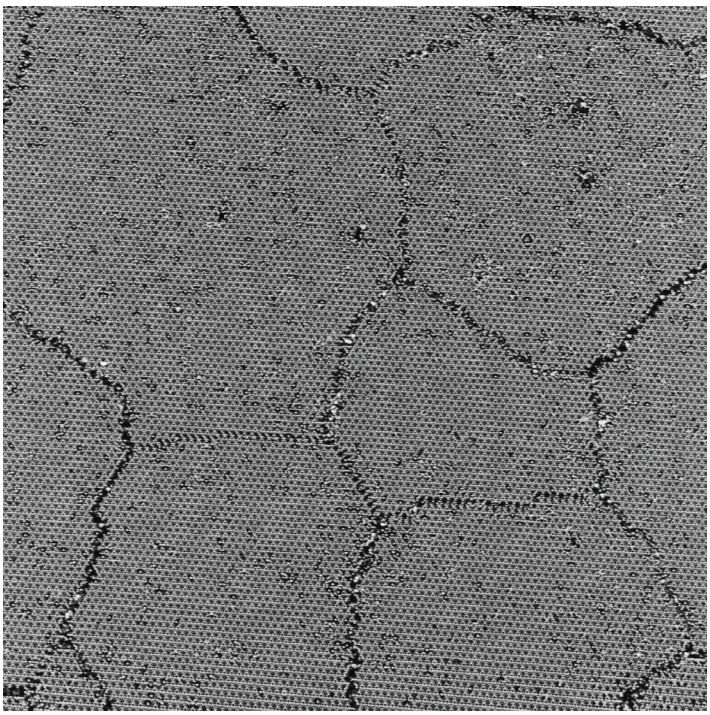

Figure 4.9.: Overview of a characteristic boundary network structure of the Si(111)7×7 surface. Within the patches small defects can be seen as darker spots. The periodic structure of the 7×7 reconstruction is clearly visible within the patches. (280 nm × 280 nm, $U_{gap} = -0.8$ V, $I_T = 15$ pA)

The boundaries appear as dark lines. Although small defects are visible as dark protrusions within the domains the periodic 7×7 reconstruction is clearly visible. This structure is representative for this sample and can be found at all investigated locations. As a first result the clusters do not induce the formation of the typical boundary structures due to their impact on the surface. This is in accordance with the theory of the origin of the boundaries described in section 2.4. But one has to be aware that the here shown boundary structure is typical for this

particular sample as the structure depends strongly on the sample preparation parameters and the sample itself. So it must be assumed that, although in different experiments every sample will be prepared in a similar way, the boundary structure will always differ in the details.
After imaging the clean surface, size selected Ag cluster are produced with the ACIS and deposited *in situ* onto the same 7×7 surface that has been investigated before. No preparation cycle is performed before the cluster deposition to ensure that there is no change in the boundary structure due to the sample preparation.

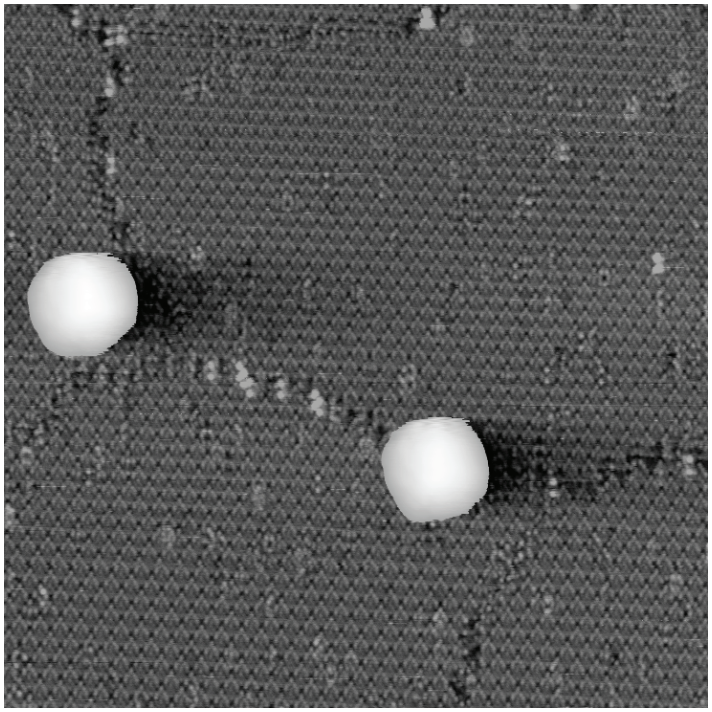

Figure 4.10.: Topographic image of Ag clusters deposited on Si(111)7×7. The cluster height is about 6 nm. The clusters are located directly on a boundary (darker lines). (100 nm × 100 nm, $U_{gap} = -1.0$ V, $I_T = 50$ pA)

STM images of the deposited particles, like Fig. 4.10, show that at least some clusters are directly located on top of a boundary. Having the results of the simulations, these topographic images are now analyzed in terms of the minimal distance between a particle and the boundaries. This will help investigating the question if the clusters are located randomly distributed over the surface or if they have preferred positions at the boundaries or step edges.
When imaging structures or objects with STM the tip convolution always broadens their imaged width. Therefore only the height of the particles can be extracted as reliable information from STM images (cf. section 2.6). The lateral size and shape of the particles cannot be determined accurately due to the convolution with the tip shape [146, 85]. However in some cases it is possible to partly deconvolute the tip shape from the cluster and obtain hints for the geometric structure of the cluster [87]. For the following analysis the imaged shape of the particles is not of real interest as the highest point, which is represented by the brightest

pixel, of an imaged particle is used for determining the position of the cluster. Even with convolution artifacts, e.g. an asymmetric tip convolution, the highest point of the imaged shape still corresponds to the highest part of the nanoparticle. This can be easily seen from geometric constructions shown e.g. by Castle *et al.* [147].
The distances between the clusters and the boundaries are analyzed by an algorithm, for a detailed description of the algorithm see appendix A.1. The algorithm searches based on a cluster position the next boundary or step edge and returns the smallest distance. The result of the distance analysis of the boundary mask in Fig. 4.2 is shown in the histogram in Fig. 4.11. From the image 125 particles are found and analyzed. The histogram shows the abundance versus the particle distance. The bin width of the histogram is set to 2 nm to fit the simulations. A small peak can be seen at 0 nm distance, meaning that 16 cluster are directly located on a boundary. Other peaks appear at higher distances while the the whole distribution shows a decrease to higher distances. As the number of analyzed particles is very low the statistical relevance can not clearly be stated for all these peaks.

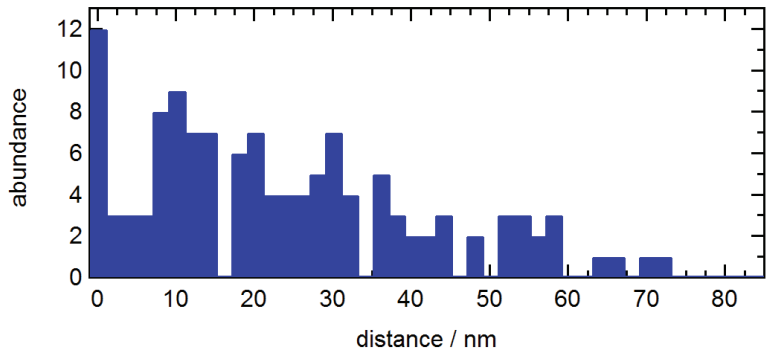

Figure 4.11.: Result from the analysis of Fig. 4.2 regarding the shortest distance between the cluster and the next boundary or step edge.

4.1.3. Discussion

The experimental results in the previous chapter show that the boundaries on the 7×7 surface are not due to the cluster deposition. As they are imaged before the deposition in the same amount and with the same characteristics they are only due to the growth of the 7×7 reconstruction during the sample preparation process and not induced by the cluster impact upon landing.
The question of the particle behavior after deposition is more complex to answer. First of all it can be said that the clusters are not all pinned at the boundaries or step edges. This can be easily seen from topographic STM images. The next question is if the arrangement of the cluster positions is completely random or if some diffusion of the particles is involved. Therefore the simulated histograms are compared to the experimental data using the chi-square test (also known as Pearson's chi-square test). This test can be used to evaluate if

a set of sample data is consistent with a given data distribution, in other words: it can be evaluated if experimental data fits to a theory. The χ^2 statistics is calculated as follows

$$\chi^2 = \sum_N \left\{ \frac{(a_i - b_i)^2}{\sigma_i^2} \right\} = \sum_N \left\{ \frac{(a_i - b_i)^2}{a_i} \right\} \tag{4.3}$$

where N equals the number of data points in one histogram, a_i is the observed value from the experiment and b_i is the predicted value from the simulation, that has been normalized to the experiment. σ_i is the variance which is related to the measurement error for a_i. In the case of a simple counting statistics it is given by $\sqrt{a_i}$. Figure 4.12 shows the calculated χ^2 values for the comparison of the experimental data (Fig. 4.11) with the simulations (Fig. 4.6). For large mean diffusion paths (> 300 nm) a large χ^2 is obtained. For small diffusion paths (< 3 nm) a χ^2 around 30 is achieved. The minimum of the calculated χ^2 value can be found at 45 nm: $\chi^2 = 13.9$. The standard deviation of the minimum value is indicated by the arrow and the dotted lines. It is calculated by using the second derivative of the χ^2 function [148]:

$$\sigma_{a_0} = \sqrt{2 \cdot \left(\frac{d^2\chi^2}{da_0^2} \right)^{-1}} \tag{4.4}$$

with a_0 being the value of the simulations length where χ^2 is minimized. The second derivative at the location a_0 is given by the curvature of a parabola that is fitted around the minimum a_0. This estimation results an error of the length a_0, resulting in a mean diffusion path of 45$\pm$18 nm.

From the χ^2 test a first insight into the problem can be obtained. In this test the null hypothesis for the simulation with a random distribution, stating that particles are randomly distributed without diffusion, is tested. The χ^2 value for the random simulation is shown in Fig. 4.12: $\chi^2 = 33.4$. In the test this value has to be compared to a test value that can be calculated from the χ^2 distribution for a given number of degrees of freedom and a selected level of significance, to verify if the null hypothesis has to be refused. The degrees of freedom, that equal the entries n in the experimental histogram 4.11 minus 1, are $df = n - 1 = 24$ in this experiment. A level of significance of 20% for the null hypothesis is assumed. Having these two values the so called "critical value" χ^2_{test} for the test can be looked up in the literature [149]: $\chi^2_{test}(0.8, 24) = 29.6$. Comparing χ^2_{test} with χ^2, the null hyptothesis has to be refused, because $33.4 > 29.6$. So as a first result it can be stated, that a random distribution without diffusion can be ruled out with a probability of 80%.

In the following, the probabilities for the remaining simulations are calculated. These values indicate the chance, that a mean diffusion path of 1, 3, 10,... nm cannot be excluded for the corresponding simulations. From the found values for χ^2 in Fig. 4.12 and the degrees of freedom df, the probability P for the different simulations can be calculated [150]

$$P(\chi, df) = \frac{\gamma\left(df/2, \chi/2\right)}{\Gamma\left(df/2\right)} \tag{4.5}$$

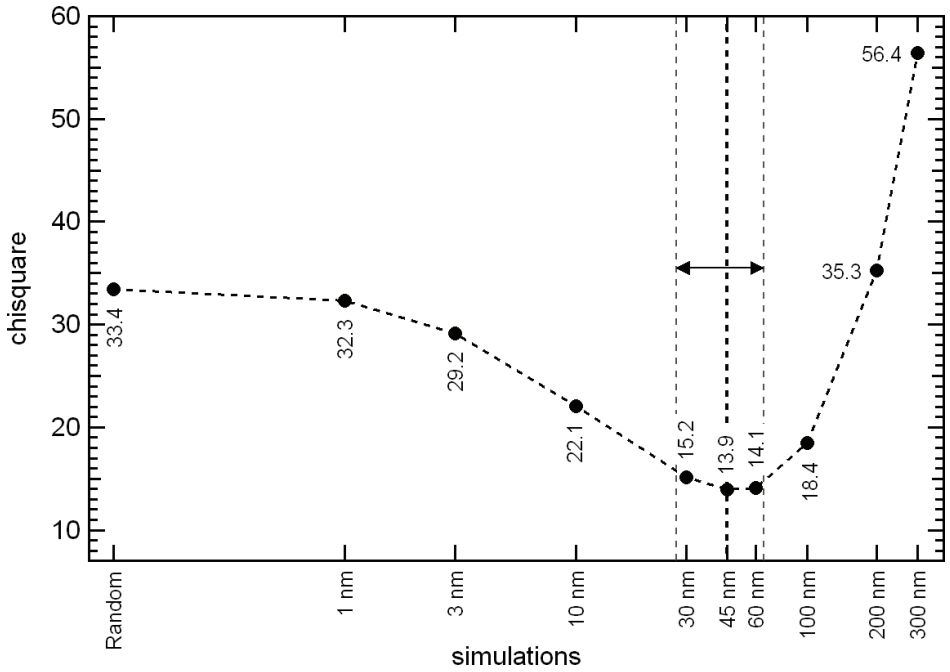

Figure 4.12.: The results from the χ^2 test for the different simulation from no diffusion to 300 nm mean diffusion path. The numbers on the markers indicate the obtained value for χ^2. Note that the simulation axis has a logarithmic scale. The calculated error of the minimal value is indicated by the arrow and the dotted lines.

where γ is the lower incomplete gamma function and Γ is the standard gamma function. The resulting probabilities are depicted in Fig. 4.13. At the lowest value for χ^2, with a chance of 95% a MDP of 45 nm cannot be ruled out. At this length the simulation has the best agreement to the experimental data. The two corresponding graphs are shown in Fig. 4.14. Here the data from the experiment is plotted together with the normalized data from the 45 nm simulation for a direct comparison. The error of the experimental data is given by $\sqrt{N}$ and indicated with the light blue bars. Taking the error bars into account the simulation fits the experiment quite well. In conclusion, it is found that the particles have a mean diffusion path of 45$\pm$18 nm, whereas this 45 nm MDP has a confidence level of 95%.

Due to the difficulty of creating good STM images of deposited nanoparticles, it was only possible to evaluate the shown experimental data in this work. When having more high-resolution and large-sized topographic images that can be analyzed, the distance distribution from the experiment will contain more particles and thus will be more definite. So for a further analysis of the diffusion behavior more data is needed from the experiment.

Having now the results of the diffusion analysis, it will be discussed how these results fit in the known diffusion properties of the particles. When clusters are landed on the surface, their kinetic energy is transferred into phonon excitation resulting in a heating of the cluster. In general, “hot” particles should be more mobile on the surface, so it is important to give a rough estimation on the temperature increase. There are two ways to estimate the temper-

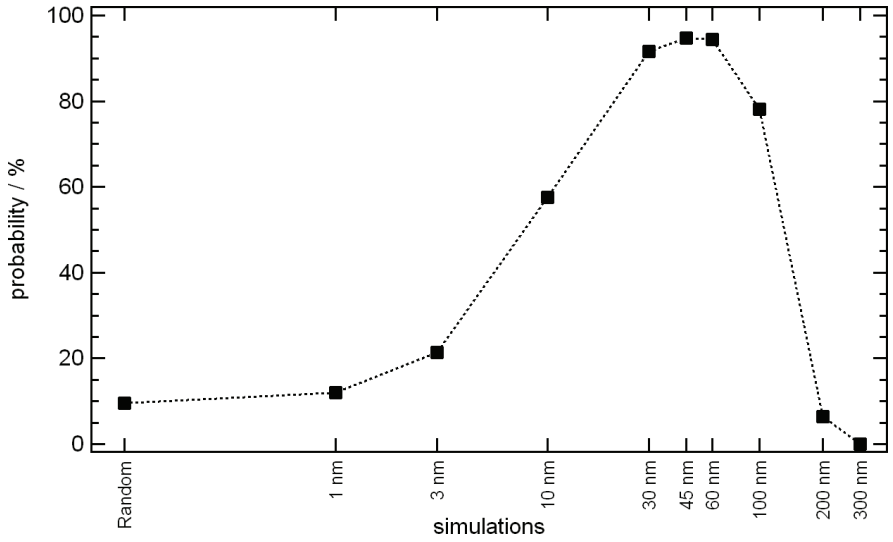

Figure 4.13.: Resulting probabilities for the random distribution with and without diffusion as a function of the different simulated mean diffusion paths.

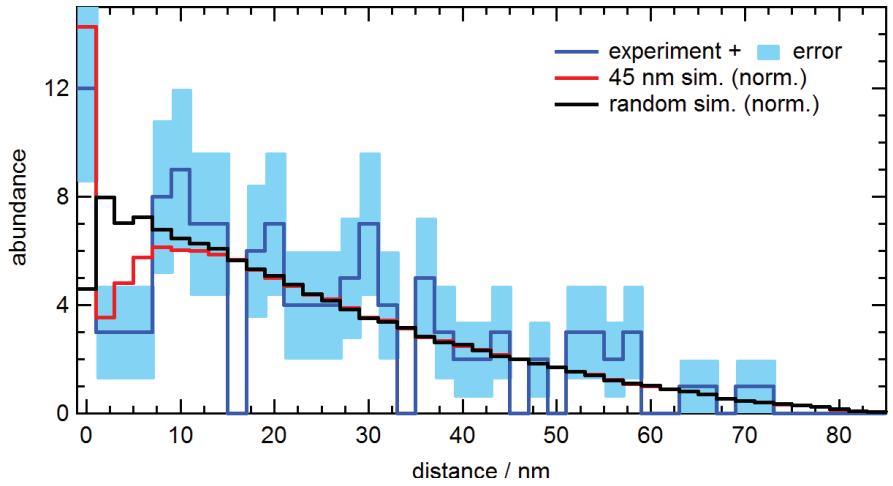

Figure 4.14.: Comparison of the data obtained from the experiment (blue curve) and the simulation random cluster placement (black curve) and with 45 nm MDP (red curve). The indicated error of the experimental data (light blue area) is given by $\sqrt{n}$.

ature gain ΔT upon impact. The first method takes into account the energy gain ΔE upon landing, including the adhesion energies of particle and substrate and the kinetic energy of the particle [151]:

$$\Delta E = \frac{E_{adh} + E_{kin}}{2} = \frac{A(\gamma_{Ag} + \gamma_{Si})}{2} \tag{4.6}$$

with A being the contact area of the particle, γ_{Ag} and γ_{Si} the surface energies of Ag (5.626 eV/nm^2) and Si (8.5 eV/nm^2), respectively. The factor $1/2$ corresponds to the assumption that half of the energy is dissipated into the substrate. Setting now the energy required for the particle heating equal to the surface energy released to the cluster and applying the

equipartition theorem [152] gives the relation

$$\frac{3}{2}\Delta T N k_B = \frac{\Delta E}{2} \tag{4.7}$$

with N being the number of atoms in the clusters. Using equation 4.6 and 4.7 a temperature increase of 48.8 K is found for a particle with a radius of 4.55 nm. The other way to estimate the temperature gain is the approximation that the whole kinetic energy is transferred into the cluster heating. Taking the specific heat capacity of Ag (0.235 J/gK) and the kinetic energy of 412 eV, results in a temperature increase of about 68 K. Assuming that the clusters have room temperature, the deposition on the substrate would result in a final cluster temperature in the range of 348...368 K. This is far below the melting temperature, which is about 1000 K for Ag nanoparticle of such size [153]. This small temperature gain should make no huge impact in the diffusion properties of the Ag clusters.

Small clusters that are soft-landed on a surface may experience diffusion under certain conditions as shown in different experiments in literature [9, 10, 11]. For larger particles smaller diffusion lengths are expected as the diffusion coefficient D scales with the inverse size of the particle r [39]:

$$D \propto r^{-\beta} \tag{4.8}$$

with β being a factor that depends on the limiting process in the fluctuations of the cluster shape, that are assumed in this model. Larger values of D correspond to a higher mobility of the particles which is the case for small values of r.

In many of the cluster diffusion studies, HOPG is used as substrate. As in this work a Si(111) sample is used, it should be quantitivly compared to HOPG. A first comparison can be done via the activation energy Q_{diff} for diffusion as this energy depends strongly on the considered materials. For the diffusion of Ag atoms on the Si(111)7×7 surface, the value for activation energy varies in literature. A reasonable value is Q_{diff} = 1.3 eV/atom [154], while for Ag on HOPG, or carbon in general, Q_{diff} = 0.83 eV/atom [155]. The diffusion coefficient for a surface diffusion on the atomic scale can be written as

$$D \propto \exp\left(\frac{-Q_{diff}}{kT}\right) \tag{4.9}$$

At room temperature, for Si the Boltzmann factor in the diffusion coefficient is 10^{-22} eV/atom and for HOPG 10^{-14} eV/atom. Comparing the two materials, the values show a huge difference of several orders of magnitude. Inserting a temperature of 470 K into the Si coefficient would result in a similar factor as for the HOPG. So the huge difference of several magnitudes is moderated. From the values it is obvious that on the 7×7 surface less diffusion of Ag is expected than on HOPG.

The low diffusion probability of large clusters on Si substrate implies, that the driving diffusion mechanism is probably not a movement of the whole cluster. Thus a different mechanism may be the dominant process here, e.g. an indirect diffusion of surface atoms on the clusters resulting in a movement of the particle as a whole [143]. This mechanism does

not strongly depend on the cluster-substrate interaction, which would explain the observed results. Hence the properties of the substrate would be less important for the observed particles diffusion.
Studies by Goldby *et al.* [8] show that small Ag clusters on HOPG have a diffusion length in the range of hundreds of nm, which is a lot more than the 45 nm MDP found for the large clusters on Si in this work. This also supports the assumption that the diffusion of clusters is more prominent on HOPG.

In the following section the same Ag nanoparticles, deposited on the 7×7 surface, are used as a model system for a metal-semiconductor contact. The band topology of this system is investigated using the laser-induced surface photovoltage.

4.2. Metal clusters in contact with semiconductor surfaces

Metal clusters on semiconductor substrates serve as a model system for a nanoscale Schottky contact, providing access to the electronic properties of such systems. In this chapter the laser-induced surface photovoltage (SPV) is used for band topology investigations of Ag nanoparticles deposited on a the Si(111)7×7 surface.

4.2.1. SPV on the clean 7×7 surface

In the first step the surface photovoltage is measured a clean p-type 7×7 sample. Figure 4.15 shows the SPV as a function of the laser intensity. It can be seen that the SPV increases very quickly, even at low laser intensities.

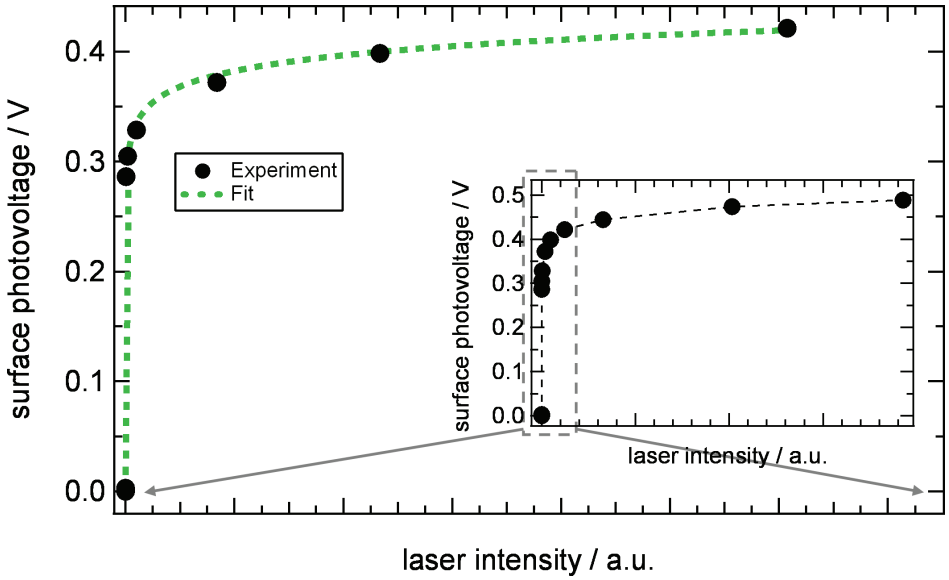

Figure 4.15.: Excerpt from the measurement (see inset) showing the SPV as a function of laser power on a clean p-type Si(111)7×7 sample. An abrupt increase of the SPV occurs at very low laser intensities. The green curve shows a fit of the SPV according to equation 2.17. **Inset:** Complete data from the experiment indicating a saturation around 0.5 V. The maximum laser intensity amounts to 20 mW at 532 nm.

The inset represents the complete experimental data indicating that a real saturated SPV is not achieved according to the measurement. Nevertheless the curve approaches a saturation above 0.5 V SPV. The green curve in Fig. 4.15 shows a fit (later referred to as fit "1") based on equation 2.17 and relates the photovoltage U_{SPV} to the laser intensity P: $U_{SPV} = A \cdot \ln(1 + B \cdot P)$, where A and B are the fit parameters. Such a SPV fit was first applied by Hamers *et al.* [21]. For the here shown SPV curve the following relation is obtained: $U_{SPV} = 0.021\text{V} \cdot \ln(1 + 6.036 \times 10^7 \text{mW}^{-1} \cdot P)$. According to equation 2.16 the parameter A

can be identified with $k_BT/q = 0.026$ V for room temperature ($T = 300$ K). In their work, Hamers *et al.* obtained a value of $A = 0.0306$ V, which fits quite well. Our experiments were done at liquid nitrogen temperature $T = 78$ K, so the resulting A should be $k_BT/q = 0.0067$ V. The deviation of the parameter will be discussed in section 4.2.4.1.
Next to the p-type sample, the SPV is also measured on a clean n-type 7×7 sample. Fig. 4.16 shows several $I(V)$ curves measured at different locations over a small area of the surface. Although the curves differ in the details, the shift of the zero-crossing is quite similar. From these curves a SPV value of $U_{SPV} = -0.49 \pm 0.01$ V is obtained, which is in accordance with the value of -0.47 V found by Losio *et al.* [156].

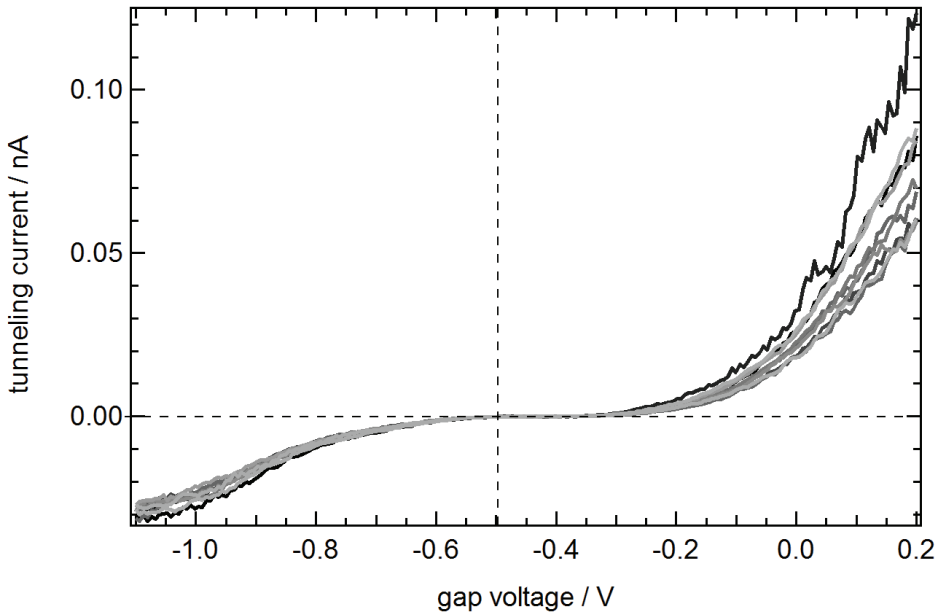

Figure 4.16.: I(V) curves at different locations on a clean Si(111)7×7 n-type substrate sample extracted from grid spectroscopy showing the saturated surface photovoltage of -0.49±0.01 V.

The clean substrate are used in the following experiments for the deposition of metal nanoparticles and for the creation of the 5×2 chain structure.

4.2.2. SPV of Ag nanoparticles on 7×7

In this experiment, size-selected Ag clusters with an average height of about 6 nm are produced with the ACIS and deposited on the clean p-type Si(111)7×7 substrate. The particle density can be estimated from topographic images like Fig. 4.17 to about 1.4×10^{10} particles per cm^2. The large distances to the next neighbors allow measurements on single clusters and prevent agglomeration of the particles. In Fig. 4.18 a single cluster is shown on the atomically resolved substrate. Some boundaries between different 7×7 patches are visible

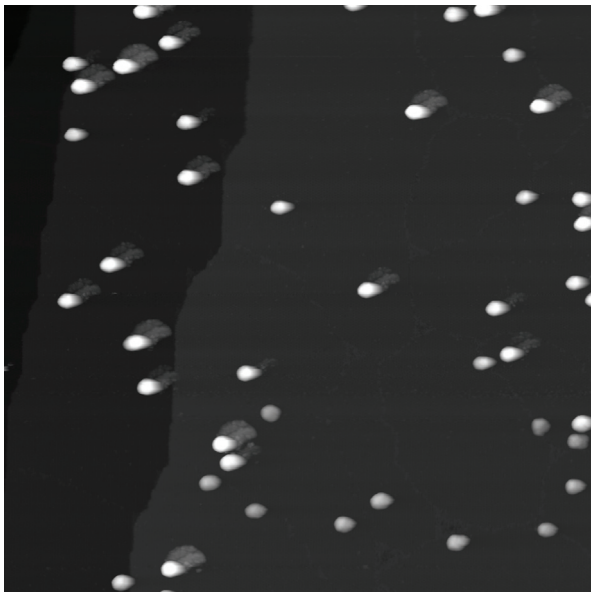

Figure 4.17.: Ag clusters deposited on Si(111)7×7. The cluster density is about 1.4×10^{10} cm^{-2}. The cluster appear as bright spots. The substrate shows different terraces indicated by the different shades of grey. (500 nm × 500 nm, $U_{gap} = -1.0$ V, $I_T = 15$ pA)

Figure 4.18.: Topographic image of a Ag cluster deposited on Si(111)7×7. The particle height is about 6 nm. An adaptive nonlinear color scale has been used to emphasize both the cluster and the substrate (100 nm × 100 nm, $U_{gap} = -1.0$ V, $I_T = 15$ pA)

and appear as dark lines [157], partly decorated by adsorbates. The density of the residual contaminations, that show up within the 7×7 reconstruction, has not increased significantly upon cluster deposition, confirming clean deposition conditions. The clean interface between the Ag clusters and the Si substrate allows investigation of well-defined nanoscale metal-semiconductor interfaces that only depend on the contact facet of the nanoparticle. To gain access to the electronic properties of such an interface, especially the magnitude of the Si bulk band bending and thus the local Schottky barrier, the SPV is measured as a function of the lateral location on the sample. With the help of the SPV the band topology of such metal-semiconductor systems can be investigated.

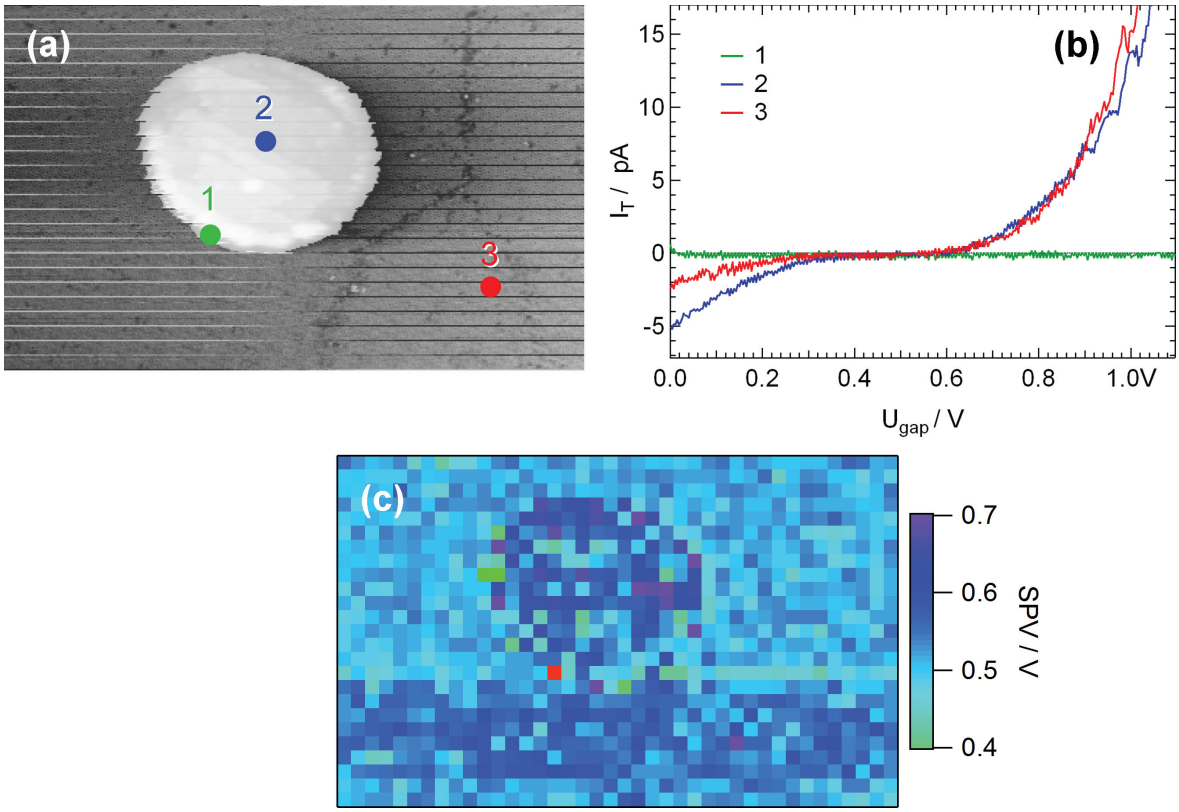

Figure 4.19.: **(a)** Topography of the measured cluster. The horizontal lines are artifacts originating from the performed grid spectroscopy. **(b)** Single $I(V)$ curves taken on the marked positions in (a) showing a noisy signal in the range of the zero-crossing. **(c)** Map of the surface photovoltage obtained from the zero-crossing shift of each $I(V)$ spectrum of the grid. Setpoint: $U_{gap} = 1$ V, $I_T = 15$ pA.

Figure 4.19a shows another cluster on which the measurement is performed. The horizontal lines in the image are artifacts from the grid spectroscopy that has been carried out on this cluster. They only appear in the topographic image and do not alter the spectroscopy measurement in any way. The resulting spectroscopy data have been analyzed regarding the shift of the zerocrossing of each $I(V)$ curve of the grid. Fig. 4.19b shows three extracted $I(V)$ curves taken on the marked positions in (a). The zero-crossing can be roughly estimated

from curve 2 and 3 to be somewhere around 0.5 V. But due to the noise in the single spectra it is difficult to evaluate the exact zero-crossing position $I(V) = 0$, especially in curve 3 which only shows noise around 0. After the SPV is evaluated for each grid position, a spatial resolved SPV map is obtained, which is shown in Fig. 4.19c. From the map it is obvious that the SPV is in the same range on both the substrate and the cluster. Nevertheless, the cluster can be clearly located due to some distinctive peaks in the SPV at the cluster border. These peaks appear preferably when the tip reaches the edges of the cluster, resulting in unstable tunneling conditions. This causes invalid $I(V)$ curves like the green curve 3 where no current is measured at all. Such invalid curves lead to wrongly determined SPV values appearing in the map. The smaller variations in the map originate from the noise around $I = 0$ in the single spectra. For obtaining the SPV the original curve is smoothed to minimize the noise in the signal (cf. also Appendix A.3). However, if the noise is too heavy, even the smoothing does not help. The zero-crossing will then be located with an offset as the real zero-crossing cannot be clearly determined. Another change in the SPV is visible in the lower part where the SPV seems to be higher (dark blue) than in the upper part (light blue). This suggests that when the tip hits the particle, unstable tunneling conditions occur again resulting in a change in the $I(V)$ curves. Additionally, the SPV map shows high values around 0.7 V next to low values around 0.5 V in the area of the cluster leading to an inconsistent analysis. In order to avoid such artifacts it is more accurate to compare averaged curves on the cluster and on the substrate. Such averaged $I(V)$ curves are shown in Fig. 4.20a. The red curve represents the substrate and the dark blue curve the Ag cluster. Under laser illumination the curves are shifted to the right such that for small positive voltages a negative current is observed.

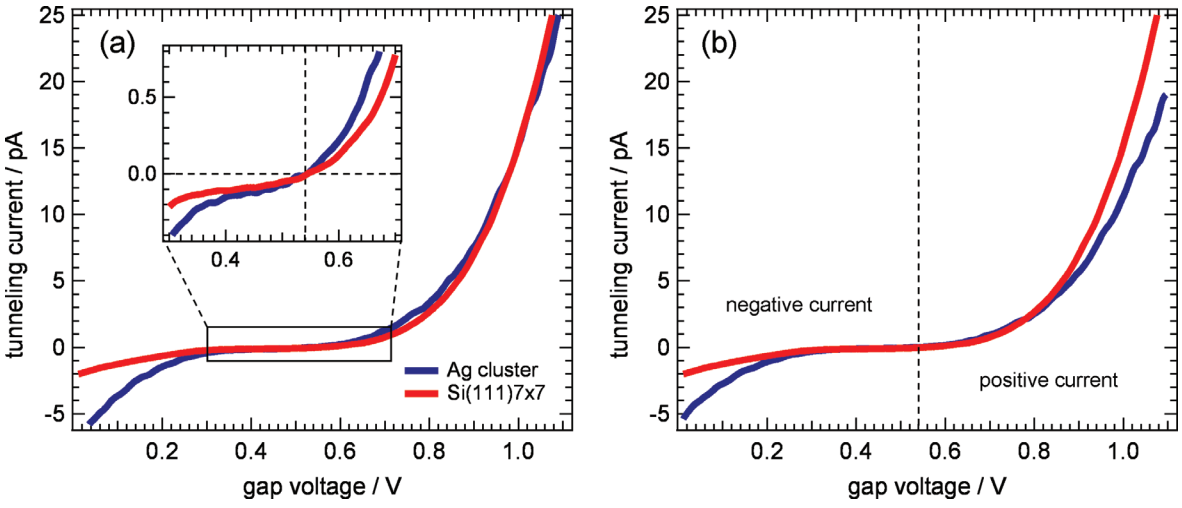

Figure 4.20.: **(a)** I(V) curves measured on a Ag cluster (blue) and on the Si(111)7×7 substrate (red) while the sample is illuminated. The inset shows the magnified region around the zero-crossing. Setpoint: $U_{gap} = 1.0$ V, $I_T = 15$ pA. **(b)** Same as (a) but with the Ag cluster curve scaled by the factor of 0.75. See text for details.

In the inset of Fig. 4.20a a magnified view of the zero-crossing region is shown. The zero-

crossing ($I(V) = 0$) occurs at $U_{SPV} = 0.54 \pm 0.01$ V for both the Ag particle and the clean 7×7, respectively. In contrast, the expected photovoltage should be $U_{SPV,calc} = 0.62$ V which corresponds to the difference of the Fermi-level positions relative to the valence band maximum (VBM) at the surface

$$E_F - E_{VBM,surface} = 0.65\,eV[156] \tag{4.10}$$

and in the bulk

$$E_F - E_{VBM,bulk} = 0.03\,eV[35] \tag{4.11}$$

The deviation of 80 mV is possibly due to an incomplete saturation on this wafer or due to a slight cluster-induced reduction of the saturated SPV. Interestingly, within the experimental accuracy of ≈10 mV there is no significant SPV difference between the cluster and the bare substrate. The same result is obtained on several Ag clusters for verification.
Both $I(V)$ curves in Fig. 4.20a show quite similar characteristics except in the region of negative current ($U_{gap} < 0.54$ V). However, both curves are pinned by the setpoint, which is at $U_{gap} = 1.0$ V and $I_T = 15$ pA. Here the curves have the same value per definition. An equivalent view of the curves is shown in Fig. 4.20b, where the blue curve is scaled by a factor of 0.75 for a better visualization. It can be seen that in the region of negative current the cluster curve shows still higher currents than the substrate curve, but less current in the region of positive current. The curve shows similar characteristics as a Schottky diode operated under forward bias at negative currents and under reverse bias at positive currents. So this metal cluster-semiconductor shows transport characteristics of a Schottky contact. This can be explained as not only the metallic 7×7 surface is involved in the current transport but also the underlaying bulk semiconductor.
Measuring the same SPV on the cluster and on the substrate can be caused by three possible effects resulting in such an observation:

1. the surface photovoltage is not yet saturated on both structures and the difference appears at higher photon fluxes only
2. the Fermi level pinning of the Ag-Si interface is exactly the same as for the plain 7×7 surface
3. the lateral Fermi potential is efficiently equilibrated such that electric fields are suppressed and a common SPV is established

Although it is difficult to strictly rule out possibility 2 there are strong indications to do so: the shift of the surface photovoltage is the same for all clusters on the sample. It is very unlikely that the different interface states of the randomly landed clusters result in exactly the same Fermi-level pinning. This leaves possibilities 1 and 3 for the physical origin leading to the observed absence of SPV variations. For a further discussion now a different system is investigated, i.e. patches of 5×2 on Si(111), which serves as a model system.

4.2.3. The Si(111)5×2-Au reconstruction as a model system

The Si(111)5×2-Au reconstruction is ideally suited as a model system for studying the topology of the Si bulk bands: first, the Fermi-level pinning is very different on 7×7:

$$E_F - E_{VBM} = 0.65\,eV [156] \tag{4.12}$$

than on 5×2

$$E_F - E_{VBM} = 0.06...0.22\,eV [82] \tag{4.13}$$

thus the expected SPV variations should be easily detectable. Secondly, the lateral transition between the two phases is atomically sharp, such that the length scale of changes in the band bending at the surface is accessible. Thirdly, the patch size and the patch density can be easily controlled during the preparation, providing the possibility to tailor the system. In this experiment n-type Si(111) samples are used because there the largest photovoltage is expected. On an ideally covered 5×2 surface McChesney *et al.* obtained a SPV of $-0.93V$ [82]. On a partly covered surface (cf. section 2.5, Fig. 2.14) the absolute SPV rises on a 5×2 patch from $0V$ to -0.93V with increasing laser intensity, which is shown in Fig. 4.21 and indicated by the dark blue circles.

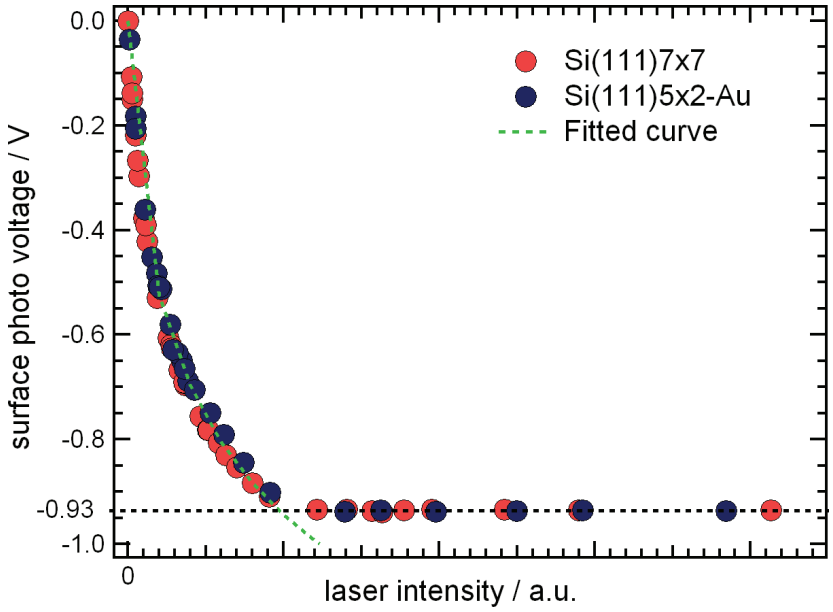

Figure 4.21.: Photovoltage as a function of laser power. It saturates at about -0.93 V for both 7×7 and 5×2 structures. The maximum laser intensity amounts to 20 mW at 532 nm. The green curve shows a fitted photovoltage for non-saturation.

The curve saturates quite abruptly at $\text{SPV}_{\text{sat}} = -0.930 \pm 0.015$ V. From this value we can directly evaluate the Fermi level pinning (Fig. 4.22) for the 5×2 reconstruction:

$$E_{F,5\times2} - E_{VBM,5\times2} = -(E_{CBM,bulk} - E_{F,bulk}) - SPV_{5\times2} + E_{gap} = 0.2eV. \tag{4.14}$$

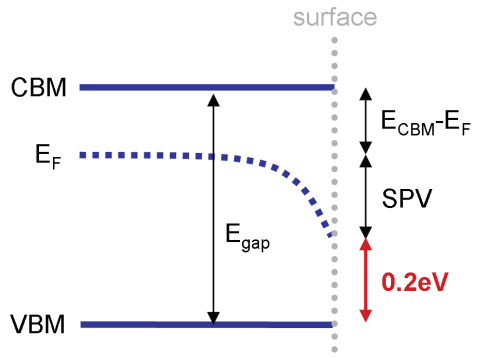

Figure 4.22.: From the SPV measurement the Fermi level pinning of the 5×2 reconstruction could be determined to: $E_F - E_{VBM} = 0.2$ eV.

This value is consistent with the determined range of the Fermi-level pinning position in [82]. Furthermore, an absolute value for the Fermi-level pinning of the 5×2 is obtained.
On a 7×7 region of the same sample the SPV (indicated by the red circles in Fig. 4.21) follows exactly the curve for 5×2 and saturation occurs again at $U_{SPV} = -0.930$ V. This photovoltage is almost a factor of two larger than the expected maximum SPV according to the model in section 2.2. Disregarding the huge value, such a pronounced saturation of the SPV on the 7×7 surface has also been observed by Mönch *et al.* [158] for a temperature of $T = 85$ K. The green curve in Fig. 4.21 shows a fit of the photovoltage (later referred to as fit "2") based on equation 2.17 as it was shown before. For the here shown SPV curve we obtain the following relation: $U_{SPV} = -0.29\text{V} \cdot \ln(1 + 5.28\text{mW}^{-1} \cdot P)$. According to equation 2.16 the parameter A should equal $k_B T/q = 0.0067$ V for liquid nitrogen temperature. The absolute value of A is larger than the parameter for the clean p-type Si sample and shows also a huge discrepancy to the experimental value, which will be discussed in the section 4.2.4.
Similar to the measurements on the Ag cluster sample, the SPV does not show any significant differences between the 5×2 and the 7×7. In fact no dependence on the lateral location could observed at all. Obviously, the 5×2 patches dominate the SPV and thus the photon-induced band bending on this surface. Several experiments with a reduced Au coverage down to a few percent of a ML revealed that even in a distance >200 nm to a 5×2 patch the same SPV is measured on 7×7. This means that the SPV value of the 5×2 dominates the SPV of the 7×7. This is even the case when using p-type Si: here a saturated SPV of about 0.1 V for both 7×7 and 5×2 is observed. In contrast, a SPV >0.5 V is measured for the clean p-type Si sample (cf. section 4.2.1). The reason for the 5×2 domination could unfortunately not be resolved within this work, so this has to be investigated in further studies.
Obtaining the same SPV on both structures, the three possible scenarios that can result in this value have to be taken into account again. The large value of the SPV and the shape of the curves in Fig. 4.21 imply that saturation of the SPV has been reached in this experiment. Therefore, possibility 1 (cf. section 4.2.2) can be directly ruled out as an explanation of the

absence of SPV variations. Scenario 2 cannot be true either because of the known different Fermi-level pinning of 5×2 (cf. Eqn. 4.13) and 7×7 (cf. Eqn. 4.12). This leaves the third mechanism, i.e. an efficient elimination of lateral electric fields, as a possible explanation.
So far a strong Fermi level pinning is assumed, such that the band bending of the bulk bands near the surface can be directly derived from the saturation SPV. To verify this assumption, averaged dI/dV curves from a 7×7 region with and without laser illumination are compared in Fig. 4.23. The features of the measured dark curve goes well together with a similar measurement from Wolkow and Avouris [70], showing that the spectra corresponds to the typical 7×7 structure. If the pinning position is not affected by the illumination a rigid shift of the dI/dV curves along the voltage axis by the amount of $\mathrm{SPV}_{\mathrm{sat}} = -0.93$ V may be expected [22]. This shift can be seen in Fig. 4.23 as indicated with the dotted lines. Applying the reverse shift of +0.93 V to the green curve results in almost identical spectra (inset in Fig. 4.23). This indicates that the electronic structure and thus the Fermi-level pinning remain unchanged upon illumination, except for a global shift due to the induced surface photovoltage.

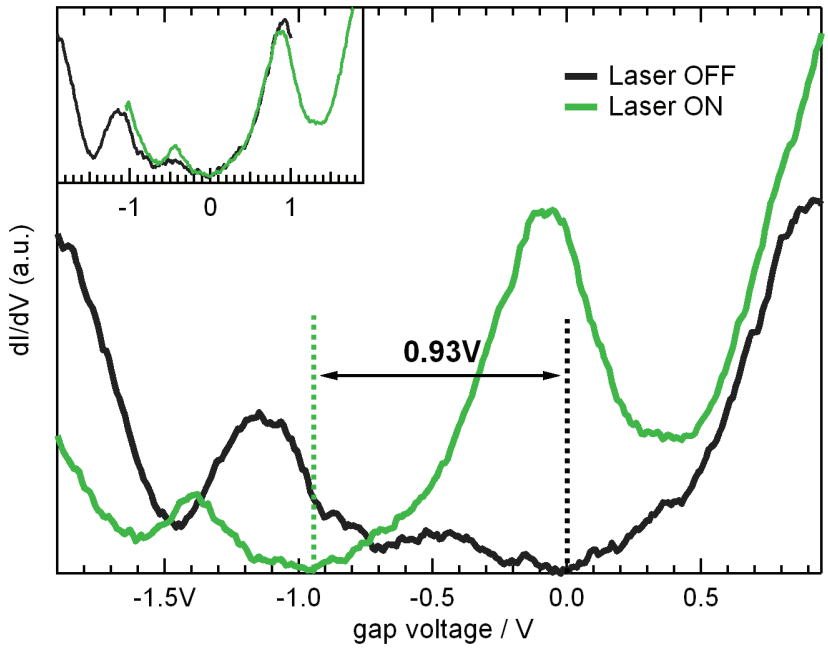

Figure 4.23.: Comparison of averaged dI/dV spectra on a Si(111)7×7 region with (green) and without (black) illumination. The markers indicate the 0.93 V shift of the spectra. - **Inset:** the green curve (laser on) is offset horizontally by 0.93 V and scaled vertically to fit the black curve (laser off).

However, some of the previous results are quite surprising and can not intuitively be explained. For a better understanding, a closer look to the band topology of the 7×7-5×2 junction is helpful.

4.2.3.1. Model of the band topology

To summarize and understand the obtained results from the SPV experiments a simple model for the band topology of a junction between a 7×7 and a 5×2 patch is developed. It is illustrated in Fig. 4.24. The left image (a) shows the "dark" system which is in equilibrium,

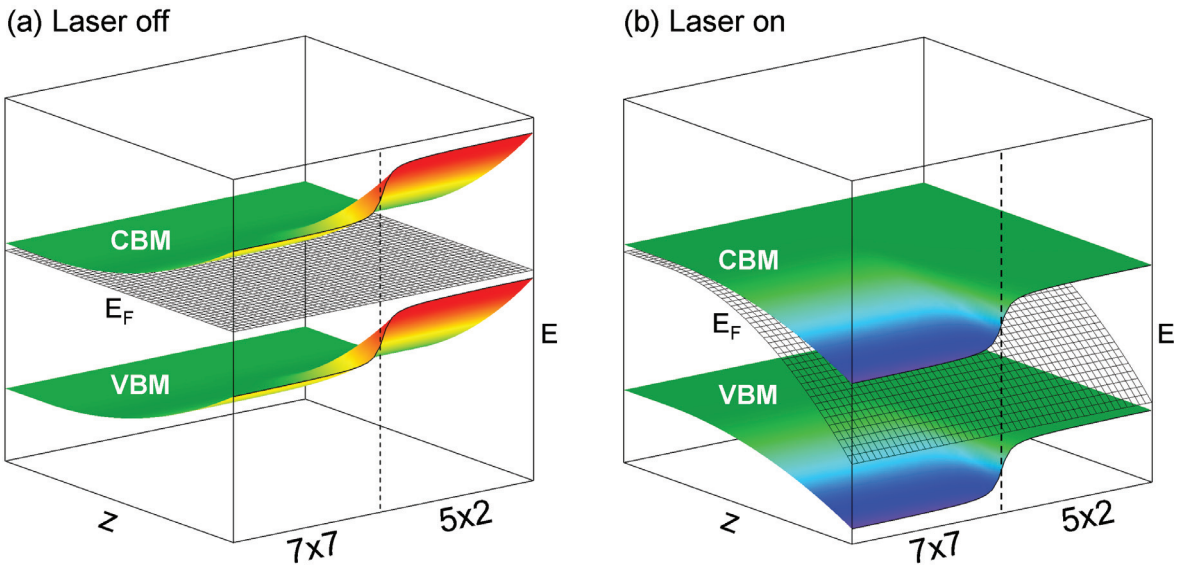

Figure 4.24.: Band model of the 7×7 and 5×2 junction: (a) Different band bending of the 7×7 and 5×2 structures at the surface. (b) The laser light induces a downward band bending of about 0.93 eV on both structures. As a result the same SPV value is measured on 7×7 and 5×2.

while the right image "b" shows the system under laser illumination. The front of the box represents the surface of the 7×7 and 5×2 junction, while the "z" axis indicates the direction into the bulk Si which is located in the back. The colored planes represent the conduction band minimum (CBM) and the valence band minimum (VBM), respectively. The color itself indicates the bending of the bands: red corresponds to an upward bending and blue to a downward bending from the bulk level (green). The Fermi level E_F is represented by the grey shaded plane. In the bulk it is located near the CBM. In equilibrium, without the laser, the band bending in 7×7 and 5×2 are different as the Fermi level E_F of 7×7 is pinned near the middle of the gap, while on 5×2 it is pinned near the VBM (Fig. 4.24a). The gradient of the potential is modeled in a simple parabolic way for the band bending, assuming a constant charge within the Debye length. The transition between the structures is approximated in this model by a polynomial function and does not represent the real characteristics. However, as the transition takes place on a very narrow length scale, which can be seen in the FER measurements in the next section, this approximation is justified.
When turning on the laser, the sample is illuminated (Fig. 4.24b) and a downward band bending of -0.93 eV is induced. As the same photon-induced bending occurs on both structures, there is no difference in the Fermi levels and hence no variation in the photovoltage.

As a result the same SPV is measured on both structures. Interestingly, the bulk bands on the n-type 7×7 bend downward, a situation that cannot be created on homogeneous systems without an external electrical field.
The result that no SPV variation is measured can be attributed to an efficient elimination of any electrical fields associated with SPV variations on the surface. The reason is the metallic character of the 7×7 and 5×2 surface reconstructions [156, 159]. This applies to scenario 3 discussed in the previous section. As a consequence there is apparently no formation of a lateral Schottky contact at the surface, which is in accordance with the results of Schmeidel *et al.* [160]. Instead, the transition between the two structures corresponds to a 1D metal-metal junction, where any photon-induced potential differences are efficiently equalized.
This simple model of the band topology implies that the work-function is different on the 7×7 and 5×2 structures. For verification of this assumption, a supplemental experiment is performed which is presented in the next section.

4.2.3.2. Spatially resolved local work function from field emission resonances (FER)

Assuming that the local work function (LWF) is predominantly determined by the Fermi-level position within the gap the band topology model in Fig. 4.24 suggests a LWF difference between the two coexisting structures. Such variations in the LWF can be detected via the onset of field-emission resonances (FER) that are related to image potential states [161, 162]. The effective potential between the tip and the surface is not attempted to be accurately modeled here, as it is done e.g. by Poligt *et al.* [163]. The FER onsets are rather compared in a qualitative manner. This supporting experiment and analysis of the FERs were performed by S. Polei [164].
In Fig. 4.25 the spatial dependence of the FER at a junction of 7×7 and 5×2 is summarized. Figure 4.25a shows the topography where the 7×7 (left) and 5×2 (right) structures are clearly visible. In Fig. 4.25b a map of the spatially resolved energy position of the first dI/dV peak is shown. Large voltages correspond to bright grey. The FER that are obtained from STS are shown in Fig. 4.25c. The FER variations (Fig. 4.25c) are the result of changes in the local work function. Due to the different Fermi-level pinnings the first FER peak is shifted towards larger voltages on 5×2, directly reflecting an increased work function compared to 7×7. As a result two peak positions are obtained for both structures: 4.7 V for 7×7 and 5.3 V for 5×2. These values do not reflect absolute values of the work function, only the difference can be used as a qualitatively hint for the different work function of both structures. The lateral length scale of the work-function change and thus the bulk band bending near the surface can be obtained from the data in Fig. 4.25b. The transition from dark grey to light grey is very narrow and its upper limit can be quantified to $\Delta l < 2$ nm, which is more than a factor 30 less than the bulk Debye length of Si $\lambda_D = 60$ nm and comparable to a metallic substrate [163]. This allows the conclusion that the formation of a

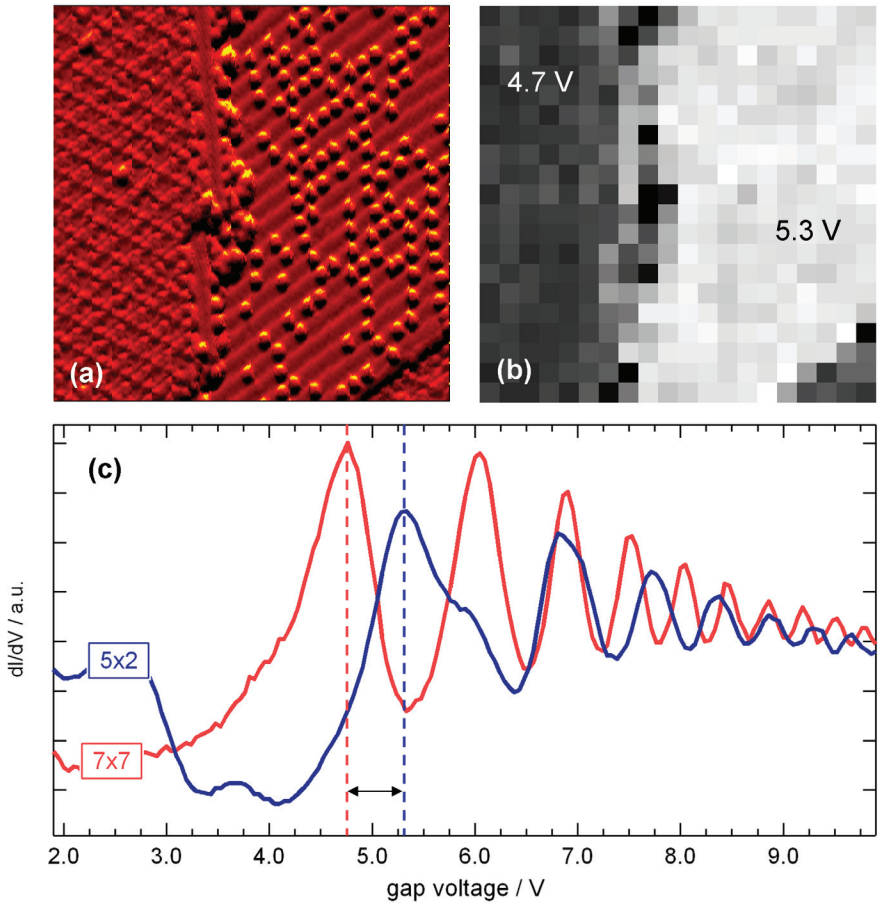

Figure 4.25.: (a) STM image (derivative display) of a junction between 7×7 (left) and 5×2 (right) (40 nm × 40 nm, $U_T = -2.0$ V, $I_T = 50$ pA). (b) Spatially resolved map of the energy position of the first dI/dV peak. Large voltages are bright. Variations are due to changes of the local work function. (c) Averaged FER spectra obtained from a dI/dV map on 7×7 and 5×2, respectively. The position of the respective first peak are indicated by the dashed lines.

one-dimensional 7×7-5×2 junction on the Si(111) surface can be described in analogy to a contact of two bulk metals.

4.2.4. Discussion

By comparing the results of the 5×2 SPV experiments to the findings of the SPV experiment on deposited Ag cluster, several implications can be drawn. First of all, a direct measurement of the Fermi-level position and hence the Schottky barrier around a metal nanoparticle is not possible via SPV mapping on semiconductors with metallic surface states, like e.g. Si(111)7×7. The reason is the absence of local SPV variations. Instead a common SPV is observed throughout the sample surface. The results suggest that even on scarcely covered

cluster samples the SPV can be significantly altered compared to the clean substrate. Furthermore, a Schottky-based device with dimensions in the nm-range can hardly be realized on a semiconductor sample with strong metallic surface states. The latter form a metallic layer on top of the semiconductor that equilibrates any lateral electrical fields, so that no potential differences can be measured. Since the nanoparticle is electrically connected to this layer a current that passes through the device is likely to be spread out over a region much larger than the particle itself. The lateral evolution of the bulk band bending around a metal nanoparticle on Si(111)7×7 is schematically depicted in Fig. 4.26.

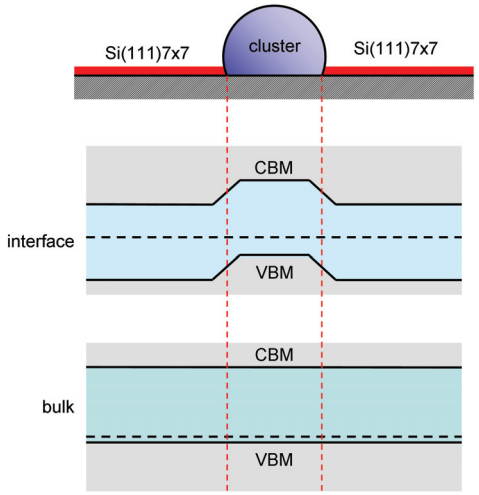

Figure 4.26.: Topology of the cluster-surface system with the corresponding schematic band structures at the surface and in the bulk. The cluster is in electrical contact with the metallic surface reconstruction.

Although the Schottky barrier shows a variation in the vicinity of the cluster, there is no formation of a confined Schottky contact because of the metallic surface reconstruction. However, the physical conditions for the formation of a nanoscale Schottky-contact are virtually the same as for inhomogeneous photovoltages for such systems. The measurement of SPV variations is thus a promising technique to elaborate whether a particular system is an eligible candidate for a nanoscale Schottky device.
In the following, two aspects of the results will be discussed in more detail. First the deviations in the SPV fit, showing different values than those known from literature, will be discussed. In the second part the current transport mechanisms that are involved in the SPV will be discussed with respect to the obtained results.

4.2.4.1. Deviations in the SPV fit

From the fitted SPV curves the obtained values show all a discrepancy to the expected values. In the following several possibilities will be discussed that may explain such values.

In all the SPV experiments, the laser intensity is always measured in relative units. Experimentally there are two main reasons why the quantitative determination of the laser intensity turns out to be inaccurate and would result in large error bars: (1) the laser passes windows of different materials on the path to the sample. This results in different unknown absorptions. (2) The spot size of the laser and its exact position needs to be optimized and adapted to the actual tip location during the experiment. Due to the high reflectivity of the silicon samples a visual determination of these quantities is not possible. Therefore only the relative laser intensity is logged here. However, this does not influence the value of the parameter A: considering the SPV equation $U_{SPV} = A \cdot \ln(1 + B \cdot P)$, it can be shown that for a given U_{SPV} a change of the intensity P results in a contrary change of the fit parameter B and in no change in the parameter A. So the value of A is completely independent from the magnitude of the laser intensity. For a further discussion, the current transport mechanisms that are shown in section 2.2.1 are now taken into account.

The calculation of the surface photovoltage (cf. section 2.2.1) that is used in the literature is always based on the assumption that the dominant current transport mechanism is thermionic emission [21, 43, 42]. Contributions from electron tunneling and recombination are totally neglected in this assumption. But this model of the SPV, which is based on the Schottky model, is only valid for high temperatures, i.e. room temperature and above [35]. As the here shown SPV experiments were all performed at $T = 78$ K, the discussion about the dominant transport mechanism has to be revised.

From works e.g. by Chen *et al.* [165] and Chand *et al.* [166] it is known that at low temperatures the mechanisms of recombination and electron tunneling play an important role and cannot be neglected in the discussion. For the tunneling current Chen *et al.* [167] gave a rough estimation that this contribution becomes important when $E_{00} > kT$, with E_{00} being a quantity which is given for electrons at the edge of the space charge region by $E_{00} = 18.5 \times 10^{-15} \cdot (N_d/m_r\epsilon_r)$. For the Si(111) sample used in this work, this would result in E_{00}/kT = 0.05 for 300 K and E_{00}/kT = 0.2 for 78 K. Therefore it can be assumed that the contribution of the electron tunneling current does not play a significant role in this work.

A first indication that the thermionic emission process plays a less important role in our experiments can be directly estimated by the SPV calculation (cf. equation 2.16) that is characterized and mainly driven by a Boltzmann factor of the type $\exp(\phi_b/kT)$. Comparing this factor for high and low temperatures with a constant barrier height ϕ_b, the result is that at liquid nitrogen temperature the effect of thermionic emission is 48 orders of magnitude smaller than at room temperature.

With the presumption that the current transport mechanisms can be very different at low temperatures, the two SPV fits shown in section 4.2.2 and 4.2.3 have to be reviewed. The fit "1" in Fig. 4.15 describes the photovoltage on a p-type Si(111) sample as a function of the laser intensity. It is based on the SPV calculations for the non-saturated SPV: $U_{SPV}(P) = A \cdot \ln(1 + B \cdot P)$ with A and B being the fit parameters and P the laser intensity. The fit yields the values $A = 0.021$ V and $B = 1.888 \times 10^8$ mW^{-1}. As shown before A can be

identified as the factor kT/q that depends only on the temperature. For liquid nitrogen temperature ($T = 78$ K) the factor equals $A = 0.0067$ V. One possible attempt is to try and hold A at a fixed value of 0.0067 V during the fit. But the resulting curve would be completely offset and does not even approximately describe the experimental curve.
The fit "2" was done with the experimental data from the SPV measurements on 7×7 and 5×2 patches. For the results in Fig.4.21 the fit yields the values $A = -0.29$ V and $B = 5.28$ mW^{-1}. The different sign of A reflects the different doping as an n-type Si(111) sample is used here. So the laser induced SPV is of negative sign. In a more or less naive approach one can estimate the temperature that would correspond to the found value of $A = -0.29$ V: $T = 3400$ K. Disregarding the unrealistic high value, a change in the temperature would also result in a different value for the parameter B as it depends on $1/T^2$. However, it is not possible that the sample had such a high temperature, so this is a wrong way to go.
An interpretation of the deviations can be found in the work of Galbraith *et al.* [168]. They introduce the factor n as a parameter that describes the experimental I-V characteristics, resulting in a modified equation for the SPV:

$$U_{SPV} = \frac{nkT}{e} \ln(1 + \frac{\exp(\phi_b/kT)}{A^* T^2 h\nu} P) \tag{4.15}$$

The parameter n is used as a correction factor that fits the experimental data with the theoretical calculation. At room temperature and light doped samples, n equals about 1. For low temperatures and higher doping levels n gets increases and gets larger than 1, e.g. $n = 2$ for a n-type GaAs Schottky diode with a doping level of 1×10^{17} cm^{-3} and $T = 77$ K [168]. Bednyi *et al.* [169] gave an interpretation of the factor n being an equivalent to the ideality factor in a Schottky diode. The ideality factor indicates how closely the diode follows the ideal diode equation and depends on the dominating current transport mechanism. Therefore n should be ideal, i.e. $n = 1$, for a SPV resulting from thermionic emission, smaller than 1 when surface trapping of excess carriers is present and about 2 in the presence of significant bulk trapping and recombination [170]. So the value of n indicates which mechanism is dominantly driving the SPV. From our experiments an ideality factor of $n = 3$ for fit "1" and $n = 43$ for fit "2" is obtained. Taking these values and the above interpretation of the mechanisms, it can be assumed that in this work, the thermionic emission does not play a significant role in the SPV mechanism. In the here shown low-temperature experiments the recombination process could be more present and therefore has to be taken into account.
Another proof that the recombination dominates the thermionic emission at low temperatures is given by Rhoderick and Williams [171]. They show that the ratio of the thermionic emission to the recombination current is proportional to $T^2\tau \exp[q(E_{gap} + U_{SPV} - 2\phi_b)/2kT]$. This ratio increases with the carrier lifetime τ, E_{gap} and U_{SPV} and decreases with the barrier height ϕ_b. Because the expression $(E_{gap} + U_{SPV} - 2\phi_b)$ is usually negative for n-type semiconductors, the ratio increases with the temperature T. As a result the recombination current is more important on high barriers, in material of low lifetime and at low temperatures. They also address the recombination current to be a common cause of deviation from

the ideal behavior in Schottky diodes. A very important statement of their work is that the effect of the recombination current has been frequently overlooked in the literature and that those deviations from the ideal model become more pronounced at low temperatures [171]. Considering Schottky diodes, the values of the ideality factor are normally in the range of 1...2. But even larger values for n are possible and observed in the literature. Mangal *et al.* [172], for example, reported on values of $n > 4$. They attributed such high values to barrier inhomogeneities, whereas Osvald *et al.* [173] came to the conclusion that such a high value is an intrinsic property of homogeneous semiconductor interfaces. In this work the Schottky barrier consists of a semiconducting substrate with metallic surface in the case of 7×7 and 5×2. This system forms a homogeneous junction. Therefore possible inhomogeneities can be ruled out here. An ideality factor up to $n = 15$ has been observed by Gupta *et al.* [174] for a gold-strontium titanate thin film Schottky diode. Going from room temperature to lower temperatures (about 150 K) results in an increasing n. They attribute their findings to an accelerated recombination of carriers in the SCR, Schottky barrier height inhomogeneities or other imperfections.
The here observed ideality factors of 3 (fit 1) and 43 (fit 2) show a huge difference of one magnitude, which is really remarkable. Such high values as for fit 2 were not reported in the literature to the best of knowledge. It is obvious that the 5×2 reconstruction causes effects that are not yet theoretically fully understood.

4.3. Catalytically active Ag clusters

In this experiment Ag nanoparticles are deposited on a Si support, which is covered by an Al_2O_3 film. During a catalytic reaction, GISAXS (cf. section 2.7) is used to monitor the size and shape changes of the cluster. In the experiment the selective epoxidation of propylene is performed as a temperature programmed reaction (TPR) with reactant gases, i.e. propylene and oxygen, of a 1% concentration in a non-reactant helium gas atmosphere. The programmed temperature ramp of the TPR during the experiment is schemtatically sketched in Fig 4.27.

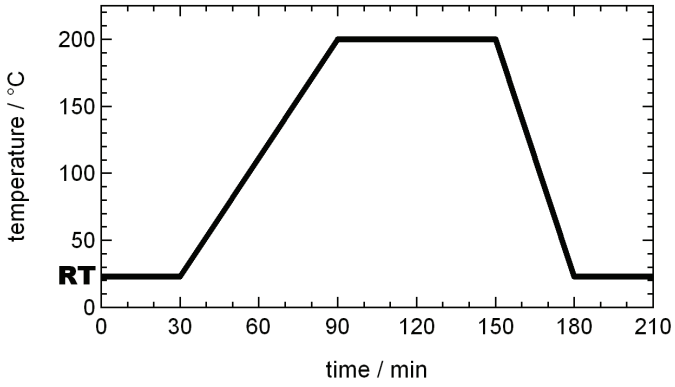

Figure 4.27.: Schematically sketch of the temperature programmed reaction (TPR): progression of the temperature during the time of the experiment.

The sample is kept for 30 min at room temperature (RT) followed by a 60 min heating ramp up to 200°C. After 60 min at 200°C the temperature is reduced back to RT with a 30 min cooling ramp. The heating is always performed very slowly, so that the sample can adapt to the current temperature level.
The cluster are investigated *in situ* with GISAXS during the reaction which is possible due to the special design of the reaction cell. Figures 4.28 and 4.29 show GISAXS patterns of the Ag nanoparticles recorded during the reaction. Fig. 4.28 shows a change in the scattering pattern caused by the reactants at room temperature. The experiment starts at room temperature (23°C) where the reactant gas mixture is let into the reaction cell. After 10 min at the same temperature a directional scattering feature emerges, which is indicated by the yellow arrow. It appears as an "ear"-like feature emerging on both sides of the high peak in the middle. In the image taken after 30 min the angle of the directional feature has changed. Such a directional scattering has been also observed, e.g., on large Pd and Ag nanoparticles by Renaud *et al.* [114] and Winans *et al.* [175]. It corresponds to scattering from the facets of the particles. Figure 4.29 shows the further evolution of the scattering pattern during the proceeding to higher temperatures during the reaction. The angle of the directional scattering changes again during the transition from 23°C to 50°C. At 75°C the directional scattering vanishes and the aspect ratio of the particle changes, which is indicated by the spherical

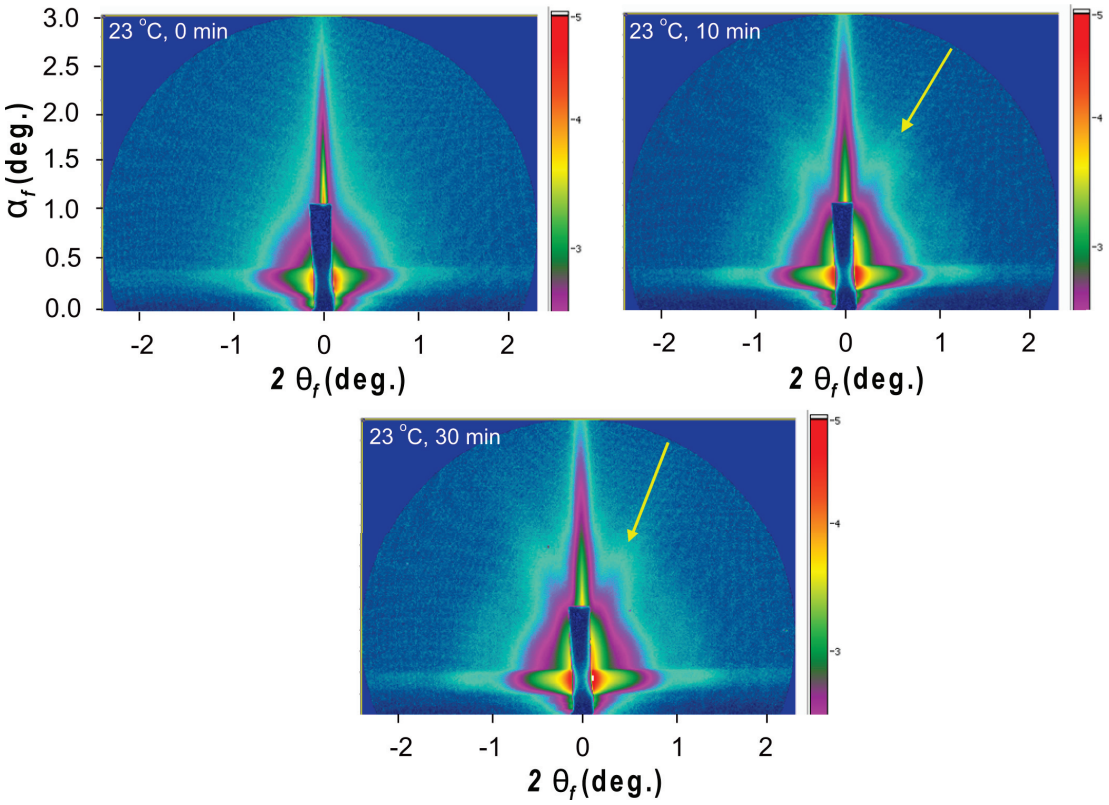

Figure 4.28.: GISAXS images of the nanoparticle scattering at room temperature. From left to the right, top to bottom: image recorded at the time of the inlet of the propylene-oxygen mixture, after 10 min of exposure and after 30 min of exposure. See text for a detailed description.

purple scattering features in the middle of the image. This symmetrical scattering pattern that develops from oval to spherical shape during the temperature progression from 150°C to 200°C is an indication for the formation of spherical nanoparticles.
The data from the GISAXS experiment is analyzed by B. Lee and S. Lee (X-ray Science Division and Vajda Group, Argonne) using the Guinier analysis [121] (cf. section 2.7.1) and a self-written software framework. From the GISAXS images the change of the particle shape can be extracted via horizontal and vertical cuts as described in chapter 2.7. The resulting development of the particle shape during the reaction is shown in Fig. 4.30. The upper graph shows the width and the lower graph shows the height of the particles. The yellow circles in the middle are indicating the change of the aspect ratio. At the beginning after the inlet of the reactant gases the width increases while the height stays nearly constant. When the temperature is increased the particles get flattened as indicated by the yellow sphere. During the following rise of the temperature the width decreases and the height increases, leading to a more spherical particle at 200°C again. This shape is even stable during a further heating at this temperature for another 60 min.

The evolution of the particle aspect ratio determined from the GISAXS images during the

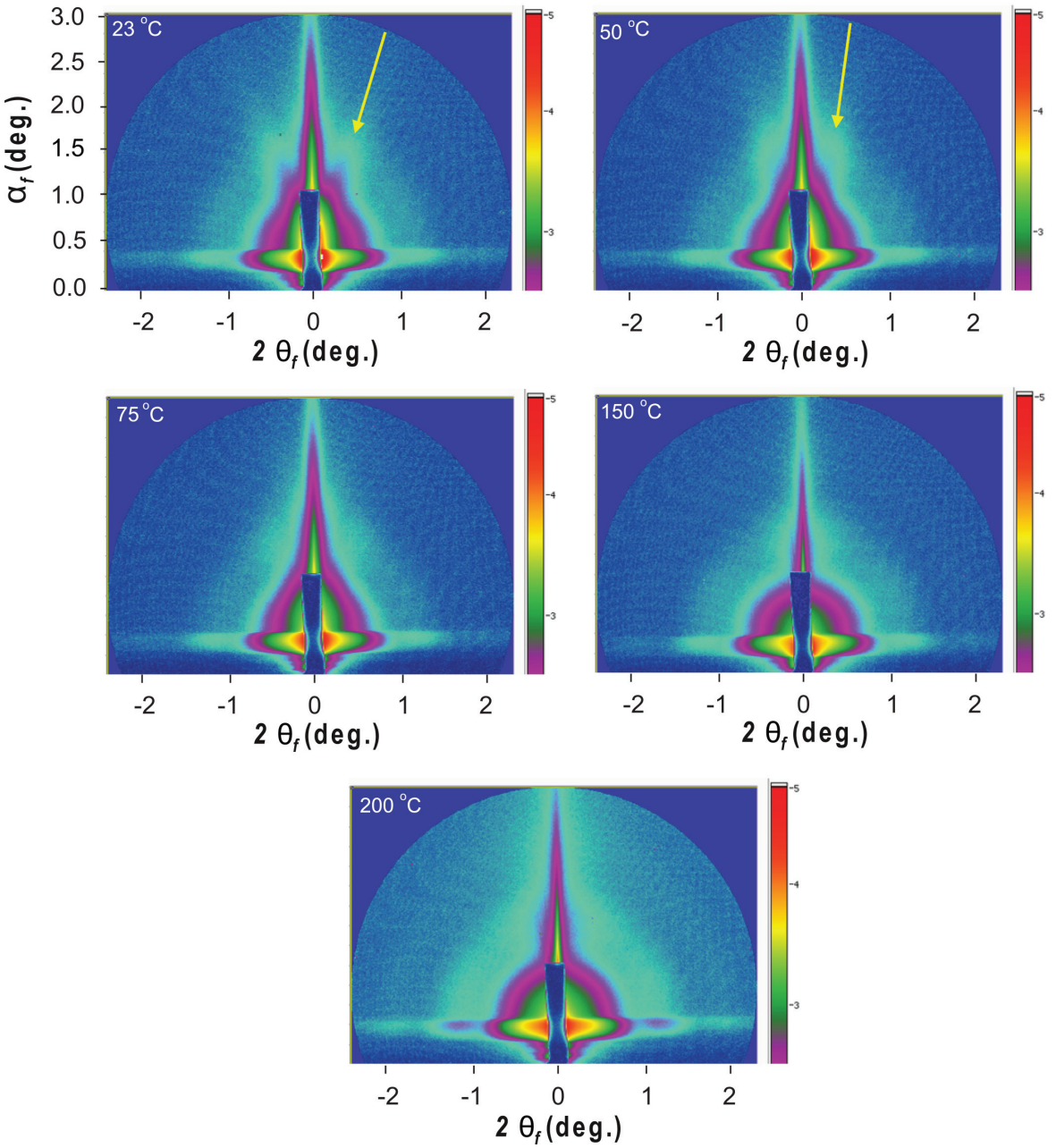

Figure 4.29.: Change of the scattering pattern during the increase of the temperature from 23°C to 200°C. The arrows indicate the directional scattering. See text for a detailed description.

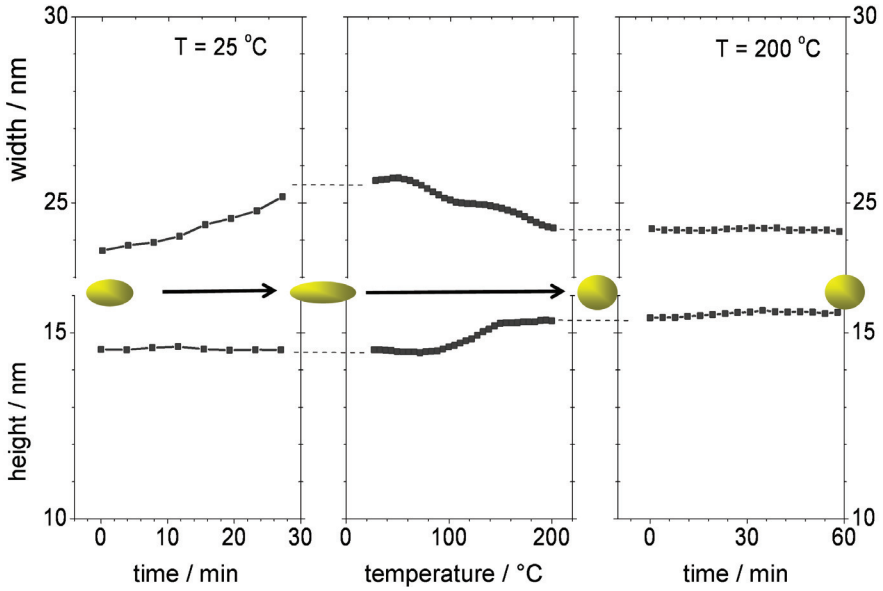

Figure 4.30.: The development of the cluster width (upper graph) and height (lower graph) during the reaction. The yellow circle indicates the aspect ratio during the different stages.

reaction is depicted in Fig. 4.31. In plot (a) the first data point, which is represented by the square, indicates the aspect ratio of the clusters under pure helium. The particles have an average diameter of 21.3 nm and a height of 13.6 nm as determined by GISAXS before introducing the reactant gas mixture. The second data point reveals an abrupt change of the nanoparticle shape at room temperature immediately after propylene and oxygen are ingested into the reaction cell. It is followed by a monotonic increase of the aspect ratio during 30 min of observation at room temperature. With increasing temperature first no notable change in the aspect ratio of the particles is observed up to approximately 60°C. Then the aspect ratio starts to decrease again (plot (b)). After reaching 200°C no further change in the aspect ratio is observed, even during an additional hour of the reaction at a constant temperature of 200°C (plot (c)). The last data point, which is indicated by the star, represents the aspect ratio of the particles after cooling the sample back to room temperature. Here the aspect ratio has reached nearly the initial value from the beginning of the reaction.

Scanning electron microscopy (SEM) is used before and after the reaction for supportive measurements of the particles size [1]. The results are shown in Fig. 4.32 for three samples (#1, #2 and #3) with different cluster sizes. The sizes are obtained by measuring the particle widths from SEM images. The measurement shows that the particle size does not differ within the error ranges before and after the reaction. It also demonstrates that the size measurement with SEM is in good accordance with GISAXS. Unfortunately for sample #3 there is no GISAXS data available as here the cluster density was too low to produce a sufficient scattering signal. However, these three cluster sizes are measured on different

[1] The SEM measurements were done during a collaboration by A. Fraile-Rodríguez (Swiss Light Source, Paul Scherrer Institut, Villigen PSI, Switzerland [112])

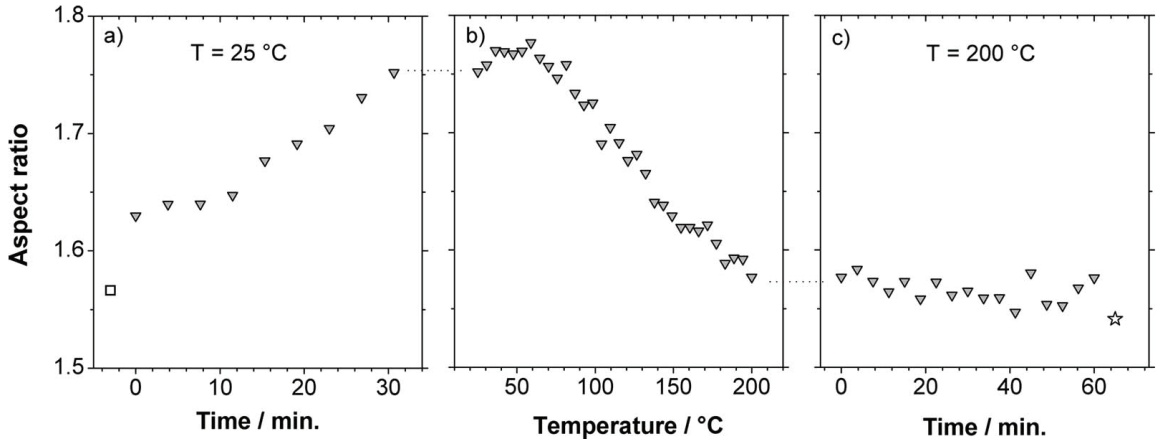

Figure 4.31.: (a) Square: aspect ratio of silver nanoclusters in pure helium atmosphere at room temperature. Triangles: time-dependent change in the aspect ratio after the introduction of the propene and oxygen mixture. (b) temperature-dependent aspect ratio of the silver nanocatalyst. (c) Triangles: aspect ratio as a function of time at constant 200°C. Star: aspect ratio after cooling back to room temperature..

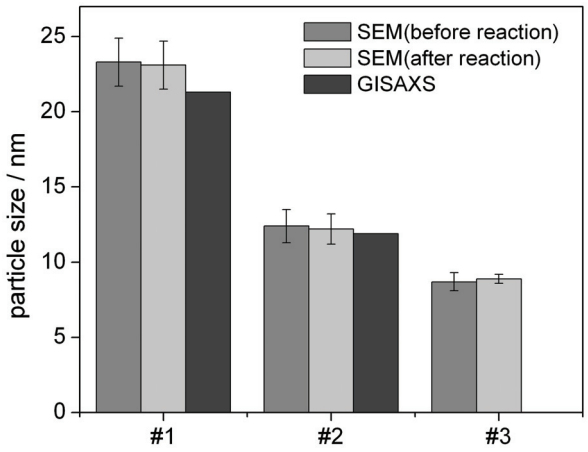

Figure 4.32.: Comparison of the particle sizes measured with GISAXS and SEM before and after the reaction. It shows that the sizes determined with both techniques are in good agreement.

samples than the sample used for the GISAXS experiment in Fig. 4.30. They are only shown here to give an idea how reliable the GISAXS size measurement is compared to other techniques. Another statement that can be made is that the change of the cluster aspect ratio during the reaction and rise of temperature is reversible, because the same cluster size is measured before and after the reaction. Additionally no indication of particle sintering is observed based on the GISAXS data. This is confirmed by the SEM investigations performed after the reaction, that show an unchanged particle width.

4.3.1. Discussion

The results from the GISAXS experiments show that the nanoparticles undergo a shape change during the catalytic reaction. The scattering pattern in Fig. 4.28 and 4.29 show the development of the several features indicating different changes on the clusters. The directional scattering feature that appears during the reaction indicates scattering from the particle facets. This is well known from experiments and simulations in literature (cf. section 2.7). In Fig. 4.33 a representative GISAXS image from the experiment is shown. The directional facet scattering from the Ag nanoparticles is clearly visible.

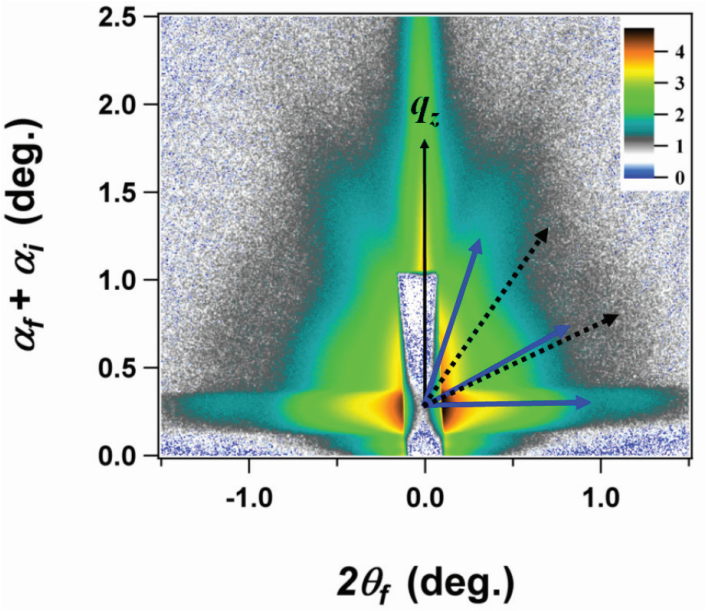

Figure 4.33.: Analysis of the GISAXS pattern of the Ag particles during the reaction. The blue arrows indicate scattering from (111) facets, the black arrows indicate (110) facets. [176]

The blue solid arrows indicate all possible contributions from (111) facet scattering from a single crystalline cluster. Here the particles are assumed to be oriented in a way that the (211) plane is parallel to the substrate surface but the particles are randomly oriented on the surface. This orientation is a result from first taking into account all orientations, followed by modeling the related GISAXS pattern and comparing them with the experimental data [177]. The black dotted arrows indicate the possible contributions from the (110) facet scattering. It is known from literature that the azimuthal angles (the angle between q_z and facet scattering) of the (111) facet scattering are 19.5, 61.9, and 90 degrees [178]. The directional features in the measured GISAXS images are well matched with these (111) facet directions shown by blue arrows suggesting that the (111) plane is a dominant facet of the Ag nanoparticles under the mixture of the reactant gases propylene and oxygen. The disappearance of the directional scattering at higher temperatures that can be seen in Fig. 4.29 may be an indication for changes of the surface energies of the particle in the presence of the gases leading to more

spherical particles shapes and/or the formation of disordered surface structures. So a change of this scattering feature indicates a change in the orientation of the particle facets. This is connected with a change in the wetting angle, which describes the angle between the substrate and the particle shape near the interface layer approximated by a tangent (Fig. 4.34). A change in the wetting layer would correspond to a change in the aspect ratio. As the only difference in this part of the experiment is the inlet of the reactant gases, the change of the directional feature has to be induced by those reactants.

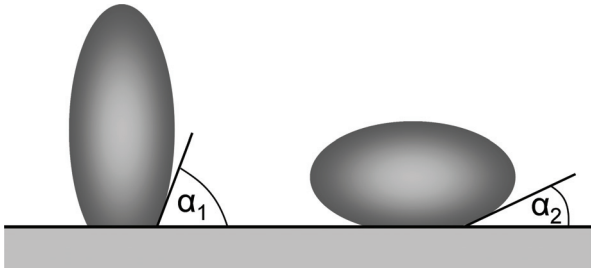

Figure 4.34.: Depending on the particle shape and truncation at the surface the wetting angle can be larger (α_1) or smaller (α_2).

In order to verify the attribution of the observed scattering features to the particle facets, Ag nanoparticles are images with environmental TEM under oxygen (Fig. 4.35a) and hydrogen (Fig. 4.35b) atmosphere. This experiment was done within a collaboration by the Henry group [176].

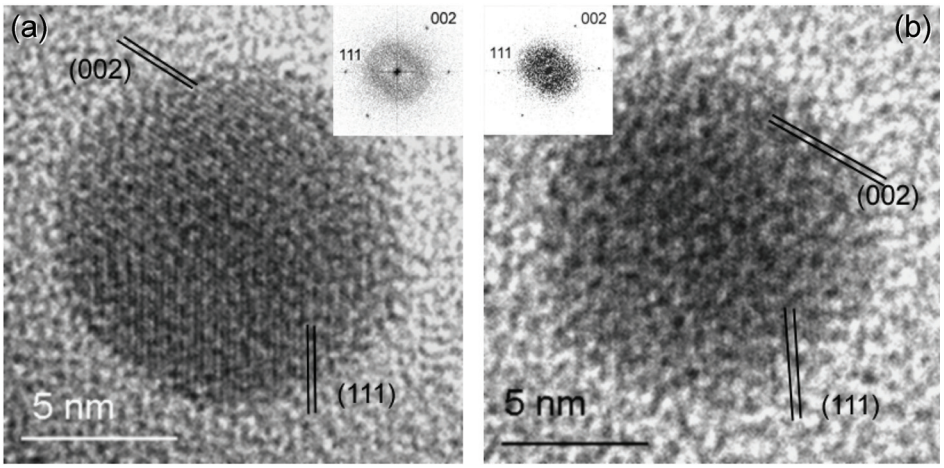

Figure 4.35.: High-resolution TEM images of individual Ag cluster under (a) hydrogen (0.4kPa) and (b) oxygen atmosphere. [176]

For this investigation hydrogen was chosen instead of propylene to mimic competition for oxygen binding with propylene on the surface of the particles, as propylene would possibly cause contamination of the TEM cell. Figure 4.35a shows a Ag cluster under hydrogen at a pressure of 0.4 kPa. From the images and the calculated fast-fourier transformation (inset), it

can be seen that the particle is (110) oriented on the surface. The lateral facets are indicated as (002) and (111) facets. Figure 4.35b shows the same Ag cluster, this time under oxygen at the same pressure. The particle is still (110) oriented but the shape is a bit more isotropic. It is known from literature that oxygen causes an extension of the (001) facets at the expense of the (111) facets [179, 180].
From the GISAXS results the change of the cluster aspect ratio can be directly extracted as it is shown before in Fig. 4.30 and 4.31. In Fig. 4.36 a magnified view of the middle part of Fig. 4.30 is shown.

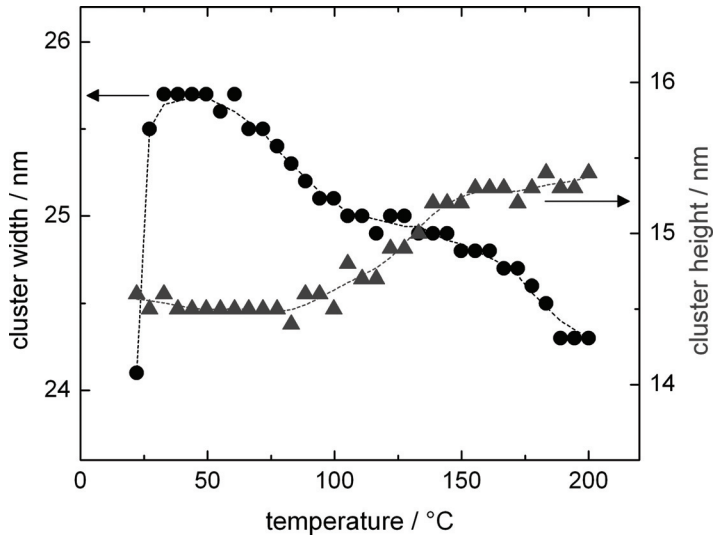

Figure 4.36.: Change of the cluster diameter (blue curve) and height (red curve) as a function of the temperature during the reaction.

It is clearly visible that the width of the cluster, after a first increase from 24 nm to about 25.7 nm, decreases again near to its initial value to 24.25 nm. The height increases during the heating from 14.5 nm to finally about 15.5 nm. This would suggest that the volume of the cluster increases as the height gets bigger by 1 nm. As the number of Ag atoms of a cluster should stay nearly constant during the experiment, one explanation could be that the lattice constant of the clusters is changed by the reactant gases. This is supported by a study of Argo *et al.* [181] revealing that for small clusters propylene ligands cause changes in inter-atomic distances in the particles and affect the cluster-support interaction in Ir/Al_2O_3 and Ir/MgO catalysts. To identify the cause of the shape change that is observed at room temperature, several supporting experiments have been performed with various gas compositions, containing only oxygen, only propylene or a mixture of both. Having only oxygen present in the helium carrier gas, no noticeable change in the cluster aspect ratio is detected. However, a mixture of propylene with oxygen in helium or propylene alone induced the same changes in cluster shape. This indicates that the propylene induces the changes in the cluster shape at room temperature. The binding of ligands may alter the surface energy of the nanoparticle and the strengths of the interaction at the cluster-substrate interface inducing

dramatic shape changes. A similar behavior has been observed by Hansen *et al.* [182] for Cu nanoparticles in a similar size range. As far as the temperature-dependent shape change above 60°C is concerned, in addition to the interaction of the reactants with the clusters several other factors can be considered, such as the change in the chemistry of the support and surface oxide formation on the silver clusters. The alumina surface is OH terminated [183] with water adsorbed on it that starts to desorb from a hydroxylated α-alumina surface at 47°C with a maximum desorption rate at 102°C [184]. In a control experiment, desorption of water from the used Al_2O_3 supports is observed as well, which may also cause changes in the morphology of the nanoparticles. Moreover, partial dehydroxylation of the support during the reaction can affect cluster-substrates interactions which may lead to changes in cluster morphology [185, 186, 187, 188]. Another possible factor leading to morphology changes is the reduction and reoxidation of the metal cluster surface during the reaction [189, 190, 191, 192, 31].
In Fig. 4.37, the equilibrium shape of representative supported Ag particles in the case of clean surfaces (Fig. 4.37a) and in the case of oxygen adsorption (Fig. 4.37b+c) is shown. For simplicity, only (111) and (100) facets are taken into account. The interaction with the substrate translates into a further energy gain for the surface in contact with the support, and as a consequence an increase of the contact area with respect to the opposite face. For clean particles, the anisotropy ratio between the energy of the (100) and (111) surfaces is 1.08, entailing that the area of the (111) faces is larger than that of the (100) faces (see Fig. 4.37a. In contrast, in presence of oxygen adatoms, the ratio is decreased to 0.80 at $p(O_2) = 5 \times 10^{-3}$ atm or to 0.75 at $p(O_2) = 1$ atm, entailing an increase in the area of the (100) faces (see Fig. 4.37b+c). The calculated aspect ratio of the cluster is 1.75 in absence of oxygen adsorption, whereas it becomes 1.44 and 1.53 at $p(O_2) = 1$ atm and $p(O_2) = 5 \times 10^{-3}$ atm, respectively.

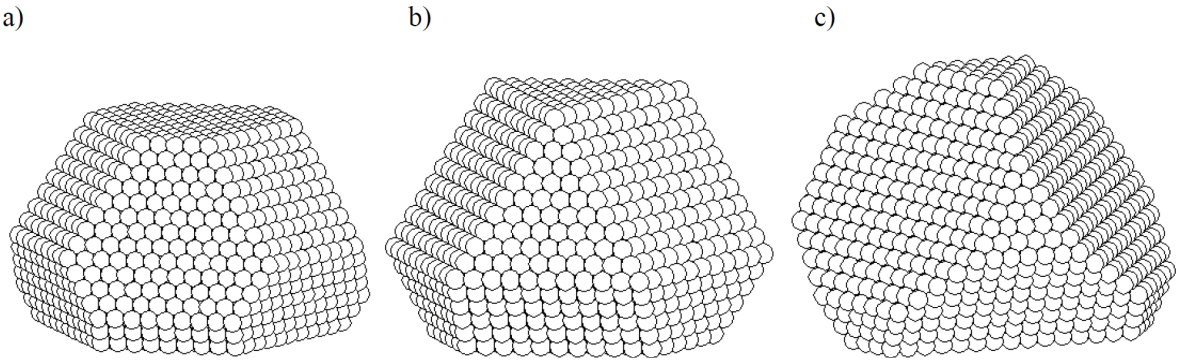

Figure 4.37.: Morphology of supported silver particles in case of (a) non-oxidized surfaces, and oxygen-covered surfaces at (b) $p(O_2) = 5 \times 10^{-3}$ atm and (c) $p(O_2) = 1$ atm. The lateral dimension of the clusters is about 6 nm. [176]

If it is assumed that propylene in the absence of oxygen produces a removal of oxygen atoms from the surface and thus a morphology change to the gas-phase shape of the particles, the predicted aspect ratio is 1.75 for the clean particles. The predicted aspect ratio of 1.53 for the

oxidized particles at p(O_2) = 5×10^{-3} atm is somewhat smaller than the experimentally determined $\approx$1.6 aspect ratio of the oxidized silver particles in the absence of propylene. When propylene and oxygen are co-fed in the reaction mixture, a steady state will be reached, which will depend on the flux, the propylene/oxygen ratio, etc., and in which the oxidation state of the particle surfaces will probably be intermediate between the two limit conditions (pure propylene and pure oxygen).

Although the mechanism that causes the shape change of the particles is yet not fully understood, several possible mechanisms can be taken into account. Nevertheless for a complete understanding additional experiments and simulations are needed in the future.

5. Summary and outlook

In this work several aspects of deposited silver nanoparticles have been investigated, using the techniques of STM and GISAXS. In the first part of the experiments, the diffusion properties of the clusters after deposition were investigated. Outgoing from topographic STM images and an extracted mask of boundaries and step edges, several cluster depositions were simulated with different diffusion characteristics. The simulated positions of the clusters were compared to the positions from the experimental images using the χ^2 test. This statistical "goodness of fit" test provides, in this case, an estimation how well the data from the experiment can be described by a certain simulation. It turned out that the plain random simulation can be excluded with a probability of about 90%. According to the test, a mean diffusion path of about 45 nm has the highest probability of about 95%. It also has been shown that other lengths may also occur but with much lower probabilities. So in a first approach it has been demonstrated that the investigated Ag clusters may experience diffusion after landing, although for larger particles less diffusion on the surface is expected. The analysis of the cluster diffusion showed that, although a first statement could be made with the help of the χ^2 test, more experimental data from large area STM images of deposited clusters would help to improve the statistical analysis. An increased number of analyzed particles from the experimental STM images would resulting in a higher statistical relevance of the experimental distance distribution. Another possible enhancement would be the implementation of an improved diffusion simulation. At the moment a diffusion step is realized as a one-pixel movement in any direction. Taking into account the special symmetry and structure of the 7×7 reconstruction, the simulated movement could be adapted to reflect this symmetry. Furthermore the probability for the iterative diffusion steps could be revised in a way to reflect a loss of energy in the cluster during the movement. Here also the characteristic properties of the substrate and the cluster material could be included to investigate a possible dependence on the materials. Another aspect is the temperature dependent preparation, i.e. depositing clusters at different substrate temperatures. In the shown experiments the particles were deposited at room temperature. Taking into account that the particles would be less mobile at lower temperatures, cooling down the substrate would provide access to control the cluster mobility to a certain extend.

In the second part of the experiments, the band topology of nanostructured systems has been investigated using the laser-induced surface photovoltage (SPV). With the help of the STM, a direct measurement of the SPV is possible using simple $I(V)$ spectroscopy. It was shown that Ag nanoparticles, deposited on Si(111)7×7, do not exhibit a spatial-dependent SPV.

Instead, the same SPV was measured on both the cluster and the substrate. Using patches of Si(111)5×2-Au on Si(111)7×7 as a model system, the findings could be attributed to the strong metallic surface states of the 7×7 reconstruction. Measurable differences in the SPV would result in lateral electric fields that are efficiently equilibrated by these surface states. Both systems under investigation can be effectively treated as metal-metal junctions in spite of the semiconducting nature of the underlying bulk Si. On a Si(111) surface that is only partly covered with 5×2 patches, this results in an unusual band bending in the 7×7 regions and a surprisingly large photovoltage of $SPV_{sat} = -0.93$ V. Transferred to the deposited Ag clusters this would mean that the presence of only a few particles may lead to a modification of the surface photovoltage effects. From the SPV measurement we obtain for 5×2 an accurate Fermi-level pinning of $E_F - E_{VBM} = 0.2$ eV, which is supported by recent density functional calculations [79].
The SPV experiments on the nanostructured systems lead to new ideas for future studies. The main issue in the experiments was the metallic character of the 7×7 surface. So a next step would be the transition to surfaces that have a less metallic surface, like e.g. Si(001)2×1. On those substrates the lateral equalizing of the electric fields would be avoided or at least reduced. On such samples the SPV should show a spatial difference on appropriate nanostructures. Other interesting aspects would be a study of the coverage dependent SPV, relating the size and distances of, e.g., small 5×2 patches to the observed modification of the SPV. This would investigate what amount of 5×2 coverage is needed to alter the SPV value. Another improvement to the experiment would be the measurement of the laser intensity in absolute units, providing access to even more physics like carrier mobility and lifetime. Using laser light of different wavelengths during the experiment would also provide access to the minority carrier diffusion length [20].

In the last part of the experiments, GISAXS was used on deposited Ag nanoparticles to study the shape and size effects of the particles during a catalytic reaction. The results showed that the silver clusters are reversibly changing their aspect ratio due to the reaction environment. This changing does even happen at room temperature and can be addressed as the result of the formation of propylene and its influence on the cluster structure and wetting layer. The experiments demonstrate the promising potential of this new approach, where the onset of the catalytic activity of the nanocatalysts is accompanied by dramatic changes in their shape [112], while catalytic activity and selectivity strongly depends on the cluster size [176]. This opens new ways to investigate the correlation between the catalytic function and the catalyst size, composition, and shape.
In further experiments, the change of the Ag particles during the catalytic reaction could be investigated using different methods, but with the same environmental reaction conditions. In our group, e.g., it is planned to use reflection high energy electron diffraction (RHEED) in a reaction environment to directly access the crystal structure of the nanocatalysts during the catalytic reaction. With this method it would be possible to directly investigate the development, growing, and orientation of the faceted clusters. Another approach would be

to use the same reaction environment in high resolution TEM experiments. Up to now this was not possible due to possible contaminations in the TEM cell caused by the propylene. Thus only alternative reactant gases were used in the TEM investigations shown in this work.

A. Appendix

A.1. Analyzing the cluster-boundary distance

In the following the algorithm (see Fig. A.1) used for determining the minimal distance between a cluster position and the next boundary or step edge from a color-coded image is explained. It was implemented in Wavemetrics IGOR Pro 6.

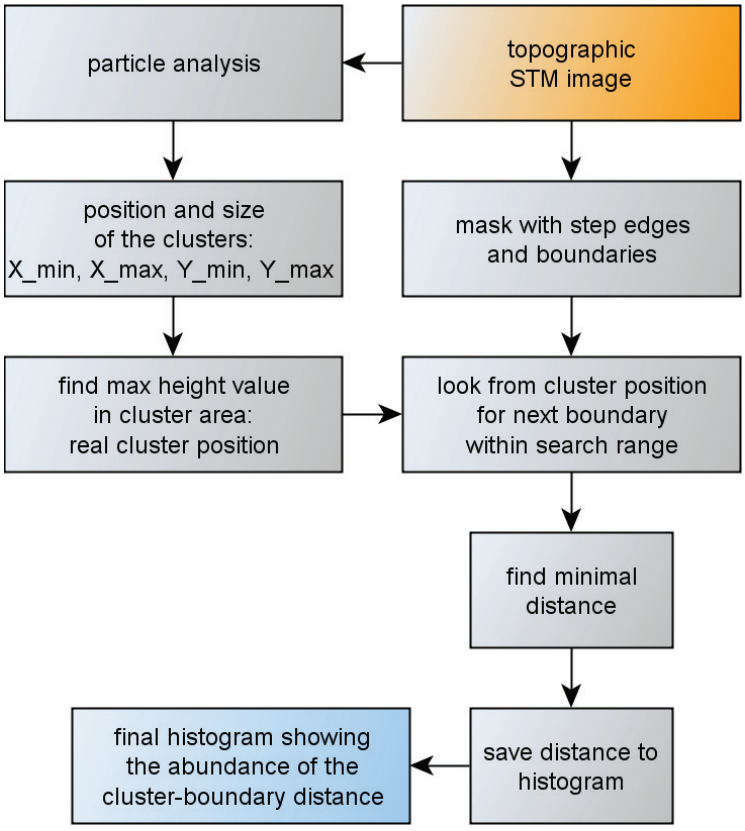

Figure A.1.: Visualization of the algorithm for determining the minimal distance between a cluster and boundary.

From a topographic STM image a color-coded mask (cf. Fig. 4.4) is manually created by marking the step edges and boundaries with different colors, blue and red in this work. For the drawing purposes the software GIMP is used. On the other hand a particle analysis is performed from the original topography with IGOR which yields the positions and the area of each the cluster. The area is thereby approximated by a rectangular shape with is

given by four coordinates: X_{min}, X_{max}, Y_{min} and Y_{max}. Within this area the maximum value for the height (Z_{max}), that corresponds to the brightest pixel, is searched and used for the real position of the cluster. From this position the algorithm searches for the next boundary within a given search range. This search range is a work-around to improve the speed of the search as normally the whole image is searched for the next boundary. The value for search range is manually determined before by looking at the maximum size of the 7×7 patches. During the analysis it can be directly evaluated if a distance is outside the search range, providing a check for the selected range. Nevertheless a good start value would be a bit more than the maximum patch size in the unit of pixel. As the boundaries and step edges are marked with distinct colors, the algorithm searches for a pixel of the color blue or red in this case. The distance from the cluster to the colored pixel is thereby given by a simple geometric construction (Pythagoras). During the search the minimum distance is found by comparing any new distance with the last one and storing the smaller value. The smallest found distance is then saved to a histogram that in the end shows the abundance of cluster-boundary distances.

A.2. Monte-Carlo simulation of cluster deposition

The algorithm for the simulated cluster deposition (see Fig. A.2) is based on the algorithm from appendix A.1, as here also the distances between the simulated clusters and the boundaries are evaluated. On the manually created mask image Fig. 4.4 clusters are randomly positioned by a simple Monte Carlo algorithm. The random numbers are set to be within the X and Y dimensions of the mask image. The topographic STM image which is used as a basis for the simulations, contains 1500 pixel × 1500 pixel and shows a physical size of 1000 nm × 1000 nm. So one single pixel represents a physical size of about 0.67 nm. There are two ways to perform the simulation: (1) the cluster has a fixed random position and (2) the cluster has a finite chance for iterative diffusion steps after the positioning. In the case of diffusion, after setting up the random positions of the particles, they have a probability to perform an iterative diffusion step of one pixel in a random direction, which equals the model of random walk. The probability for a certain step n is given by P^n. In the simulation n equals the number of pixels that directly can be written in a length of nm. Varying the probability can be used to simulate different mean diffusion paths. For a given mean diffusion path λ the probability P can be calculated by

$$0.5 = P^{\lambda} \Rightarrow P = \exp(-\frac{0.69314}{\lambda}) \tag{A.1}$$

The factor 0.5 represents the fact, that the mean diffusion path is defined at the length where the probability decreased to one half. After one diffusion step the probability for a next step remains the same. Another way for an implementation would be that the probability decreases after each step, simulating a loss of energy during the diffusion. But as this

simulation is aimed to a simple approach, this is not performed here. The movement is immediately stopped when the particle hits a boundary or a step edge during the diffusion. This is justified as the pinning of clusters on step edges is known to be energetically favorable. After the diffusion has stopped the cluster has obtained a new position. From this final position the smallest distance to the next boundary is searched like in the same as before in appendix A.1. After the minimal distance is found it is also stored in a histogram. Then the next cluster is randomly deposited until the counting value N reaches the selected number of steps (= numbers of clusters), which is in the case of this work 500000.

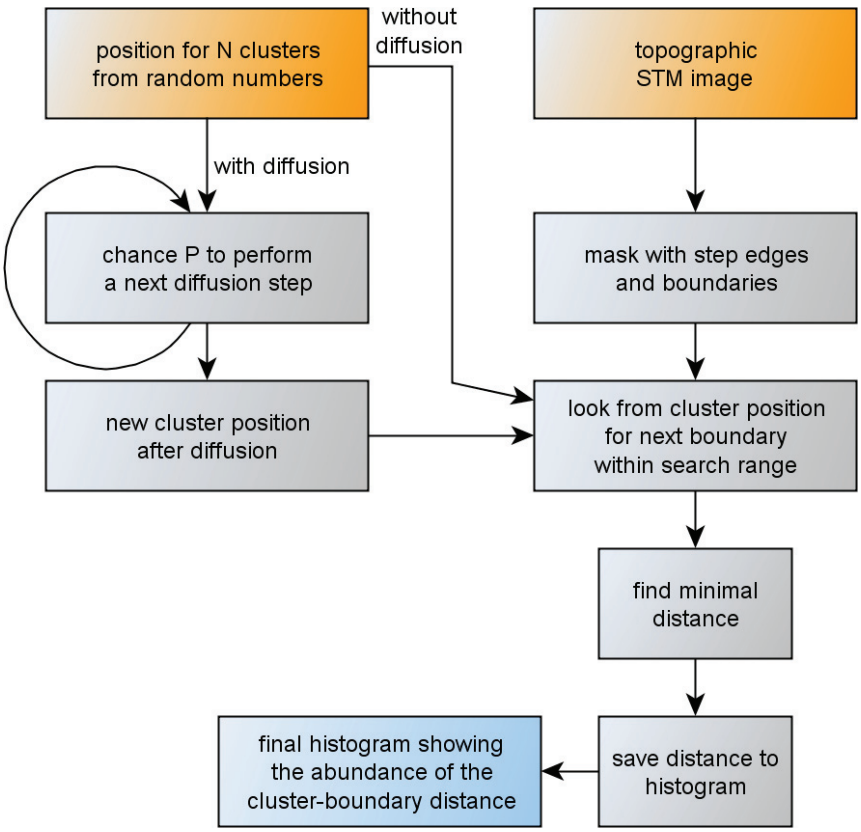

Figure A.2.: Visualization of the algorithm for the simulation of the cluster positioning with and without diffusion and determining the minimal distance between a cluster and boundary.

A.3. Finding the zero-crossing of I(V) curves

In this work the surface photovoltage is directly extracted from $I(V)$ curves that are obtained using the STM. For the analysis it is necessary to find the zero-crossing of a single $I(V)$ curve. Normally, grid spectroscopy is used to obtain the spectra as the analysis of single point spectra is more complicated with the available methods. Another advantage of grid spectroscopy is that an average curve over a specific area can be easily generated. As a result a 2D grid of $I(V)$ spectra is obtained.

In the following the algorithm used for the finding of the zero-crossing of single $I(V)$ curves is described (cf. Fig. A.3). The value for the SPV is represented by the shift of the $I(V)$ curve on the voltage axis, so the new voltage value for $I = 0$ is needed for evaluating the magnitude of the SPV. Due to the fact that there can be a small offset in the tunneling current in the pA range, which is internally generated by the STM electronics, the condition is modified to $I = I_{offset}$, where I_{offset} is the current offset. This offset has been obtained from separate measurements and is well known for the used setup.
The $I(V)$ curve taken from the raw data is then smoothed using the Savitzky-Golay algorithm, which performs a local polynomial regression on a given number of surrounding data points. This provides a lowering of the noise that is normally included in single spectra. When not using the smoothed curve, a small oscillating noise in the range of the zero-crossing could result in multiple voltages where $I = I_{offset}$, making it is impossible to select the correct one.
When measuring the SPV as a function of the laser intensity, the laser power is adjusted after each row of spectra, so all $I(V)$ spectra per row can be averaged before determining the zero-crossing to increase the signal-to-noise ratio. In the end a graph is created where each data point represents the zero-crossing and hence the SPV for the corresponding row in the grid spectroscopy.

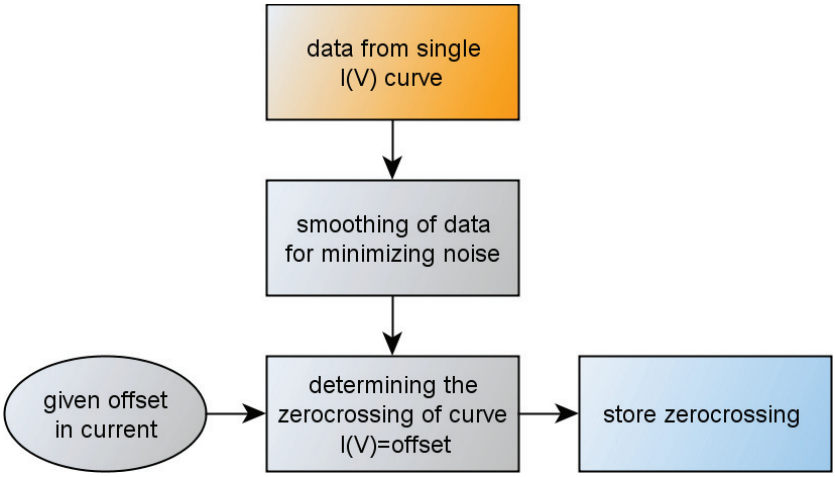

Figure A.3.: Visualization of the algorithm for determining the zero-crossing of single $I(V)$ spectroscopy curves.

Bibliography

[1] W.A. de Heer, Reviews of Modern Physics **65**, 611 (1993)

[2] W.P. Halperin, Reviews of Modern Physics **58**, 533–606 (1986)

[3] *Metal Clusters at Surfaces*, edited by K.-H. Meiwes-Broer (Springer Berlin, 2000) ISBN 3-540-66562-5

[4] U. Heiz and W.D. Schneider, Critical Review in Solid State and Materials Sciences **26**, 251 (2001)

[5] R.M. Lambert, F.J. Williams, R.L. Cropley, and A. Palermo, Journal of Molecular Catalysis A **228**, 27–33 (2005)

[6] K. Bromann, C. Felix, H. Brune, W. Harbich, R. Monot, J. Buttet, and K. Kern, Science **274**, 956 (1996)

[7] S.J. Carroll, S. Pratontep, M. Streun, and R.E. Palmer, Journal of Chemical Physics **113**, 7723 (2000)

[8] I.M. Goldby, L. Kuipers, B. von Issendorff, and R.E. Palmer, Applied Physics Letters **69**, 2819 (1996)

[9] S.J. Carroll, R.E. Palmer, P.A. Mulheran, S. Hobday, and R. Smith, Applied Physics A **67**, 613–619 (1998)

[10] N. Kebaili, S. Benrezzak, P. Cahuzac, A. Masson, and C. Brechignac, European Physical Journal D **52**, 115–118 (2009)

[11] A. Masson, J.J. Metois, and R. Kern, Surface Science **27**, 463 (1971)

[12] P. Jensen, Reviews of Modern Physics **71**, 1695 (1999)

[13] U. Landman, R.N. Barnett, A.G. Scherbakov, and P. Avouris, Physical Review Letters **2**, 2–5 (2000)

[14] D.L. Carroll, M. Wagner, M. Rühle, and D.A. Bonnell, Physical Review B **55**, 9792–9799 (1997)

[15] R. Hasunuma, T. Komeda, and H. Tokumoto, Applied Surface Science **130-132**, 84–89 (1998)

[16] L. Hao and P.A. Bennett, Nanotechnology **20**, 355201 (2009)

[17] O. Kubo, Y. Shingaya, M. Aono, and T. Nakayama, Applied Physics Letters **88**, 233117 (2006)

[18] F. Giannazzo, F. Roccaforte, F. Iucolano, and V. Raineri andM.G. Grimaldi, Journal Of Vacuum Science And Technology B **27**, 789–794 (2009)

[19] J.-L. Sun, X. Zhao, and J.-L. Zhu, Nanotechnology **20**, 0–4 (2009)

[20] L. Kronik and Y. Shapira, Surface Science Reports **37**, 1 (1999)

[21] R.J. Hamers and K. Markert, Physical Review Letters **64**, 1051–1054 (1990)

[22] Y. Kuk, R.S. Becker, P.J. Silverman, and G.P. Kochanski, Physical Review Letters **65**, 456–459 (1990)

[23] D. Gorelik, S. Aloni, and G. Haase, Surface science **432**, 265–278 (1999)

[24] M. Haruta, Catalysis Today **36**, 153–166 (1997)

[25] C. Henry, Surface Science Reports **31**, 231–325 (1998)

[26] H.-J. Freund, Surface Science **500**, 271 (2002)

[27] B. Yoon, H. Häkkinen, U. Landman, A.S. Wörz, J.-M. Antonietti, S. Abbet, K. Judai, and U. Heiz, Science **307**, 403 (2005)

[28] B. Lee, I. Park, J. Yoon, S. Park, J. Kim, K.-W. Kim, T. Chang, and M. Ree, Macromolecules **38**, 4311–4323 (2005)

[29] A.T. Bell, Science **299**, 1688 (2003)

[30] T.A. Nijhuis, M. Makkee, J.A. Moulijn, and B.M. Weckhuysen, Industrial Engineering Chemistry Research **45**, 3447–3459 (2006)

[31] F.W. Zemichael, A. Palermo, M.S. Tikhov, and R.M. Lamber, Catalysis Letters **80**, 93 (2002)

[32] T.A. Nijhuis, T. Visser, and B.M. Weckhuysen, Angewandte Chemie International Edition **44**, 1115–1118 (2005)

[33] S. Vajda, M.J. Pellin, J.P. Greeley, C.L. Marshall, L.A. Curtiss, G.A. Ballentine, J.W. Elam, S. Catillon-Mucherie, P.C. Redfern, F. Mehmood, and P. Zapol, Nature Materials **8**, 213–216 (2009)

[34] W. Schottky, Zeitschrift für Physik **113**, 367–414 (1939)

[35] *Physics of semicondutor devices*, edited by S.M. Sze and Kwok K Ng (Wiley, Hoboken, 2007)

[36] Ioffe Physico-Technical Institute, "Semiconductors on NSM," (2001)

[37] F.J. Himpsel, G. Hollinger, and R.A. Pollak, Physical Review B **28**, 7014 (1983)

[38] J. Viernow, M. Henzler, W.L. O'Brian, F.K. Men, F.M. Leibsle, D.Y. Petrovykh, J.L. Lin, and F.J. Himpsel, Physical Review B **57**, 2321 (1998)

[39] *Physics of Surfaces and Interfaces*, edited by H. Ibach (Springer Verlag, Berlin, 2006) ISBN 978-3-540-34709-5

[40] W.H. Brattain, Physical Review **72**, 345 (1947)

[41] W.H. Brattain and J. Bardeen, Bell System Tech Journal **32**, 1 (1953)

[42] S. Grafstroem, Journal of Applied Physics **91**, 1717 (2002)

[43] K. Horn, M. Alonso, and R. Cimino, Applied Surface Science **56-58**, 271–289 (1992)

[44] Bart van Zeghbroeck, "Principles of semiconductor devices," (2007), http://ecee.colorado.edu/ bart/book/book/index.html

[45] *Semiconductor Devices: Basic Principles*, edited by Jasprit Singh (John Wiley and Sons, Inc., 2001) ISBN 0-471-36245-X

[46] H. Dember, Physikalische Zeitschrift **32**, 856–858 (1931)

[47] M. Barck, Review of Modern Physics **65**, 677 (1993)

[48] *Metal nanoparticles*, edited by J.A. Blackman (Elsevier, 2009) ISBN 978-0-444-51240-6

[49] B. von Issendorff and O. Cheshnovsky, Annual Review of Physical Chemistry **56**, 549–590 (2005)

[50] R. Kubo, Journal of the Physical Society of Japan **17**, 975 (1962)

[51] Y. Long and N.X. Chen, Surface Science **602**, 46–53 (2008)

[52] S. Erkoc and T. Yilmaz, Physica E **5**, 1–6 (1999)

[53] R. Fournier, Journal of Chemical Physics **115**, 2165 (2001)

[54] C. Henry, Progress in Surface Science **80**, 92–116 (2005)

[55] J.J. Lander and J. Morrison, The Journal of Chemical Physics **37**, 729–746 (1962)

[56] J.W.T. Ridgway and D. Haneman, Applied Physics Letters **14**, 265–267 (1969)

[57] G. Binnig, H. Rohrer, F. Salvan, C. Gerber, and A. Baro, Surface Science **157**, L373–L378 (1985)

[58] G. Binnig and H. Rohrer, Review of Modern Physics **59**, 615–625 (1987)

[59] K. Takayanagi, Y. Tanishiro, M. Takahashi, and S. Takahashi, Journal of Vacuum Science and Technology A **3**, 1502–1506 (1985)

[60] Y.-L. Wang, H.-M. Guo, Z.-H. Qin, H.-F. Ma, and H.-J. Gao, Journal of Nanomaterials, 874213(2008)

[61] P. Suttner, P. Zahl, E. Suttner, and J.E. Bernard, Physical Review Letters **90**, 166101 (2003)

[62] K. Miki, Y. Morita, H. Tokumoto, T. Sato, M. Iwatsuki, M. Suzuki, and T. Fukuda, Ultramicroscopy **42-44**, 851–857 (1992)

[63] Y. Zhou, C. Zhou, H. Zhan, Q. Wu, and J. Kang, Materials Science in Semiconductor Processing **9**, 279–282 (2006)

[64] K. Miyake, H. Shigekawa, and R. Yoshizaki, Applied Physics Letters **66**, 3468 (1995)

[65] P. Martensson, W.-X. Ni, G.V. Hansson, J.M. Nicholls, and B. Riehl, Physical Review B **36**, 5974 (1987)

[66] R.I.G. Uhrberg, T. Kaurila, and Y.-C. Chao, Physical Review B **58**, R1730 (1998)

[67] I. Barke, F. Zheng, A.R. Konicek, R.C. Hatch, and F.J. Himpsel, Physical Review Letters **96**, 216801 (2006)

[68] J.E. Demuth, B.N.J. Persson, and A.J. Schell-Sorokin, Physical Review Letters **51**, 2214 (1983)

[69] R.J. Hamers, R.M. Tromp, and J.E. Demuth, Surface Science **181**, 346–355 (1987)

[70] R. Wolkow and Ph. Avouris, Physical Review Letters **60**, 1049 (1988)

[71] J. Ortega, F. Flores, and A.L. Yeyati, Physical Review B **58**, 4584 (1998)

[72] S. Modesti, H. Gutzmann, J. Wiebe, and R. Wiesendanger, Physical Review B **80**, 125326 (2009)

[73] H.E. Bishop and J.C. Riviere, Journal of Physics D **2**, 1635 (1969)

[74] M.-H. Kang and J. Y. Lee, Surface Science **531**, 1–7 (2003)

[75] S.C. Erwin, Physical Review Letters **91**, 206101 (2003)

[76] S. Riikonen and D. Sanchez-Portal, Physical Review B **71**, 235423 (2005)
[77] H.S. Yoon, J.E. Lee, S.J. Park, I.-W. Lyo, and M.-H. Kang, Physical Review B **72**, 155443 (2005)
[78] F.-C. Chuang, C.-H. Hsu, C.-Z. Wang, and K.-M. Ho, Physical Review B **77**, 153409 (2008)
[79] S.C. Erwin, I. Barke, and F.J. Himpsel, Physical Review B **80**, 1–10 (2009)
[80] I. Barke, F. Zheng, S. Bockenhauer, K. Sell, V. von Oeynhausen, K.-H. Meiwes-Broer, S.C. Erwin, and F.J. Himpsel, Physical Review B **79**, 1–9 (2009)
[81] H.S. Yoon, S.J. Park, J.E. Lee, C.N. Whang, and I.-W. Lyo, Physical Review Letters **92**, 096801 (2004)
[82] J.L. Mcchesney, J.N. Crain, V. Perez-Dieste, F. Zheng, M.C. Gallagher, M. Bissen, C. Gundelach, and F.J. Himpsel, Physical Review B **70**, 195430 (2004)
[83] G. Binnig, H. Rohrer, C. Gerber, and E. Weibel, Physical Review Letters **49**, 57–61 (1982)
[84] R. Young, J. Ward, and F. Scire, The Review of Scientific Instruments **43**, 999–1011 (1972)
[85] J.S. Villarrubia, Surface Science **321**, 287 (1994)
[86] J.S. Villarrubia, Journal of Research of the National Institute of Standards and Technology **102**, 435 (1997)
[87] K. Sell, A. Kleibert, V. von Oeynhausen, and K.-H. Meiwes-Broer, European Physical Journal D **437**, 433–437 (2007)
[88] H. Hövel and I. Barke, Progress in Surface Science **81**, 53–111 (2006)
[89] R. Wiesendanger, *Scanning Probe Microscopy and Spectroscopy: Methods and Applications* (Cambridge University Press, 1994)
[90] J. Tersoff and D.R. Hamann, Physical Review Letters **50**, 1998 (1983)
[91] J. Bardeen, Physical Review Letters **6**, 57 (1961)
[92] R.A. Feenstra, Surface Science **299/300**, 965–979 (1994)
[93] D.G. Cahill and R.J. Hamers, Physical Review B **44**, 1387–1390 (1991)
[94] G.P. Kochanski and R.F. Bell, Surface Science Letters **273**, L435–L440 (1992)
[95] T. Hagen, S. Grafström, J. Kowalski, and R. Neumann, Applied Physics A **66**, S973–S976 (1998)
[96] R.H.M. Groeneveld, M.W.J. Prins, and H. van Kempen, Surface Science **331-333**, 1299 (1995)
[97] G. Haase, Int. Reviews in Physical Chemistry **19**, 247–276 (2000)
[98] M. McEllistrem, G. Haase, D. Chen, and R.J. Hamers, Physical Review Letters **70**, 2471 (1993)
[99] R.H. Fowler and L. Nordheim, Proceedings of the Royal Society A **119**, 173–181 (1928)
[100] N.V. Smith, Physical Review B **32**, 3549 (1985)
[101] T. Jung, Y.W. Mo, and F.J. Himpsel, Physical review letters **74**, 1641–1644 (1995)

[102] P. Müller-Buschbaum, Lecture Notes in Physics **776**, 61–89 (2009)

[103] J.R. Levine, J.B. Cohen, Y.W. Chung, and P. Georgopoulos, Journal of Applied Crystallography **22**, 528–532 (1989)

[104] G. Renaud, R. Lezzari, and F. Leroy, Surface Science Reports **64**, 255–380 (2009)

[105] G.H. Vineyard, Physical Review B **26**, 4146 (1982)

[106] M. Rauscher, R. Paniago, H. Metzger, Z. Kovats, J. Domke, J. Peisl, H.-D. Pfannes, J. Schulze, and I. Eisele, Journal of Applied Physics **86**, 6763 (1999)

[107] R. Lazzari, Lecture Notes in Physics **770**, 283–342 (2009)

[108] J.S. Pedersen, Advances in Colloid and Interface Science **70**, 171–210 (1997)

[109] R. Lazzari, Journal of Applied Crystallography **35**, 406–421 (2002)

[110] Y. Yoneda, Physical Review **131**, 2010–2013 (1963)

[111] B. Lee, S. Seifert, S.J. Riley, G. Tikhonow, N.A. Tomczyk, S. Vajda, and R.E. Winans, The Journal of Chemical Physics **123**, 074701 (2005)

[112] S. Vajda, S. Lee, K. Sell, I. Barke, A. Kleibert, V. von Oeynhausen, K.-H. Meiwes-Broer, A. Fraile Rodriguez, J.W. Elam, M.M. Pellin, B. Lee, S. Seifert, and R.E. Winans, The Journal of Chemical Physics **131**, 121104 (2009)

[113] A. Barbier, G. Renaud, and J. Jupille, Surface Science **454-456**, 979–983 (2000)

[114] G. Renaud, R. Lazzari, C. Revenant, A. Barbier, M. Noblet, O. Ulrich, F. Leroy, J. Jupille, Y. Borensztein, C.R. Henry, J.-P. Deville, F. Scheurer, J. Mane-Mane, and O. Fruchart, Science **300**, 1416–1419 (2003)

[115] O.M. Yefanov, A.V. Zozulya, I.A. Vartanyants, J. Stangl, C. Mocuta, T.H. Metzger, G. Bauer, T. Boeck, and M. Schmidbauer, Applied Physics Letters **94**, 123104 (2009)

[116] S.V. Roth, M. Burghammer, C. Riekel, P. Müller-Buschbaum, A. Diethert, P. Panagiotou, and H. Walter, Applied Physics Letters **82**, 1935 (2003)

[117] I.A. Vartanyants, D. Grigoriev, and A.V. Zozulya, Thin Solid Films **515**, 5546–5552 (2007)

[118] I.A. Vartanyants, A.V. Zozulya, K. Mundboth, O.M. Yefanov, M.-I. Richard, E. Wintersberger, J. Stangl, A. Diaz, C. Mocuta, T.H. Metzger, G. Bauer, T. Boeck, and M. Schmidbauer, Physical Review B **77**, 115317 (2008)

[119] M. Kotlarchyk, R.B. Stephens, and J.S. Huang, The Journal of Physical Chemistry **92**, 1533–1538 (1988)

[120] *Soft-Matter Characterization*, edited by R. Borsali and R. Pecora (Springer Verlag Berlin Heidelberg, 2008) ISBN 978-1-4020-8290-0

[121] A. Guinier and G. Fournet, *Small Angle Scattering of X-Rays* (Wiley, New York, 1955)

[122] A.A. Baski, S.C. Erwin, and L.J. Whitman, Surface Science **392**, 69–85 (1998)

[123] J.L. Lin, D.Y. Petrovykh, J. Viernow, F.K. Men, D.J. Seo, and F.J. Himpsel, Journal of Applied Physics **84**, 255 (1998)

[124] R.P. Methling, V. Senz, E.D. Klinkenberg, T. Diederich, J. Tiggesbäumker, G. Holzhüter, J. Bansmann, and K.-H. Meiwes-Broer, The European Physical Journal D **16**, 173 176 (2001)

[125] F. Frank, W. Schulze, B. Tesche, J. Urban, and B. Winter, Surface Science **156**, 90–99 (1985)

[126] J. Passig, K.-H. Meiwes-Broer, and J. Tiggesbäumker, Review of Scientific Instruments **77**, 093304 (2006)

[127] R. Alayan, L. Arnaud, A. Bourgey, M. Broyer, E. Cottancin, J.R. Huntzinger, J. Lerme, J.L. Vialle, M. Pellarin, and G. Guiraud, Review of Scientific Instruments **75**, 2461 (2004)

[128] A. Bettac, *Adsorptionsverhalten, geometrische und lokale elektronische Struktur metallischer Nanopartikel: eine STM Studie*, Phd thesis, Universität Rostock (1999)

[129] Z.Q. Yu, C.M. Wang, Y. Du, S. Thevuthasan, and I. Lyubinetsky, Ultramicroscopy **108**, 873–7 (2008)

[130] C. Schiller, Surface Science **339**, L925–L930 (1995)

[131] L. Nordheim, Proceedings of the Royal Society A **121**, 626–639 (1928)

[132] S. Ernst, S. Wirth, M. Rams, V. Dolocan, and F. Steglich, Science and Technology of Advanced Materials **8**, 347–351 (2007)

[133] J.M.R. Weaver, L.M. Walpita, and H.K. Wickramasinghe, Nature **342**, 783 (1989)

[134] J.A. Stovneng and P. Lipavsky, Physical Review B **42**, 9214 (1990)

[135] S.H. Park, N.M. Miskovsky, P.H. Cutler, and E. Kazes, Surface Science **266**, 265–273 (1992)

[136] B.F.G. Johnson, Coordination Chemistry Review **190-192**, 1269–1285 (1999)

[137] A.W. Ott, J.W. Klaus, J.M. Johnson, and S.M. George, Thin Solid Films **135**, 292 (1997)

[138] S. Vajda, R.E. Winans, J.W. Elam, B. Lee, M.J. Pellin, S. Seifert, G.Y. Tikhonov, and N.A. Tomczyk, Topics in Catalysis **39**, 161–166 (2006)

[139] J. Passig, *Charakterisierung und Optimierung der Nanoteilchenemission aus der Clusterquelle ACIS*, diploma thesis, Universität Rostock (2005)

[140] H.-P. Cheng and U. Landman, Science **260**, 1304–1306 (1993)

[141] M.O. Watanabe, N. Uchida, and T. Kanayama, Physical Review B **61**, 7219–7222 (2000)

[142] J.M. Burgers, Proceedings of the Koninklijke Nederlandse Akademie van Wetenschappen **42**, 293–325 + 378–399 (1939)

[143] G.L. Kellogg, Physical Review Letters **73**, 1833–1836 (1994)

[144] G.L. Kellogg, Progress in Surface Science **53**, 217–223 (1996)

[145] S.J. Carroll, K. Seeger, and R.E. Palmer, Applied Physics Letters **72**, 305 (1997)

[146] E.J. van Loenen, D. Dijkkamp, A.J. Hoeven, J.M. Lenssinck, and J. Dieleman, Applied Physics Letters **56**, 1755 (1990)

[147] J.E. Castle, P.A. Zhdan, and P. Singjai, Journal of Physics D: Applied Physics **31**, 3437 (1998)

[148] *Numerical Recipes - 3rd edition*, edited by W.H. Press, S.A. Teukolsky, W.T. Vetterling, and B.P. Flannery (Cambridge University Press, 2007) ISBN 978-0-511-33555-6

[149] *Statistics (5th ed.)*, edited by W.L. Hays (Holt, Rinehart and Winston, 1994)
[150] NIST/SEMATECH, "e-handbook of statistical methods," (2010)
[151] A. Kleibert, A. Voitkans, and K.-H. Meiwes-Broer, Physical Review B **81**, 073412 (2010)
[152] T.T. Järvi, A. Kuronen, K. Meinander, and K. Nordlung, Physical Review B **75**, 115422 (2007)
[153] T. Castro, R. Reifenberger, E. Choi, and R.P. Andres, Physical Review B **42**, 8548–8556 (1990)
[154] N.-J. Wu, H. Yasunaga, and A. Natori, Surface Science **260**, 75–84 (1992)
[155] E.G. Seebauer and M.Y.L. Jung, in *Landolt-Börnstein - Group III Condensed Matter*, edited by A.P: Bonzel (Springer, Berlin, 2001) ISBN 978-3-540-41223-6
[156] R. Losio, K.N. Altmann, and F.J. Himpsel, Physical Review B **61**, 845–853 (2000)
[157] H.Q. Yang, J.N. Gao, Y.F. Zhao, Z.Q. Xue, and S.J. Panga, Applied Physics A **66**, 1077–1081 (1998)
[158] W. Mönch, in *Chemical and Physics of Solid Surfaces*, Vol. 5, edited by R. Vanselow and R. Howe (Springer, Berlin, 1984)
[159] J. Ortega, A.L. Yeyati, and F. Flores, Applied Surface Science **123**, 131–135 (1998)
[160] J. Schmeidel, H. Pfnür, and C. Tegenkamp, Physical Review B **80**, 1–7 (2009)
[161] R.S. Becker, J.A. Golovchenko, and R.S. Swartzentruber, Physical Review Letters **55**, 987–990 (1985)
[162] G. Binnig, K.H. Frank, H. Fuchs, N. Garcia, B. Reihl, H. Rohrer, F. Salvan, and A.R. Williams, Physical review letters **55**, 991–994 (1985)
[163] H.-C. Ploigt, C. Brun, M. Pivetta, F. Patthey, and W.-D. Schneider, Physical Review B **76**, 1–5 (November 2007)
[164] K. Sell, I. Barke, S. Polei, C. Schumann, V. von Oeynhausen, and K.-H. Meiwes-Broer, Physica Status Solidi B **247**, 1087–1094 (2010)
[165] T.P Chen, S. Fung, and C.D. Beling, Semiconductor Science and Technology **9**, 2101–2106 (1994)
[166] S. Chand and J. Kumar, Semiconductor Science and Technology **10**, 1680–1688 (1995)
[167] T.P Chen, T.C. Lee, C.C. Ling, C.D. Beling, and S. Fung, Solid-State Electronics **36**, 949–954 (1993)
[168] L.K. Galbraith and T.E. Fischer, Surface Science **30**, 185–206 (1972)
[169] B.I. Bednyi and N.V. Baidus, Semiconductors **27**, 620 (1993)
[170] J.R. Maltby, C.E. Reed, and C.G. Scott, Surface Science **93**, 287 (1980)
[171] *Metal-Semiconductor contacts*, edited by E.H. Rhoderick and R.H. Williams (Claredon Press, Oxford, 1988) ISBN 0-19-859336-8
[172] S. Mangal and P. Banerji, Journal of Applied Physics **105**, 083709 (2009)
[173] J. Osvald, Microelectronic Engineering **86**, 117–120 (2009)
[174] R.K. Gupta, K. Ghosh, and P.K. Kahol, Physica E **42**, 1509–1512 (2010)

[175] R.E. Winans, S. Vajda, B. Lee, S.J. Riley, S. Seifert, G.Y. Tikhonov, and N.A. Tomczyk, Journal of Chemical Physics B **108**, 18105–18107 (2004)

[176] L.M. Molina, S. Lee, K. Sell, G. Barcaro, A. Fortunelli, B. Lee, S. Seifert, R. E. Winans, J.W. Elam, M.J. Pellin, I. Barke, V. von Oeynhausen, Y. Lei, R.J. Meyer, J.A. Alonso, A. Fraile-Rodríguez, A. Kleibert, S. Giorgio, C.R. Henry, K.-H. Meiwes-Broer, and Stefan Vajda, Catalysis Today, accepted(2010)

[177] Byeongdu Lee, "private communication," (Oct. 2010)

[178] T. David, D. Buttard, T. Schülli, F. Dallhuin, and P. Gentile, Surface Science **602**, 2675–2680 (2008)

[179] S. Giorgio, S.S. Joao, S. Nitsche, D. Chaudanson, G. Sitja, and C.R. Henry, Ultramicroscopy **106**, 503–507 (2006)

[180] S. Giorgio, M. Cabie, and C.R. Henry, Gold Bulletin **41**, 167–173 (2008)

[181] A.M. Argo, J.F. Odzak, F.S. Lai, and B.C. Gates, Nature **415**, 623 (2002)

[182] P.L. Hansen, J.B. Wagner, S. Helveg, J.R. Rostrup-Nielsen, B.S. Clausen, and H. Topsoe, Science **295**, 2053 (2002)

[183] G. Xiong, J.W. Elam, H. Feng, C.Y. Han, H.-H. Wang, L.E. Iton, L.A. Curtiss, M.J. Pellin, M. Kung, H. Kung, and P.C. Stair, Journal of Physical Chemistry B **109**, 14059 (2005)

[184] J.W. Elam, C.E. Nelson, M.A. Cameron, M.A. Tolbert, and S.M. George, Journal of Physical Chemistry B **102**, 7008 (1998)

[185] P.J. Eng, T.P. Trainor, G.E. Brown Jr., G.A. Waychunas, M. Newville, S.R. Sutton, and M.L. Rivers, Science **288**, 1029 (2000)

[186] J.A. Kelber, C. Niu, K. Shepherd, D.R. Jennison, and A. Bogicevic, Journal of Chemical Physics **446**, 76 (2000)

[187] Z. Lodziana and J.K. Norskov, Journal of Chemical Physics **115**, 11261 (2001)

[188] Z. Lodziana, J.K. Norskov, and P. Stoltze, Journal of Chemical Physics **118**, 11179 (2003)

[189] R. Serna, D. Babonneau, A. Suarez-Garcia, C.N. Afonso, E. Fonda, A. Traverse, A. Naudon, and D.E. Hole, Physical Review B **66**, 205402 (2002)

[190] J.T. Ranney and S.R Bare, Surface Science **382**, 266 (1997)

[191] M. Rocca, L. Vattuone, L. Savio, F.B. d. Mongeot, U. Valbusa, G. Comelli, S. Lizzit, A. Baraldi, G. Paolucci, J.A. Groeneveld, and E.J. Baerends, Physical Review B **63**, 081404 (2001)

[192] V.I. Bukhtiyarov and V.V. Kaichev, Journal of Molecular Catalysis A: Chemical **158**, 167 (2000)

Publications

K. Sell, A. Kleibert, V. von Oeynhausen, and K.-H. Meiwes-Broer, "The structure of Cobalt nanoparticles on Ge(001)", European Physical Journal D **437**, 433-437 (2007)

I. Barke, F. Zheng, S. Bockenhauer, K. Sell, V. von Oeynhausen, K.-H. Meiwes-Broer, S.C. Erwin, and F.J. Himpsel, "Coverage-dependent faceting of Au chains on Si(557)", Physical Review B **79**, 1-9 (2009)

S. Vajda, S. Lee, K. Sell, I. Barke, A. Kleibert, V. von Oeynhausen, K.-H. Meiwes- Broer, A. Fraile Rodriguez, J.W. Elam, M.M. Pellin, B. Lee, S. Seifert, and R.E. Winans, "Combined temperature-programmed reaction and in situ x-ray scattering studies of size-selected silver clusters under realistic reaction conditions in the epoxidation of propene", The Journal of Chemical Physics **131**, 121104 (2009), *(editor's choice 2009)*

K. Sell, I. Barke, S. Polei, C. Schumann, V. von Oeynhausen, and K.-H. Meiwes-Broer, "Surface photovoltage of Ag nanoparticles and Au chains on Si(111)", Physica Status Solidi B **247**, No. 5, 1087-1094 (2010)

L.M. Molina, S. Lee, K. Sell, G. Barcaro, A. Fortunelli, B. Lee, S. Seifert, R. E. Winans, J.W. Elam, M.J. Pellin, I. Barke, V. von Oeynhausen, Y. Lei, R.J. Meyer, J.A. Alonso, A. Fraile-Rodríguez, A. Kleibert, S. Giorgio, C.R. Henry, K.-H. Meiwes-Broer and Stefan Vajda, "Size-dependent selectivity and activity of silver nanoclusters in the partial oxidation of propylene to propylene oxide and acrolein: A joint experimental and theoretical study", Catalysis Today (2010), published online

S. Bartling, I. Barke, K. Sell, S. Polei, V. von Oeynhausen, K.-H. Meiwes-Broer, "Structure of AuSi nanoparticles on Si(111) from reflection high-energy electron diffraction and scanning tunneling microscopy", European Physical Journal D (2010), accepted